Automated Time-Lapse Analysis of Cell Mechanics in Single-Cell Migration on 1D Micropatterns

Johannes Clemens Julius Heyn

Munich 2024

Automated Time-Lapse Analysis of Cell Mechanics in Single-Cell Migration on 1D Micropatterns

Johannes Clemens Julius Heyn

Dissertation
submitted to the Faculty of Physics
Ludwig-Maximilians-Universität
Munich

by
Johannes Clemens Julius Heyn
born in Augsburg, Germany

Munich, the 17th of December 2024

First supervisor: Prof. Dr. Joachim O. Rädler
Second supervisor: Prof. Dr. Martin Falcke
Date of doctoral colloquium: 24th March 2025

Automatisierte Zeitrafferanalyse der Zellmechanik bei der Einzelzellmigration auf 1D-Mikrostrukturen

Johannes Clemens Julius Heyn

München 2024

Contents

List of Figures

List of Tables

Zusammenfassung

Zellmigration ist für verschiedene biologische Prozesse wie Embryogenese, Wundheilung, Immunantwort und Krebsmetastasierung von entscheidender Bedeutung. Die Physik kann dazu beitragen, unser Verständnis der krafterzeugenden Mechanismen hinter der aktiven Zellmigration zu verbessern, um die Entwicklung von Therapien für die Krebsbehandlung und die regenerative Medizin zu unterstützen. *In vitro*-Studien mit planaren Zellsubstraten zeigen sowohl erheblich unterschiedliche Zellmorphodynamiken, aber auch universelle Beziehungen, die über verschiedene Zelllinien hinweg erhalten bleiben. Beispiele sind die biphasische Adhäsions-Geschwindigkeits-Beziehung und die universelle Kopplung zwischen Zellgeschwindigkeit und Zellpersistenz. Mechanische Modelle verknüpfen diese Beziehungen mit physikalischen Kräften und verbinden so intrazelluläre Prozesse mit dem Bewegungsverhalten. Der quantitative Vergleich von experimentellen Daten mit Modellen erfordert jedoch reproduzierbare und standardisierte Bedingungen sowie umfangreiche Statistiken.

Hier präsentiere ich eine automatisierte Zeitrafferanalyse der Einzelzellmigration unter Verwendung einer Hochdurchsatz-Migrationsplattform und eines biophysikalischen Modells. Eine Weiterentwicklung von Mikrostrukturierungsverfahren, mit dem Zweck, Zellmigration auf eindimensionale Bahnen zu beschränken, vereinfachte die Datenerfassung und die Analyse der Zelltrajektorien. Die standardisierte Mikrofabrikation von 1D-Fibronektin-beschichteten Bahnen und die Scanning-Zeitraffer-Mikroskopie ermöglichten reproduzierbare Versuchsbedingungen für die Hochdurchsatz-Datenerfassung und die automatisierte Bildanalyse. Die Technik ermöglichte die Analyse von Tausenden von Einzelzell-Trajektorien, wobei eine erhebliche Variabilität innerhalb derselben Zelllinie festgestellt werden konnte, was für die Identifizierung universeller Verhaltensweisen von Bedeutung ist. In diesem Zusammenhang haben wir bei der Brustkrebszelllinie MDA-MB-231 Multistabilität in Form von vier Bewegungszuständen entdeckt. In Zusammenarbeit mit der Gruppe von Martin Falcke haben wir ein neuartiges biophysikalisches Modell vorgeschlagen, das aus Kraftbilanzen an den Zellenden, einem verrauschten Kupplungsmechanismus und einer nichtlinearen Integrin-Signalübertragung besteht. Das Modell erklärt Multistabilität, die Adhäsions-Geschwindigkeits-Beziehung und die universelle Kopplung zwischen Zellgeschwindigkeit und Zellpersistenz. Die nichtlineare, stochastische Natur des biophysikalischen Modells stellte jedoch für die Parameteroptimierung eine Herausforderung dar. Durch Training eines neuronalen Dichte-Schätzers wurden die Modellparameter aus den experimentellen Trajektorien abgeleitet. Der Ansatz

ordnet Parameterwerte effektiv verschiedenen Zelltypen zu und identifiziert den Wirkort von Wirkstoffen wie Latrunculin A und Y-27632 ohne Vorkenntnisse.

Wir haben eine Zeitraffer- und Datenanalyseplattform für Studien zur Zellmigration mit einem noch nie dagewesenen Durchsatz entwickelt. Unser zellmechanisches Modell erklärt ein beispielloses Maß an komplexem Bewegungsverhalten, das durch umfangreiche Statistiken validiert wird. Wir gehen davon aus, dass unsere Arbeit weitere Entdeckungen im Zusammenhang mit den spezifischen Eigenschaften von Zelltypen, universellen Beziehungen und biophysikalischen Mechanismen ermöglichen wird.

Summary

Cell migration is crucial in several biological processes, such as development, wound healing, immune response, and cancer metastasis. Physics can help shed light on the force generating mechanisms behind active cell migration, improving our understanding to aid the development of therapies related to cancer treatment and regenerative medicine. *In vitro* studies reveal diverse cell morphodynamics on plane adhesive substrates, as well as universal relations conserved across different cell lines, such as the biphasic adhesion-velocity relation and the universal coupling between cell speed and cell persistence. Mechanical models link these relations to physical forces, thereby connecting intracellular processes with motile behaviour. However, quantitative comparison of experimental data to models requires reproducible conditions as well as extensive statistics.

Here, I present an automated time-lapse analysis of single-cell migration using a high-throughput migration platform and a biophysical model. We advanced micropatterning for confined cell migration on one-dimensional fibronectin lanes which simplified data acquisition and trajectory analysis. Standardised microfabrication of 1D fibronectin coated lanes and scanning time-lapse microscopy enabled reproducible experimental conditions for high-throughput data collection and automated image analysis. The technique allowed for analysis of thousands of single-cell trajectories, finding significant variability within the same cell line, which is important for identifying universal behaviours. In this context, we discovered multistability in the form of four motile states in the breast cancer cell line MDA-MB-231. In collaboration with the group of Martin Falcke we proposed a novel biophysical model that consists of force balances at the protrusion edges, a noisy clutch mechanism and non-linear integrin signalling. The model explains multistability, the adhesion-velocity relation and the universal coupling between cell speed and cell persistence. However, the non-linear, inherently stochastic nature of the biophysical model presented significant challenges, as parameter optimisation became mathematically and conceptually difficult. By training a neural density estimator model parameters were inferred from experimental trajectories. The approach effectively asigns parameter values to different cell types and identifies the site of drug action, like latrunculin A and Y-27632 without prior knowledge.

We developed a time-lapse and data analysis platform for studies of cell migration with unprecedented throughput. Our cell-mechanical model explains an unparalleled level of complex motile behaviour, validated by extensive statistics. We anticipate that our work will facilitate additional discoveries related to the specific characteristics of cell types, universal relations, and biophysical mechanisms.

List of Publications

Parts of this dissertation have been published in or are about to be submitted to peer-reviewed journals. Here, (J) denotes journal articles that have been peer-reviewed and published and (M) manuscripts that are in the process of being peer-reviewed, ready for submission, or in preparation.

J1 "On the adhesion–velocity relation and length adaptation of motile cells on stepped fibronectin lanes"
Christoph Schreiber*, Behnam Amiri*, **Johannes C. J. Heyn**, Martin Falcke, Joachim O. Rädler
* - authors contributed equally
Proceedings of the National Academy of Sciences 118.4 (2021) [1]

J2 "On multistability and constitutive relations of cell motion on fibronectin lanes"
Behnam Amiri, **Johannes C. J. Heyn**, Christoph Schreiber, Joachim O. Rädler, Martin Falcke
Biophysical Journal (2023) [2]

J3 "Mesenchymal cell migration on one-dimensional micropatterns"
Johannes C. J. Heyn, Martin Falcke, Joachim O. Rädler
Frontiers in Cell and Developmental Biology 12 (2024) [3]

M1 "Cell-mechanical parameter estimation from 1D cell trajectories using simulation-based inference"
Johannes C. J. Heyn*, Miguel Atienza Juanatey*, Martin Falcke, Joachim O. Rädler
* - authors contributed equally
submitted to *PLOS ONE* (2024), published as preprint [4]

M2 "Intrinsic cell-to-cell variance from experimental single-cell motility data"
Anton Klimek, **Johannes C. J. Heyn**, Debasmita Mondal, Sophia Schwartz, Joachim O. Rädler, Prerna Sharma, Stephan Block, Roland R. Netz
submitted to *PRX Life* (2024), published as preprint [5]

M3 "Myosin VI and its effect on the migration of RPE cells"
Markus Kröss*, **Johannes C. J. Heyn***, Joachim O. Rädler, Claudia Veigel
* - authors contributed equally

Over the course of my graduation I had the opportunity to contribute to several conferences and summer schools in the form of talks (T) and posters (P).

T1 international Physics of Living Systems (iPOLS), conference | 06/2022 | Montpellier, France
Johannes C. J. Heyn, Behnam Amiri, Christoph Schreiber, Martin Falcke, Joachim O. Rädler

T2 DPG Frühjahrstagung 2022, conference | 09/2022 | Regensburg, Germany
Johannes C. J. Heyn, Behnam Amiri, Christoph Schreiber, Martin Falcke, Joachim O. Rädler

P1 DPG Frühjahrstagung 2021, conference | 09/2021 | virtual
Christoph Schreiber, Behnam Amiri, **Johannes C. J. Heyn**, Martin Falcke, Joachim O. Rädler

P2 Physics of Cells (PhysCell) 2022, conference | 09/2022 | Rehovot & Ein Gedi, Israel
Johannes C. J. Heyn, Behnam Amiri, Christoph Schreiber, Martin Falcke, Joachim O. Rädler

P3 DPG Frühjahrstagung 2023, conference | 03/2023 | Dresden, Germany
Johannes C. J. Heyn, Behnam Amiri, Christoph Schreiber, Martin Falcke, Joachim O. Rädler

P4 CeNS/SFB1032, workshop | 09/2023 | Venice, Italy
Johannes C. J. Heyn, Miguel Atienza Juanatey, Behnam Amiri, Martin Falcke, Joachim O. Rädler

Introduction

In 1623, Galileo introduced a now-famous metaphor frequently referenced by scientists: “Nature”, he claimed, “is a book written in the *language of mathematics*” [6]. To this day, most researchers and especially physicists hold a firm belief that only a quantitative description of nature will lead to a thorough understanding of its structure and dynamics. This assumption concerns both experimental observations as well as theoretical models and affects both inanimate and animate matter. Hence, it does not come as a surprise that the quest for quantitative measurements and mathematical models of biological systems has established the interdisciplinary science of biophysics [7–11]. However, the characterisation of animate or living matter has consistently been challenging due to the intrinsic noise occurring at virtually all levels, ranging from fundamental molecular and sub-cellular processes to the dynamics of tissues, organs and populations [12]. The motile dynamics of mammalian cells is no exception to this observation.

Cell migration is an essential characteristic inherent to all mammalian cells. The term cell motility describes the mechanism by which cells relocate from one location to another. This capability is vital for various biological processes, such as cellular movement during development, tumour metastasis, wound repair, and immune system functions [13–15]. Impairments in cell motility processes can lead to significant adverse effects. The ability to invade tissues and metastasise, for example, is a hallmark of cancer [16–18]. The dissemination of cancerous cells underscores the critical need to understand the mechanisms governing cell motility.

Biological studies have identified the main protagonists of cell migration and a basic theory of biological processes is by now well established: cell motility is facilitated by a sophisticated mechanism that relies on treadmilling of the actin cytoskeleton. Actin polymerisation at the cell’s front advances the leading edge while contractile forces retract the rear. Cells establish adhesions to connect the cytoskeleton to the substrate, enabling force transmission. These activities are orchestrated by a complex regulatory network that involves hundreds of proteins [19–22].

Mathematical models bridge experiments and theories, offering mechanistic insights into various aspects of cell migration. Due to the intricate nature of cell migration, these models are typically modular, focussing on interactions between components such as actin dynamics, protrusion, adhesion, contraction, and morphodynamics [23–25].

However, comparing these complex models with experimental data presents chal-

lenges due to the heterogeneity of the data. For an effective comparison, it is crucial to employ reproducible, standardised conditions and robust statistics. *In vivo* measurements typically cannot satisfy these requirements which is why *in vitro* cell migration assays are far more common. Recent advances in microfabrication allow precise control over cell environments and adjustment of external parameters like ligand density, substrate stiffness, and pore size [26–31]. Planar substrates mimic the *in vivo* environment of a cell crawling on top of a basement membrane between epithelial tissues. The two-dimensional (2D) migration along the adhesive substrate simplifies data acquisition because the cells can be imaged and followed in a single focal plane. The use of one-dimensional (1D) lanes for further confinement has been particularly beneficial as it reduces the complexity of analysing cell movement to a one-dimensional problem [32, 33]. The use of scanning time-lapse microscopy facilitates the parallel tracking of hundreds of cells over multiple days, enabling a thorough examination of the motile behaviour of the cells [34]. However, because of the heterogeneity of the data, even more data is necessary to study biological phenomena like morphodynamics and said cell-to-cell variability, as well as to validate complex cell-mechanical models. Automating 1D single-cell migration assays effectively allows high-throughput analysis and produces large datasets, facilitating mathematical model validation and data-driven insights [31, 35]. Increasingly detailed studies make it possible to observe and explain cell migration at a new level of complex behaviour that will lead to better cellular and molecular characterisation and classification [36].

The outline of this thesis is structured to guide the reader through the development of a systematic framework that enables a high-throughput single-cell analysis of cell motility.
Chapter 2 lays the foundation of this thesis by introducing key concepts of cell migration and the vast experimental and theoretical toolbox to study it. Mesenchymal cell migration is defined and methods of microfabrication, basic observations of cell motility and mathematical modelling approaches are described.
Chapter 3 presents the experimental setup that allowed high-throughput data acquisition and analysis. Building on the established technique of scanning time-lapse microscopy of cells in 1D confinement, novel improvements of the setup are discussed that significantly increase the efficiency of the data workflow to unprecedented throughputs.
Chapter 4 quantifies the cell-to-cell variance of migrating cells. To this end, the experimental 1D cell migration assay and the generalised Langevin equation are used, revealing significant differences between cells even within the same cell line.
Chapter 5 presents a biophysical model linking observed phenomena to cytoskeletal dynamics and cell-environment interactions. The mathematical framework considers force balance at the cell's leading edge, the noisy clutch of retrograde flow, and friction and drag influenced by integrin signalling. The one-dimensional fibronectin lanes offer the crucial experimental setup to quantitatively analyse cell motility and validate the biophysical model.
Chapter 6 introduces simulation-based inference which was employed to pinpoint cell-specific parameters affecting migration in both healthy and cancerous human epithelial

cell lines. Using 1D trajectory data from automated imaging on micropatterned fibronectin lanes, a neural density estimator was used to deduce parameters related to cell dynamics. The findings indicated notable variations in actin polymerisation and protrusion length between the cell lines. SBI successfully identified the impact of two cytoskeletal inhibitors without prior knowledge.
Chapter 7 concludes the main results of this thesis and discusses implications and further experiments.
Chapter A contains all the methods necessary to reproduce the contents of this thesis. It provides experimental protocols and descriptions of the algorithms used in the main text.
Chapter B offers supplementary information that is not strictly needed to follow the main text but may, nevertheless, lead to a better understanding. It contains additional figures and more detailed information that were omitted in the main text for a more concise and natural reading flow.

Fundamental Concepts

The outline and content of this chapter is based in large parts on our review on “Mesenchymal cell migration on one-dimensional micropatterns” [3] to which I contributed in writing and visualisation. I will start by defining the object at the centre of this doctoral thesis, i.e. the migration of single mesenchymal cells. I will then try to convince the reader that one-dimensional (1D) confinement poses a worthwhile approach to limit variable space and allow a quantitative study of cell migration. Then, I will introduce the two microfabrication techniques for 1D migration platforms that I used for my studies. Afterwards, I will present the most common biophysical modelling approaches with a focus on mechanical models such as our protrusion competition model [1]. This section will be followed up by an introduction to simulation-based inference (SBI) which is a mathematical method that allows likelihood-free inference of model parameters based on neural density estimation, an approach that I tested in the context of 1D cell motility.

1 Mesenchymal Cell Migration

Mesenchymal cell migration is a type of actively driven cell movement that is relevant for several important biological processes such as embryonic development, tissue repair, immune response and cancer metastasis [13, 37–41]. During embryonic development mammalian cells not only proliferate and differentiate but also migrate to form various tissues and organs [37, 42–44]. To repair connective tissue, fibroblasts, which are “the principal active cell[s] of connective tissue” [45], migrate into wounds and regenerate the tissue by secreting proteins of the extracellular matrix (ECM) [37, 38]. Certain immune cells use mesenchymal-like migration, guided by spatial cues, to reach the region of interest [38]. Cancer metastasis – when some cancer cells undergo a transition from being of epithelial type to being of mesenchymal type (EMT) and start migrating away from tumors to invade other tissues or organs – has long been a well-established hallmark of cancer [16–18]. Consequently, understanding the mechanisms of mesenchymal migration is crucial for the development of therapies related to wound healing, cancer treatment, and regenerative medicine. Additionally, it also poses interesting physical questions as I will show shortly. However, before diving into the topic, I will define what I mean by “mesenchymal cell migration”.

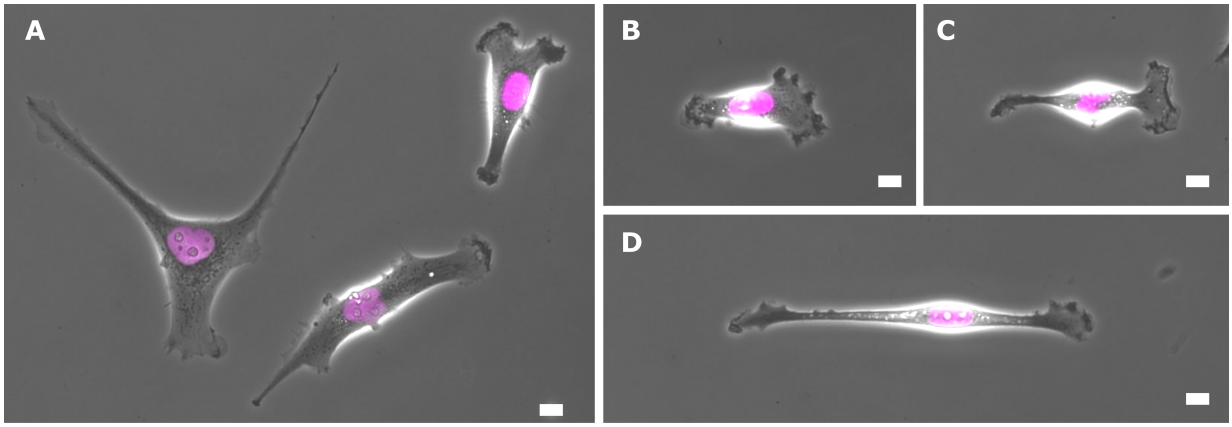

Figure 2.1: Phase contrast micrographs of mesenchymal cells migrating on a Fibronectin coated surface in 2D. Cells are of the epithelial breast cancer type MDA-MB-231 with the fluorescent nuclear marker H2B-mCherry displayed in pink. **(A)** Without external cues cells polarise along any direction in 2D. Even cells in close proximity form protrusions without apparent directional alignment, with some cells even forming multiple protrusions at the same time. **(B-D)** Once a cell has achieved uni-axial polarisation it can elongate its body to a remarkable extend. The cell in (D) is 160 µm long while it is only several micrometres wide. The stiffness of the nucleus causes an enlarged width at its position close to the geometrical centre of the cell resulting in a spindle-shape characteristic for mesenchymal migration. Despite the cell adhering to a flat 2D surface, its motile behaviour is reminiscent of 1D dynamics. Scale bars for all panels equal 10 µm.

The term *mesenchymal* in this context refers to the fact that cells phenotypically appear similar to cells of the *mesenchyme*, a type of embryonic connective tissue that gives rise to the development of most of the body's connective tissues and organs [46–48]. Another category of migration mode would be *amoeboid* in which cells migrate by changing their shape accompanied by visible streaming of cytoplasm thereby resembling the behaviour of *amoebae*, i.e. shape altering unicellular organisms [49]. The mesenchymal migration mode is characterised by elongated, spindle-shaped cells that use protrusions called lamellipodia to move, see Fig 2.1. Cells adhere strongly to the extracellular matrix through focal adhesions and may secrete matrix-degrading enzymes to remodel their environment as they migrate [50]. For cells on plane adhesive substrates, mesenchymal migration can be described as a cyclic process consisting of the following steps: polarisation breaks the spatial symmetry to establish an anterior-posterior (front-rear) axis, and membrane protrusions form. Next, the protrusions are stabilised by transmembrane receptors which anchor the cell to the substrate and allow a transduction of internal forces. Lastly, the cell contracts and releases adhesions at its rear resulting in a displacement.

Front-back polarity is regulated primarily by the Rho GTPase Cdc42 although other members of the Rho GTPase family such as Rac and Rho, as well as phosphoinositide 3-kinases (PI3Ks) and integrins are also involved [20, 51–55]. Rho GTPases are molecular switches that are located at the membrane-cytosol interface. They cycle between a GTP-bound on-state and a GDP-bound off-state, driven by GTPase-activating proteins (GAP) and guanine nucleotide exchange factors (GEF), respectively [56]. Gradients of these regulators lead to localised activation or inhibition of chemical reactions thereby breaking

the initial spatial symmetry and establishing cell polarisation. The formation of protrusions typically happens immediately after the polarisation of the cell. At the edge of the cell, just under the plasma membrane, globular actin (g-actin), which is the monomeric form of actin, polymerises at the barbed ends of filamentous actin (f-actin). Actin filaments together with microtubules and intermediate filaments make up the cytoskeleton which gives the cell its shape. The g-actin at the leading edge binds only to the growing filament when thermal fluctuations (Brownian motion) cause a sufficiently large gap between the filament and the plasma membrane. The monomer will then (with a certain probability) polymerise onto the tip of the filament, effectively closing the gap. The polymerising filament, hence, rectifies Brownian motion which gives rise to a unidirectional force, a mechanism termed "Brownian ratchet" [57, 58]. If we assume for a moment the leading edge to be a stiff wall, firmly anchored in the frame of reference, the polymerising filament's force would lead to a reaction force that pushes the filament away from the edge and towards the centre of the cell. This flow of filaments is called *actin retrograde flow* and the mechanism is termed *treadmilling*. This picture, however, leaves out the fact that the retrograde flow experiences friction within the cytoplasm resulting in an anterograde force. This force pushes the membrane forward thereby forming a protrusion. These protrusions are called *lamellipodia*. They are thin sheets of cytoplasm that are 0.1 µm to 0.3 µm in thickness and cover tens to hundreds of square micrometres [20, 59–63]. Behind its protruding contour the lamellipodium is composed of a network of actin filaments with the protein complex Arp2/3 mediating the branching of the filaments [64–72]. The actin filaments serve both as the support structure that gives the cell its (dynamic) shape and as pathways for cargo transport. Both functions are supported by motor proteins that can move along the actin filaments using energy derived from Adenosine triphosphate (ATP) hydrolysis. These proteins form the myosin superfamily [73]. All myosin motors, with the notable exception of myosin VI, translocate towards the barbed end of actin filaments [74]. Of the 12 distinct classes of human myosins, non-muscle myosin II is considered to be the most essential motor protein for cell migration as it contributes to the contraction of the posterior of the cell [20, 75, 76]. An increased expression of myosin light chain kinase (MLCK) which activates myosin II has been linked to metastatic cancer cells [77]. Myosin II activity can be selectively and specifically targeted by the small molecule inhibitor blebbistatin [78, 79].

Transmembrane receptors of the integrin family, located a few micrometres inwards from the leading edge, are dynamically coupled to the cytoskeleton and form so called *focal adhesions*. Integrins connect the cell to the substrate so that internal forces can be transduced [19, 80–90]. The integrins' coupling to the substrate results in an effective drag of the actin network [91]. Without the coupling the actin network would not be able to apply an anterograde force pushing the leading edge forward. Integrins engage with extracellular matrix (ECM) macromolecules by binding to specific amino-acid sequences such as the Arg-Gly-Asp (RGD) motif [92, 93]. The tripeptide sequence RGD can be found on a variety of ECM molecules, most notably in the glycoprotein fibronectin (FN) [94–97]. Fibronectin is one of the major components of the basement membrane on which cells crawl e.g. during wound healing, next to collagen, laminin and fibrin. Integrins first

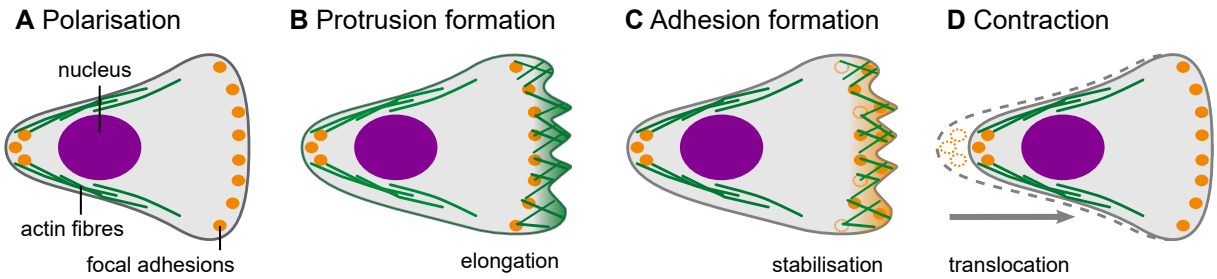

Figure 2.2: The four key steps in cell migration: polarisation breaks the spatial symmetry; protrusion formation leads to an elongation of the cell; adhesion formation stabilises the cytoskeleton and allows a transduction of forces; contraction results in a translocation of the cell. **(A)** A visible hallmark of cell polarisation is the spatial asymmetry of the cell caused by few focal adhesions at the rear side and a broad front of focal adhesions at the cell's front. This is accompanied by a rearward displacement of the nucleus with respect to the cell's geometrical centre. **(B)** At the leading edge of the cell, actin fibres polymerise into a network that pushes the membrane forward thereby forming a protrusion called *lamellipodium*. **(C)** Integrins form focal adhesions that stabilise the protrusion and transduce forces to the substrate. **(D)** Lastly, the cell releases its adhesions at the rear and contracts resulting in a translocation. Based on the review by Ridley et al. 2003 [20].

form short-lived adhesive structures called nascent adhesions upon engagement with FN. These nascent adhesions promote Rac activity and activate other signalling pathways that lead to myosin II recruitment. This in turn results in contractile forces that promote further recruitment of proteins, including also even more myosin II, thereby developing the adhesion site from a being a nascent adhesion to a stabilised focal adhesion [98–100].

Further back from the leading edge, i.e. closer to the centre of the cell, the pointed ends of the actin filaments undergo depolymerisation, thereby replenishing the pool of actin monomers [13, 67]. For a comprehensive review on actin as one of the major polymers of the cytoskeleton see for example Pollard 2016 [101]. Actin binding compounds that regulate the actin dynamics are commonly used as tools to investigate actin network mechanics and cell migration. Researchers divide small actin binding molecules into two groups: destabilisers and stabilisers [102]. Important compounds are the destabilisers cytochalasin D and latrunculin A, as well as the stabiliser phalloidin [103–107]. Latrunculin A, which was first found in the marine sponge latrunculia magnifica, specifically inhibits actin polymerisation [103, 105]. Another commonly used tool is the specific ROCK-inhibitor Y-27632 [108, 109]. Y-27632 can shed light onto the regulatory Rho/ROCK pathway which is an essential control element in mesenchymal cell migration. Rho-associated protein kinase (ROCK) increases myosin II activity and promotes cell adhesion [56]. Y-27632 diminishes these effects.

In contrast to the mesenchymal mode, cells that migrate in an amoeboid mode have a more rounded morphology and can move in an adhesion-independent manner [50]. Amoeboid migration is often faster than mesenchymal migration (cell speed ~10 µm/min for amoeboid vs ~1 µm/min for mesenchymal) and is used by cells like neutrophils (highly mobile white blood cells that are part of the immune system) as well as some cancer

cells [38, 88, 110]. Recent studies have also proposed the existence of another migration mode, named “lobopodial” in which cells form bleb-like protrusions called lobopodia to migrate using hydrostatic pressure [111]. For completeness one should also mention that cells can not only migrate all by themselves but also collectively. The conceptional relationship between single and collective cell migration is still a topic of active research but falls outside the purview of this thesis [112].

The multistep process of mesenchymal cell migration has been observed across a plethora of vastly different cell lines [32]. This observation leads to the question if mesenchymal cell migration can be understood by a single biophysical model and, consequently, if it is possible to quantitatively characterise and compare the migration of different cell types.

2 Cell Migration in Confinement

General observations of mesenchymal cell migration include that the migration behaviour strongly depends on various parameters of the extracellular environment such as pore size of the ECM (in 3D), stiffness of the substrate (2D), chemical cues, and ligand density [28, 113–117]. Cells are also capable of remodelling their environment by cleaving ECM proteins or secreting and depositing proteins of their own such as FN into the ECM [118]. Mesenchymal cells that are embedded in a matrix with a pore size significantly smaller than their nuclear diameter rely strongly on matrix degradation [111, 119, 120]. Another observation is that cells not only move their position (locomotion) but also change their shape (morphodynamics). Cells constantly develop new – sometimes multiple – protrusions, change direction and speed [121–139].

To reduce the parameter space considerably and enable quantitative studies of cell migration, cells are often studied in artificial confinement *in vitro* [140]. The simplest confinement, from an experimental point of view, consists in placing cells on a protein coated substrate. This way, cells crawl in a plane which makes image acquisition less challenging compared to a 3D environment, and the assay already provides some control over external parameters such as substrate stiffness and ligand density while also being reproducible [60, 141]. To further reduce the phenomenon of cell migration to its underlying mechanism, cells are confined to 1D micropatterns. This results in cells having two protrusions at most, one at each end of the cell. The morphology and morphodynamic of a cell can then be described by the position of the front ($x_\mathrm{f}(t)$), the position of the nucleus ($x_\mathrm{n}(t)$), and the position of the back ($x_\mathrm{b}(t)$) of the cell along a single axis, see Fig. 2.3 (A). This confinement allows the acquisition of large quantities of trajectories and the identification of dynamic patterns in the data. The high-throughput of data makes it not only possible to characterise and compare different cell lines but also provides the foundation of the formulation of biophysical models [32, 140, 142, 143].

1D confinement is commonly achieved by adhesive patterns in the shape of lanes, functionalised with ECM proteins such as fibronectin or collagen. The spaces between

these adhesive patterns are effectively blocked using cell-repellent block-copolymers like poly(L-lysine) grafted poly(ethylene glycol) (PLL PEG) [33, 144–148]. A critical parameter in this process is the width of the 1D microlanes, which is typically designed to match the size of the cell nucleus [144, 146]. The primary method for data acquisition in cell migration studies is live-cell time-lapse imaging. This technique enables detailed observation of cell movement, morphology, and intracellular dynamics. Wide-field images superimposed with fluorescence can visualise the geometry of the confinement and track the position of the cell nucleus, see Fig. 2.3 (B). Wide-field images provide comprehensive information about the overall shape of the cell, while fluorescent cytoskeleton markers reveal critical intracellular structures and activities, such as the actin cortex or focal adhesions.

Micropatterns offer standardised and reproducible boundary conditions for cell motion, facilitating the acquisition of large datasets of cell trajectories and enabling automated image analysis. In scanning time-lapse mode, numerous adjacent fields of view are imaged sequentially, allowing the acquisition of hundreds of migrating cells within a single time-lapse interval. This method reduces the complexity of analysing cell migration to tracking distinctive points over time, such as the position of the cell nucleus. For a minimalistic description of cell shape dynamics, tracking the positions of the front and back of the cell is sufficient to determine cell length L over time. Long-term imaging using incubation stages enables the tracking of migratory dynamics over extended periods such as 48 h, see the kymograph in Fig. 2.3 (C). Kymographs, which are slices through a time stack along the time-axis, visualise cell movement in a single image. Here, the vertical axis represents the position along the micropattern while the horizontal axis represents the progression of time from left to right. The standardised conditions and large statistical datasets facilitate the comparison of migratory behaviours across different cell lines, as first implemented on a large scale by Maiuri et al. in the “First World Cell Race” comprising of 54 different cell types [32]. Notably, variations in mean cell speed, mean persistence time, the fraction of time cells spend in a motile state, and the rate of transitions between these states can be observed and compared across different cell lines.

In short, the use of 1D adhesive patterns functionalised with ECM proteins, combined with advanced imaging techniques and standardised micropatterns, provides a robust framework for studying and comparing the migratory behaviours of different cell lines. This approach not only enhances our understanding of cell motility but also enables the identification of fundamental principles governing cell movement as I will show shortly. First, however, I will introduce the two main methods of microfabrication for 1D confinement.

3 Methods of Microfabrication for 1D Confinement

Micropatterns that confine cell migration require the fabrication of substrates with defined areas functionalised by cell ahesive proteins (ligands). These adhesive areas are surrounded by a passivation or non-fouling layer that inhibits cell attachement. Micropatterning techniques permit controlled experimental conditions, including ligand density, substrate stiffness, and pattern geometry. Various geometries have been reported in the

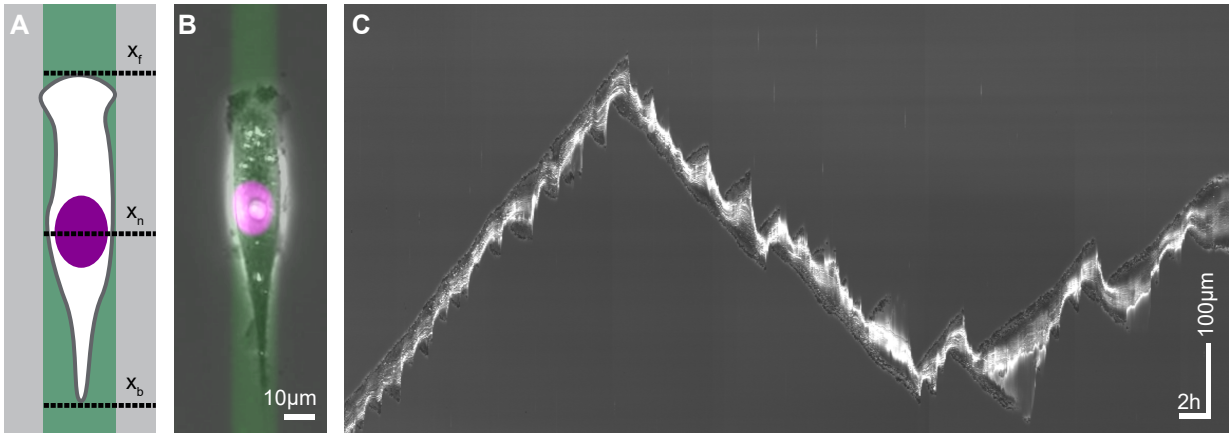

Figure 2.3: Single cell migration in one-dimensional (1D) confinement. 1D micropatterns facilitate the study of mesenchymal cell migration by enabling the acquisition of large statistical datasets. **(A)** Schematic of a cell on a lane functionalised with an extracellular matrix (ECM) protein. The cell's migration is tracked by the positions of its front (x_f), nucleus (x_n), and back (x_b) over time. **(B)** Micrograph of a human breast cancer cell (MDA-MB-231) on a fibronectin (FN) lane. The cell contour is visible in phase contrast, with the nucleus stained violet and the ECM protein green visualised using epi-fluorescence. Scale bar: 10 µm. **(C)** Kymograph of a migrating cell, illustrating changes in velocity, direction, and cell length. Time progresses from left to right. The vertical axis represents the position along the centre of the micropatterned lane. Horizontal scale bar: 1 h, vertical scale bar: 100 µm. Adapted from Heyn et al. 2024 [3].

context of confined migration, including lanes of varying width and length, rings, and zig-zag patterns. Microlanes have emerged as the standard geometry for 1D migratory assays [32, 144, 149–154]. In recent years, two fabrication techniques have proven particularly useful: microcontact printing and photopatterning [26, 155–157].

The principle idea behind the microcontact printing technique is to use a stamp in the shape of the desired pattern that 'prints', i.e. transfers, proteins onto the substrate, see Fig. 2.4 (A). These stamps have dimensions in the order of a few centimetres and contain patterns of a spatial resolution of ca 1 micrometre. Stamps are typically made from polymers such as the relatively cheap polydimethylsiloxane (PDMS). The PDMS is poured in a negative mould that consists of a silicon (Si) wafer and a layer of photoresist. The photoresist had previously been illuminated in such a way that it cured everywhere but at the place of the pattern leaving a several micrometers deep negative mould. The PDMS in the mould is then cured and cut into stamps. The stamps are subsequently incubated with proteins. These stamps, with their protein-coated side, are then placed onto the substrate to transfer the protein. Generally, the protein is simply physisorbed onto the surface. The areas between the adhesive patterns can be blocked or passivated by filling the negative spaces of the stamp with a blocking solution. Poly(L-lysine) grafted poly(ethylene glycol) (PLL PEG) is the most commonly used non-fouling system to prevent protein adsorption [158]. Microcontact printing is versatile, working with various ligands and substrates, including gold, silver, metal-oxide surfaces, glass, and various plastics. This versatility allows for the use of similar protocols with minimal adjustments to test the effects of different substrates and substrate stiffnesses on cell migration. Once established,

microcontact printing offers a reliable and economical method to produce micropatterns [112, 155, 156, 159, 160]. However, the method is difficult to scale because the stamps' size can't easily reach dimensions larger then a couple of square centimetres before bending too much and thereby distorting any micropatterns. Additionally, due to the fact that stamps are placed manually the positioning and level placement of stamps is reproducible only to a certain extent.

Photolithographic patterning techniques, or short photopatterning, involve the illumination of areas of the substrate that will turn into protein patterns, see Fig. 2.4 (B). The first step of the process is typically the application of a blocking solution followed by a layer of photo-activator to the substrate [160–165]. When the photoactive layer is exposed to ultraviolet (UV) or near-UV light, the passivation layer is removed by a photoscission mechanism, making the substrate locally receptive to ligands. The same effect can be achieved without a photo-activator by using deep UV light [166]. By illuminating an area in the shape of the desired pattern using either a mask or scanning with a UV beam, the passivation layer is removed in a negative pattern. This pattern is then filled with the desired ligands, which adhere to the substrate. Maskless projection lithography uses a digital micromirror device (DMD) to spatially modulate the light. The surface of a DMD chip is covered with an array of microscopic mirrors, with each mirror corresponding to a pixel that can quickly be turned on or off. This way images of pattern motifs can be projected on the substrate with a resolution of about one micrometre. Furthermore, DMDs make it possible to tune the UV dose for each pixel of the image via exposure time, resulting in different ligand densities. The 'brighter' a pixel, i.e. the longer it is illuminated, the more passivation is removed due to photoscission, which in turn leads to more accessible binding sites for ligands resulting in higher protein densities. While UV illumination via masks enables the scaling of a highly reproducible pattern production, maskless methods that scan the substrate with a beam excel in rapid prototyping. Pattern geometries can be easily tested by changing the digital design without the need for a new photomask [167]. However, while both photopatterning techniques require specialist equipment, maskless systems are much more expensive and more complex to operate.

Modulating ligand density, which is commonly used to tune cell adhesion strength, is more straightforward with photopatterning than with microcontact printing because the density depends on the illumination dose, which is easily controlled. However, photopatterning is limited to thin, UV-transparent substrates, making it challenging to pattern gel-coated substrates.

4 Basic Observations of Cells in 1D Confinement

One-dimensional (1D) assays have been instrumental in characterising various parameters of cell motility, including velocity, traction force, and response to environmental cues such as changes in ligand density [168]. Here, I provide an overview of key observations on migrating cells.

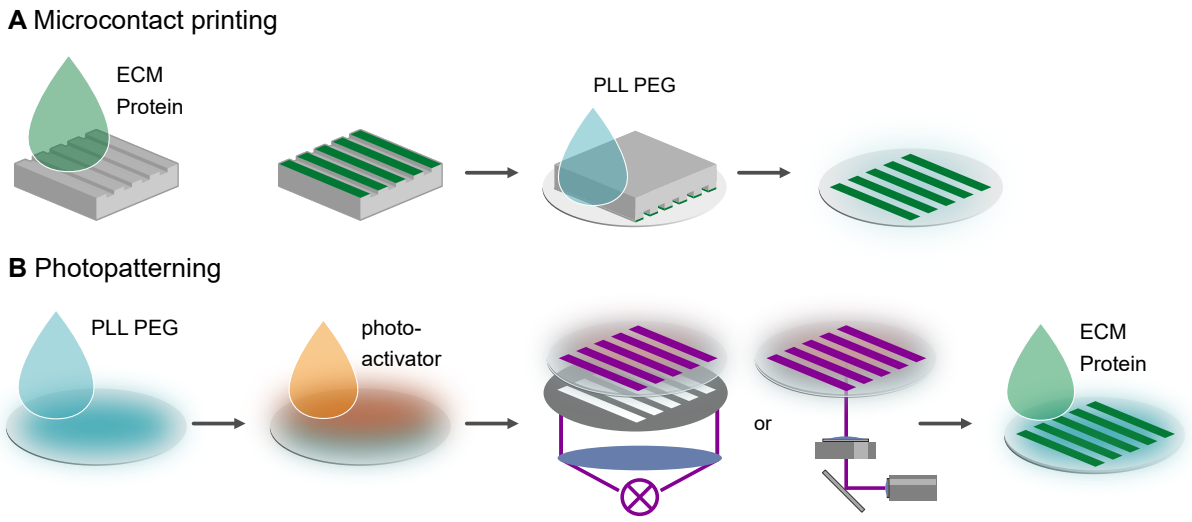

Figure 2.4: Microfabrication of 1D migration platforms. **(A)** In microcontact printing a PDMS stamp in the shape of the desired pattern 'prints' proteins of the extracellular matrix (ECM) onto the substrate. In a first step, the protein solution is applied to the stamp to cover the geometry of the pattern. The stamp then transfers the proteins to the negatively charged substrate. Negative space is backfilled with the non-fouling agent poly(L-lysine) grafted poly(ethylene glycol) (PLL PEG). **(B)** Photopatterning treats the substrate with (UV-)light to render it locally susceptible to ECM proteins. First, the substrate is passivated with a non-fouling coating. Second, a photoactive layer is added. Third, the desired pattern is either illuminated through a photomask or by scanning the substrate using spatially modulated UV-light. The photoactive layer removes the surface passivation upon treatment by UV-illumination. Now, the protein is added to the substrate and adheres to the treated areas. Adapted from Heyn et al. 2024 [3].

Cell behaviour is significantly influenced by the dimensionality of the substrate [169]. On ECM fibres or thin fibronectin lanes, cells adopt a uniaxial shape in the direction of confinement [145, 164, 170]. Cells move faster on 3D fibres compared to on 2D surfaces, and even faster on 1.5 µm wide fibronectin lanes. Fibroblasts show a biphasic velocity response to lane width, with maximal velocity at 2.5 µm and slower velocities on both thinner and wider lanes [164]. Different cell types, like human umbilical vein endothelial cells (HUVECs) and fish epithelial keratocytes, exhibit increased velocity with wider lanes [145, 153].

Another basic observation is that cells respond to environmental cues. One such response is the preference of cells for areas that provide a higher adhesion strength. This preference manifests itself in directed migration towards regions of high fibronectin density [144, 171–173]. Fibroblasts prefer 2D regions to 1D lanes due to their ability to exert larger traction forces [174]. This behaviour indicates a fundamental preference for tight adhesion, that affects the cell state via integrin signalling and the clutch mechanism between f-actin retrograde flow and stationary structures, see next Section. However, cells universally display a velocity peak at intermediate adhesion strength. The adhesion-velocity relation is hence biphasic. Initially, as adhesion increases, the velocity increases due to improved transmission of force to the substrate. But for movement, cells must detach the rear membrane from adhesion bonds, creating resistance and reducing velocity as adhesion intensifies [80, 81, 83, 84, 173, 175–177]. Cells can also alter their environment by secreting ECM proteins like fibronectin. This can create biochemical footprints that bias migration over time, as observed by d'Alessandro et al. for MDCK epithelial cells [171]. Memory effects are more pronounced in strongly secreting cell lines and low initial protein concentrations on 1D lanes. The effect has not been reported for the MCF-10A and MDA-MB-231 cells studied in this thesis. Cells exhibit quasi-periodic motion due to polarisation changes when encountering non-adhesive ends on short micropatterned lanes [33].

Doyle et al. observed that adhesions are mainly regulated at the edges of the cell, which justifies why most modelling approaches focus on force generation at the protrusion rather than at the centre of the cell [164]. Cells exert similar magnitudes of traction forces at both front and rear, significantly exceeding the force required for movement [178–180]. Changes in traction forces at one end do not correlate with force changes at the other, suggesting that front contraction may not drive rear retraction. Protrusions at both sides of the cell are common, with rearward protrusions increasing the propensity for direction reversal. Front-rear interactions involve elastic spring forces, sufficient to affect the probabilities of protrusion collapse.

Maiuri et al. report a universal coupling between cell speed and cell persistence (UCSP) [32, 142]. Their analysis of 54 different cell types showed that, in both simple and complex migration scenarios, faster cells tended to follow straighter paths, that is, to move more persistently. Maiuri et al. suggest that the persistence time depends exponentially on cell speed, see Fig. 2.5 (B). This observation has since been confirmed by Leineweber and Fraley, who report comparable results for MDA-MB-231 cells [181].

An additional noteworthy observation is that both the shape and motility of cells

exhibit significant changeability. Cells intermittently stop and resume movement, form new protrusions, and change direction. This motility, in combination with the dynamic nature of front and back protrusions, defines the motile states of cells [121–127, 130, 133, 137, 138]. Observations have revealed stationary and oscillatory dynamic regimes involving one or more protrusions, sparking considerable interest in the concept of multistability within cell motility [63, 143, 182–184]. The multistability of these dynamic states, characterised by state transition dynamics, the biphasic adhesion-velocity relationship, and the UCSP, seems to accurately represent motile behaviour across a wide variety of cell types [81, 142, 173, 175].

5 Biophysical Modelling

The field of cell mechanics and motility modelling is very active and diverse. However, there are certain recurring aspects of modelling that I will present here. Models of cell migration can broadly be divided into two categories: statistical models, that focus on the random walk-like nature of cell trajectories, and mechanistic models that concentrate on (mechanical, chemical) intracellular mechanisms. The mathematical model of each study depends on the cell behaviours, properties, and biological hypotheses on motility and morphodynamics that are being examined. Detailed reviews of modelling approaches that go beyond the scope of this thesis have been published in [23, 185–187].

In statistical models, cells are viewed as Brownian particles with an emphasis on the mean squared displacement (MSD) C_{MSD} defined as:

$$C_{\mathrm{MSD}}(t) = \langle (x(0) - x(t))^2 \rangle. \tag{2.1}$$

For a passive Brownian particle, the MSD is proportional to the time t as

$$C_{\mathrm{MSD}}(t) = 2nDt \tag{2.2}$$

in n dimensions and with the diffusion constant D. The diffusion constant D can theoretically be determined by the Einstein relation between the friction (γ) of a moving object and its environment at temperature T. If the particle is a perfect sphere of radius r, the viscous friction can be calculated as $\gamma = 6\pi\eta r$ with the viscosity of the solution η and the Boltzmann constant k_{B}

$$D = \frac{k_{\mathrm{B}}T}{\gamma} = \frac{k_{\mathrm{B}}T}{6\pi\eta r}. \tag{2.3}$$

However, cells are neither perfect spheres nor do they move passively (in the context of mesenchymal migration). They are irregular shaped, active objects that operate far from equilibrium. Observations have shown that their MSD resembles that of a persistent random walk (PRW), see Fig. 2.5 (A) [187, 188]. The MSD of the PRW is

$$C_{\mathrm{MSD}}(t) = 2V\tau_{\mathrm{p}}(t - \tau_{\mathrm{p}}(1 - e^{-t/\tau_{\mathrm{p}}})) \tag{2.4}$$

with the mean squared velocity V and the persistence time τ_{p}. Mitterwallner et al. evaluated the validity of PRW models in cell motion by employing a Langevin equation with a general memory kernel for velocity dynamics [189]. They observed slight negative friction on short time scales, but otherwise, the cell motion adhered to a persistent random walk. Persistence times, obtained from trajectories, vary by over two orders of magnitude, showing significant cell behavioural diversity. Chapter 4 will expand on these findings.

D'Alessandro et al. modified the PRW model to show that cells prefer staying on a fibronectin layer they deposit during movement [171]. This is modelled by increasing the likelihood of cells re-entering areas they previously visited and where fibronectin was deposited, utilising a persistent self-attracting random walk (PSATW) approach. At a domain's edge, cells are more prone to turn back rather than crossing over, causing a back-and-forth motion along the domain. Experimentally, the domain expands with each boundary visit, whereas in PSATW simulations, domain expansion occurs when cells cross boundaries. This model successfully replicates the observed experimental trajectories.

Mechanistic models focus on intracellular mechanisms to explain motile behaviour and may incorporate chemical reaction networks, Fig. 2.5 (C), and / or mechanical elements, Fig. 2.5 (D). Because actin polymerisation is an essential part of mesenchymal cell migration, f-actin network dynamics is also an essential part of many models. The polymerisation of actin fibres at the protrusion edge is modelled as a ratchet that pushes the cell membrane forward [57, 58, 190]. Bolado-Carrancio et al. investigated the dynamics of polymerisation by studying a signalling network comprising the small GTPases Rac1 and RhoA, the kinases ROCK and PAK, and Diaphanous related formin-1 (DIA) [137]. The network shows oscillations in GTPase concentrations that influence polymerisation and contraction activation. Complex feedback creates various state cycles, with a RhoA/Rac1 cycle leading at the cell front and a RhoA/ROCK cycle at the back, Fig. 2.5 (C). Maiuri et al. use actin network dynamics to explain the universal coupling between cell speed and cell persistence (UCSP), which suggests an exponential dependence of persistence time on cell velocity, Fig. 2.5 (B) [142]. Their model is based on two essential assumptions. The first posits that the polymerisation rate, which dictates retrograde flow velocity within the cell, is regulated by a polymerisation inhibitor binding to f-actin. This inhibitor, carried away from the leading edge by retrograde flow, halts edge movement when a critical threshold is reached due to random fluctuations. The statistics of this stochastic event manifest the UCSP. However, the f-actin-binding inhibitor is not specified. Maiuri et al. derive an exponential relationship between persistence time and retrograde flow velocity based on this inhibitor's advection. The second assumption is that cell velocity v is directly proportional to retrograde flow velocity v_r, expressed as $v = \alpha v_r$, with a constant α. Consequently, persistence time also exhibits an exponential dependence on cell velocity.

Another important component of many models is the force balance at the leading edge of the cell. Here, friction between the retrogradely flowing f-actin network and stationary structures in the lab frame of reference are essential, Fig. 2.5 (D). This process is often modelled as a non-linear clutch controlled by integrin signalling [191]. The clutch mecha-

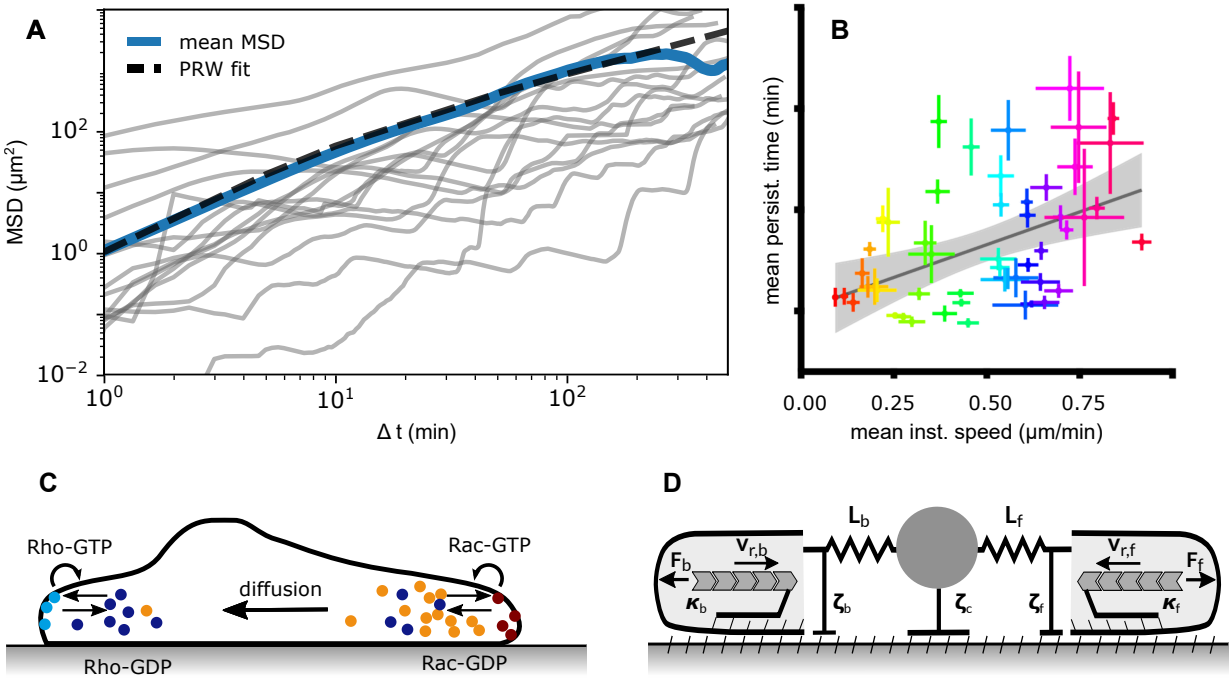

Figure 2.5: Mathematical modelling of mesenchymal cell migration. **(A)** Models considering cells as active Brownian particles with random motion analyze the mean squared displacement (MSD) from trajectories, such as those shown from MDA-MB-231 human breast cancer cells, with N = 15. The blue line indicates the population's average MSD, while the dashed line shows a fitted persistent random walk (PRW) with a persistence time $\tau_\mathrm{p} = 5\,\mathrm{min}$. **(B)** Universal coupling between cell speed and cell persistence (UCSP). Each dot marks the average persistence time and average instantaneous speed of a single cell line. Adapted from Maiuri et al. 2015 [142]. **(C)** Mathematical models based on signalling networks focus on chemical reaction descriptions, transport, and diffusion of reactants, and consider concentration profiles of pathway components. Illustrated is a prototypic system of bound/unbound RhoGTPases. **(D)** Mechanical models, such as the one introduced in Chapter 5, describe cellular dynamics with forces ($F_\mathrm{f,b}$), membrane tension (elastic springs), f-actin network flow ($v_\mathrm{r,f,b}$), drag ($\zeta_\mathrm{f,c,b}$) and friction ($\kappa_\mathrm{f,b}$ that affect protrusions and the cell body. Figure adapted from Heyn et al. 2024 [3].

nism can explain the biphasic adhesion-velocity relation and oscillations of protrusion length [138, 183, 184, 192, 193]. Sens presents a model that connects two protrusions containing a clutch by an elastic spring that represents the tension of the membrane [184]. The model of Ron et al., built on the model of Maiuri et al., posits a polymerisation inhibitor dispersing through the cytosol and interacting with f-actin to regulate polymerisation in two protrusions [183]. Both models report the coexistence of multiple motile states for the same respective parameter set. Our observation of spontaneous state transitions will also motivate us to incorporate a non-linear clutch mechanism in our biophysical model, see Chapter 5.

6 Simulation-Based Inference

Assuming that we have a mechanistic model that can simulate the trajectory of a cell, expressed as vector $\mathbf{x}$, by sampling from an input vector of parameters θ, can we inverse the approach and infer the parameter values θ that are the most plausible given an observed trajectory $\mathbf{x}$? This question is at the centre of the field of scientific inference. Inferring θ from experimental data is often necessary to validate theoretical models or compare model-based characterisations of cell motility. The solution to the inverse problem depends a lot on the context and the design of the mechanistic model. Simulation-based inference (SBI) is a method that can be useful if the underlying system is complex and traditional inference methods are not applicable or computationally intractable. In the following I will give an introduction to SBI, explaining how it works, when it is applicable and what it's advantages are.

Statistical analysis provides a powerful toolbox for scientific investigation and statistical inference is one of its most important tools. The goal of statistical inference is "[...] to infer properties of an underlying distribution of probability" [194]. The inference results should be appropriate for an unprejudiced observer, i.e. they should be unbiased and comprehensible. There are two main approaches to statistical inference, namely the *frequentist* and the *Bayesian* approach that differ in their interpretation of uncertainty [195]. The frequentist perspective primarily seeks to determine the probability of observing a given data set under the assumption of the null hypothesis. In contrast, the Bayesian methodology assesses the probability of a hypothesis in light of a specific data set [195]. For reasons of brevity I will focus here on Bayesian inference.

A function $p(\cdot)$ that takes an arbitrary vector $\mathbf{x}$ and outputs the density at $\mathbf{x}$ is called a *probability-density function* or *probability-density distribution*. Density functions must integrate to 1:

$$\int p(\mathbf{x})\mathrm{d}\mathbf{x} = 1 \tag{2.5}$$

In the context of this thesis, the vector $\mathbf{x}$ usually describes an experimentally observable variable or *data*. These data can be generated by a statistical model, a so-called *simulator*, that takes in parameters θ and puts out a data vector $\mathbf{x}$ from the conditional density $p(\mathbf{x} \mid \theta)$: $\mathbf{x} \sim p(\mathbf{x} \mid \theta)$. Examples could be an equation of motion that takes in parameters such as the initial position x_0 and velocity v_0 of a cell to compute the position of the cell $x(t)$ at time t. The statistical model might also incorporate additional variables $\tilde{\mathbf{x}}$ that are unmeasured but potentially observable and are referred to as missing or *latent* data, along with relatively fixed components of the data-generating process serving as covariates [196]. In the example of the equation of motion for a cell, this could be drag $F_{\mathrm{drag}}(v)$ that depends on the velocity v of the cell. The model calculates latent states $\tilde{\mathbf{x}}_i \sim p_i(\tilde{\mathbf{x}}_i \mid \theta)$ and, using the latent states, then the final data $\mathbf{x} \sim p(\mathbf{x} \mid \theta, \tilde{\mathbf{x}})$. This means that the joint distribution $(\mathbf{x}, \tilde{\mathbf{x}})$ depends on the parameters θ. This dependence can be expressed by factoring the joint distribution $(\mathbf{x}, \tilde{\mathbf{x}}, \theta)$ into a *prior* distribution $p(\theta)$ and the *complete-data likelihood* $p(\mathbf{x}, \tilde{\mathbf{x}} \mid \theta)$ [196]. The complete-data likelihood contains information about all latent states,

so that we can write

$$p(\mathbf{x} \mid \theta) = \int p(\mathbf{x}, \tilde{\mathbf{x}} \mid \theta) \mathrm{d}\tilde{\mathbf{x}} \tag{2.6}$$

using the definition of the density function, see Eq. 2.5. The density function $p(\mathbf{x} \mid \theta)$ is commonly referred to as *likelihood* (without "complete-data"). In real-world scenarios, the likelihood is often intractable, e.g. because one does not have access to $\tilde{\mathbf{x}}$ and therefore can't integrate over all $\mathrm{d}\tilde{\mathbf{x}}$. This poses a challenge because the likelihood is necessary to apply Bayes' Theorem to compute the posterior distribution $p(\theta \mid x)$:

$$p(\mathbf{x} \mid \theta) p(\theta) = p(\mathbf{x}, \theta) = p(\theta \mid \mathbf{x}) p(\mathbf{x}) \tag{2.7}$$

which is commonly written as

$$p(\theta \mid \mathbf{x}) = \frac{p(\mathbf{x} \mid \theta) p(\theta)}{p(\mathbf{x})}. \tag{2.8}$$

The Bayes' Theorem updates what we know about the probability of θ from the prior distribution $p(\theta)$ (without knowledge of the data) by incorporating knowledge about the likelihood of observing $\mathbf{x}$ given θ, $p(\mathbf{x} \mid \theta)$, to arrive at the posterior distribution $p(\theta \mid \mathbf{x})$ (includes knowledge of the data). For a comprehensive textbook on Bayesian Inference see for example G. E. P. Box and G. C. Tiao [197] or A. Stuart, K. Ord [198].

As mentioned above, estimating the posterior distribution $p(\theta \mid \mathbf{x})$ without access to the likelihood function $p(\mathbf{x} \mid \theta)$ is a common challenge in stochastic models that try to simulate real-life processes. Fortunately, a number of inference techniques have emerged that are likelihood-free or *simulation-based* [199–201].

$$\begin{aligned} \theta &\rightarrow \text{simulator} &&\rightarrow \mathbf{x} \\ \mathbf{x} &\rightarrow \text{simulation-based inference} &&\rightarrow \theta \end{aligned}$$

Posterior density estimation approaches frame the likelihood-free inference problem as a machine learning task that can be solved by training a neural network on data generated by the simulator. The idea is to map $\mathbf{x}$ onto an estimate of $p(\theta \mid \mathbf{x})$. To this end, G. Papamakarios and I. Murray have developed a parametric approximation to the exact posterior called sequential neural posterior estimation (SNPE) [202]. The posterior distribution is derived from a family of density functions denoted by $q_\Psi(\theta)$, with Ψ representing their parameters. This distributional mapping from $\mathbf{x}$ to Ψ is learned by adjusting the weights Φ of a neural network F such that $q_{F(x,\Phi)}(\theta) \approx p(\theta|\mathbf{x})$. The network is trained by simulating datasets $\{(\theta_j, \mathbf{x}_j)\}$ using parameters drawn from a proposed prior $\theta \sim \tilde{p}(\theta)$ and minimising the loss function

$$\mathcal{L}(\Phi) = -\Sigma_{j=1}^{N} \log q_{F(\mathbf{x}_j,\Phi)}(\theta_j)$$

with respect to the network weights Φ [202]. The process will result in learning the mapping from $\mathbf{x}$ to the posterior $p(\theta \mid \mathbf{x})$ as $N \rightarrow \infty$. Post-training, the target posterior $p(\theta \mid \mathbf{x}_o)$

is estimated for the observed data $\mathbf{x}_o$ with $q_{F(\mathbf{x}_o,\Phi)}$. To minimise computational cost, the algorithm should run only simulations that are informative about $\theta \mid \mathbf{x}_o$. This is achieved by sampling from a *proposal prior* $\tilde{p}(\theta)$ that is constructed to yield values in the vicinity of $\mathbf{x}_o$ [202, 203]. However, this leads no longer to the real posterior $p(\theta \mid \mathbf{x})$ but the *proposal posterior* $\tilde{p}(\theta \mid \mathbf{x})$:

$$\tilde{p}(\theta \mid \mathbf{x}) = p(\theta \mid \mathbf{x}) \frac{\tilde{p}(\theta) p(\mathbf{x})}{p(\theta) \tilde{p}(\mathbf{x})} \tag{2.9}$$

with $\tilde{p}(\mathbf{x}) = \int_\theta \tilde{p}(\theta) p(\mathbf{x} \mid \theta)$ [204]. Due to certain limitations, the original algorithm by G. Papamakarios and I. Murray had to be adjusted to be fully generalised and applicable even to multimodal inference problems while still being fast, accurate and requiring little data [203, 204]. The latest version of the algorithm, developed by D. Greenberg et al. [204] and called SNPE-C, defines the loss function in the following way. A family of proposal density functions is constructed:

$$\tilde{q}_{\mathbf{x},\Phi}(\theta) = q_{F(\mathbf{x},\Phi)}(\theta) \frac{\tilde{p}(\theta)}{p(\theta)} \frac{1}{Z(\mathbf{x}, \Phi)} \tag{2.10}$$

with the normalisation constant $Z(\mathbf{x}, \Phi)$. The new loss function that is to be minimised therefore becomes:

$$\tilde{\mathcal{L}}(\Phi) = -\Sigma_{j=1}^{N} \log \tilde{q}_{\mathbf{x},\Phi}(\theta_j). \tag{2.11}$$

Algorithm 1 SNPE-C (see Greenberg et al. for more details [204])

Require: simulator with density $p(\mathbf{x} \mid \theta)$, data $\mathbf{x}_o$, prior $p(\theta)$, density family q_Ψ, neural network $F(\mathbf{x}, \Phi)$, N simulations per round, R rounds

```
p̃_1(θ) ← p(θ)
for r = 1..R do
    for j = 1..N do
        sample θ_{r,j} ~ p̃_r(θ)
        simulate x_{r,j} ~ p(x | θ_{r,j})
    end for
    Φ ← arg min_Φ Σ_{i=1}^{r} Σ_{j=1}^{N} − log q̃_{x_{i,j},Φ}(θ_{i,j})      ▷ Eqs. 2.10, 2.11
    p̃_{r+1}(θ) ← q_{F(x_o,Φ)}(θ)
end for
return q_{F(x_o,Φ)}(θ)
```

The architecture chosen for the implementation of this density estimation approach depends on the use case, but Mixture-Density Network (MDN) [205] and Masked Autoregressive Flow (MAF) [206] have been reported as successful approaches in the relevant literature [207–211]. To mitigate overfitting issues arising from the limited training data available in each round, the MDN can employ variational dropout for training [212]. One significant benefit of SBI is that the inference utilises the same trained network for all experimentally obtained data points, unlike traditional numerical optimisation which requires

a separate inference algorithm for each trajectory. Although network training involves substantial computational resources, the inference process itself is not resource-intensive.

SNPE-C can hence be employed to estimate the parameter distribution of observed data according to a mechanistic model. For applications in the domain of biophysics, see for example [209, 213]. Fig. 2.6 represents the workflow of SBI for a biophysical model of single cell migration. The model is used as a simulator that generates N pairs of parameters and trajectories $\{(\theta_j, \mathbf{x}(t)_j)\}$ by sampling from a prior $p(\theta)$. In the absence of more detailed information, the initial prior may be uniform within a range of possible parameter values and equal to zero outside this range. The proposal prior will be adjusted at the end of each training round r to focus on values of θ that are the most informative for the posterior, see Alg. 1. The simulated trajectories are fed into a deep neural network that may use a convolutional neural network (CNN) to obtain a latent feature vector, also known as *embedding*. The extracted features are then fed into the neural density estimator (NDE) that is trained to optimise the loss function as defined in Eq. 2.11 by comparing the estimated posterior θ to the one that was used for simulation θ_{true}. This process is repeated until the NDE estimates the posterior distribution to the desired accuracy. Once the NDE is trained and well calibrated, the simulated trajectories can be swapped for experimental data. The CNN extracts the summary features of the experimental trajectories and the NDE estimates the posterior density distribution $p(\mathbf{x}_o \mid \theta)$. Hence, SBI can estimate the optimal set of model parameters that characterises an experimental trajectory, concurrently evaluating the associated uncertainty.

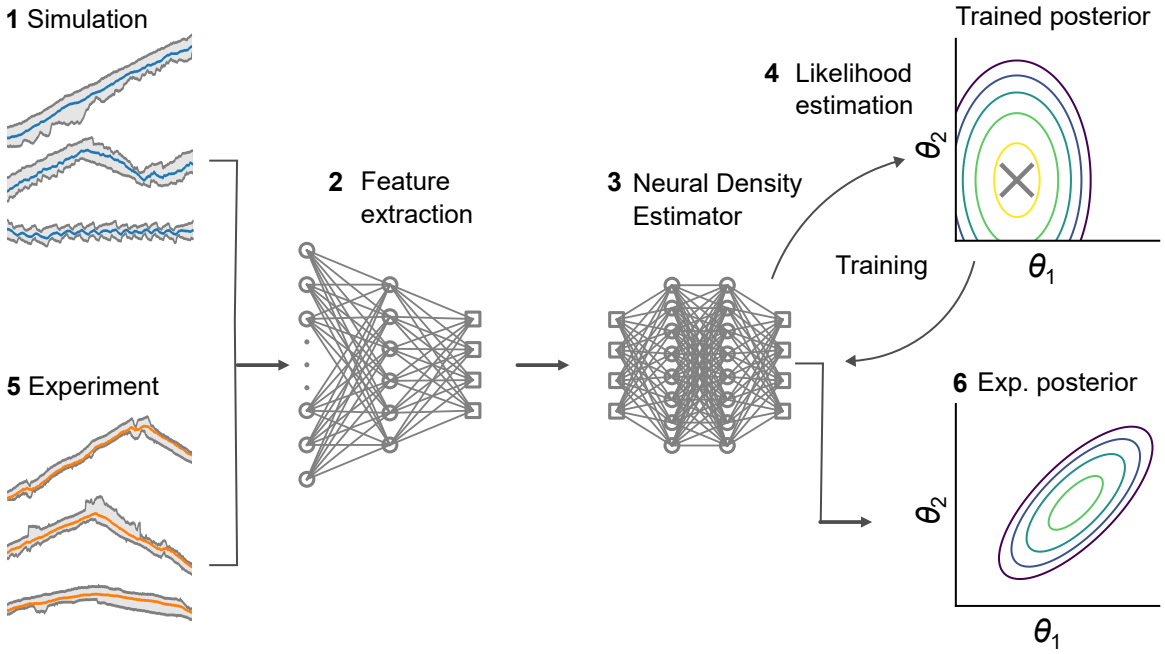

Figure 2.6: Simulation-based inference (SBI) of posterior distributions. A diagrammatic overview of the SBI process shows a neural network initially trained on simulated data, which is later used for analysing experimental data, see Alg. 1. **(1)** Parameters θ are randomly selected from the prior distribution $p(\theta)$ to generate simulated trajectories $\mathbf{x}(t)$. **(2)** These trajectories are converted to a low-dimensional feature space using a convolutional neural network (CNN). **(3)** This condensed trajectory is then processed by the neural density estimator (NDE), which estimates the posterior density. **(4)** The log-likelihood of the NDE at the actual parameter point ($\mathbf{X}$) serves as the loss function to refine the NDE, see Eq. 2.11. The maximum likelihood of the trained NDE aligns with the true parameter point indicated by 'X'. Next, the trained SBI algorithm is applied to estimate parameters from empirical data. **(5)** Experimental trajectories are reduced to a low-dimensional feature space by the same CNN as utilised in step (2), then input into the previously trained NDE. **(6)** The derived posterior highlights a cell-specific parameter estimation that elucidates interpretable cell characteristics as per the biophysical model. Adapted from Heyn et al. 2024 [4].

Development of a Setup for Standardised High-Throughput Experiments

A quantitative understanding of mesenchymal cell migration and its underlying mechanisms requires a large ensemble of single-cell trajectories. Intrinsic noise is a fundamental aspect of many biological processes, manifesting itself as cell-to-cell variability in the context of cell migration [214–216]. A considerable diversity of migratory behaviours is observable within cell populations. Consequently, many cell trajectories are needed to identify patterns that are universal across mesenchymal cells or characteristic for certain cell lines. DiMilla et al., who were among the first to experimentally quantify the biphasic adhesion-velocity relation in 1993, tracked several hundred cells for their study [173]. The First World Cell Race, which led to the discovery of the universal coupling between cell speed and cell persistence (UCSP), analysed the trajectories of more than 7,000 cells on 1D lanes in 2012 [32, 142]. For our quantitative analysis of motile states in MDA-MB-231 cells, we used more than 20,000 cell trajectories [2]. This was necessary because of the rarity of certain state transitions, as I will discuss in Chapter 5.

Temporal and cell-to-cell variability are fundamentally attributed to intrinsic cellular properties that fluctuate over time or vary among different cells, such as alterations in protein concentrations or localisation. However, migrating cells additionally experience variability in their external environment, including heterogeneity in the extracellular matrix (ECM). This problem can be addressed by controlling the environment of cells via microfabrication. Microfabricated migration platforms, such as 1D lanes, provide control over the homogeneity of ligands, the stiffness of the substrate and the concentration of supplements in cell culture media. In this way, standardised and reproducible conditions can be ensured.

Once cells are seeded and begin migrating on the microfabricated platform, their movement has to be recorded for later analysis. Data acquisition should align with the scientific question being addressed. The method of acquisition should be optimized to capture the greatest number of individual cell trajectories, all while meeting the spatio-temporal demands of the research question, and considering additional constraints like phototoxicity and photobleaching [217]. Modern scanning time-lapse microscopes can be set up to meet these requirements.

After the acquisition of the time-lapse videos of migrating cells, the data need to be

processed to retrieve the information that will answer the scientific question. Typically, only the coordinates of the front, nucleus and back of the cell over time $x_{f,n,b}(t)$ are of interest. Hence, the cells need to be segmented, tracked and the trajectories filtered to include only valid single-cell data. Ideally, this process is fully automated and scalable to achieve the required throughput. Due to the large amount of data involved in cell migration studies, an appropriate storage solution and data management system should be in place, which allows to easily retrieve, analyse and compare numerous measurements.

This chapter covers the setup which I developed to address all the requirements for standardised high-throughput experiments for the study of single-cell migration. In the final setup, a single experiment, conducted over the course of 48 h, yielded approximately 20 000 h of filtered trajectories from 1 000 cells. With the microfabrication of the migration platform before the experiment requiring one day of work and the data analysis after the experiment requiring another two days, i.e. a week in total per experiment, the setup made it possible to acquire enough data to answer various questions of cell migration within a few weeks. Additionally, the majority of steps in the acquisition process were designed for parallelisation, allowing multiple experiments to be run at the same time, further reducing the time to collect sufficient amount of data.

1 Microfabrication of 1D Migration Platforms

Initially, I produced cell migration assays using a microcontact printing protocol. Microcontact printing involves the use of a polymer stamp shaped like the target pattern to transfer proteins onto a substrate, see Fundamental Concepts. The coating protein in this thesis was fluorescently labelled FN if not stated otherwise. Fluorescence labelling made it possible to visualise the pattern under a fluorescent microscope and determine the density of fibronectin by fluorescent intensity. The respective protocols can be found in Materials and Methods. The microcontact printing protocol was quick, inexpensive and already well established in our laboratory when I started my work. Data acquired for Chapters 4 and 5 are from experiments using microcontact printing. However, the technique had multiple drawbacks that ultimately led me to switch to photopatterning. Control over FN density is limited with microcontact printing. The density is typically set by the FN concentration of the protein solution that is used as ink. However, the density also depends on various other factors, such as the duration of the transfer, the surface treatment of both the stamp and the substrate and the pressure with which the stamp is applied to the surface. As a consequence, the resulting FN density varies with each batch of fabrication even when the same FN concentration is used for the protein solution. Furthermore, the physisorption of the protein to the substrate via van der Waals forces may vary locally significantly, leading to inhomogeneous patterns. These inhomogeneities are problematic since they constitute perturbations to cells that migrate along an FN lane [1]. Additionally, the technique does not easily allow to print more than one FN density. There are versions of the protocol for fabricating patterns of two different FN densities, see Materials and Methods, but more than two densities, or even a density gradient, are

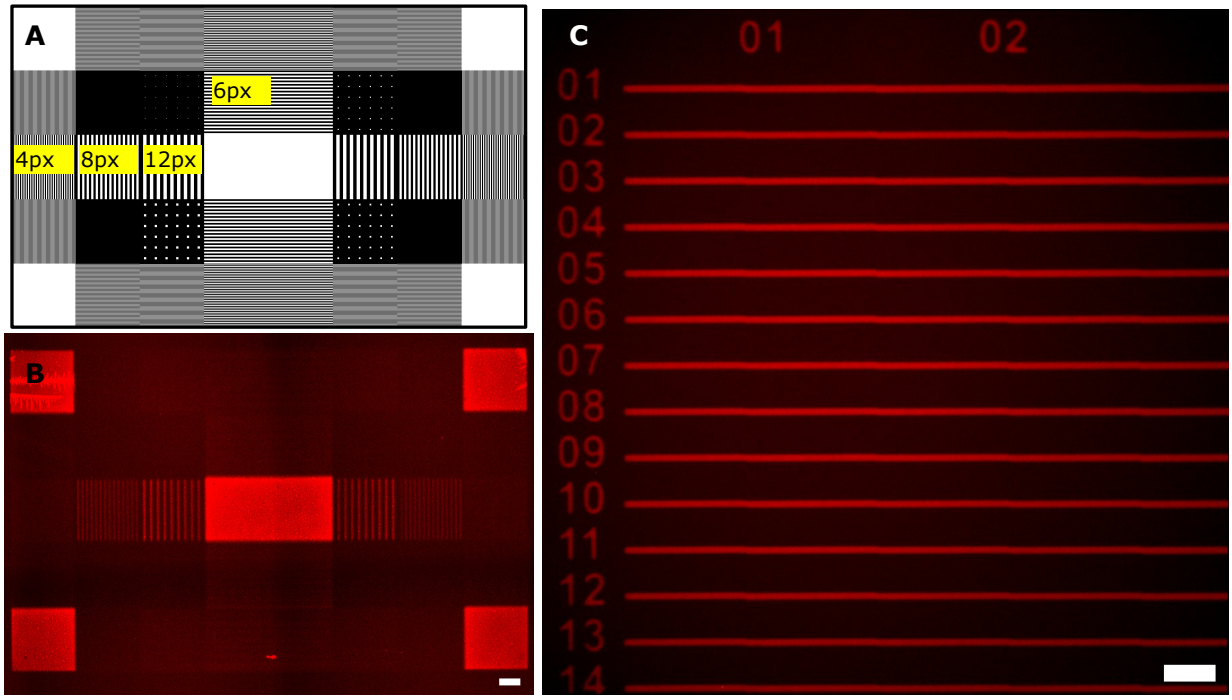

Figure 3.1: Photopatterning results with the Primo device. **(A)** Digital motif of a test pattern designed to test the spatial resolution in vertical and horizontal patterning direction of the Primo device. Annotations in yellow, which are not part of the motif, indicate the width of the white lanes in pixels. **(B)** Corresponding fluorescent FN pattern to the motif in (A). The motif was projected onto the photoactive layer on the imaging dish. Areas that were illuminated, i.e. white areas of the motif, were susceptible to the labelled FN. The spatial resolution allowed to resolve lanes with a width of a few micrometers ($\approx 5\,\mu m$). Structures smaller than that, e.g. the lanes with a width of 4 px, appeared only as a blur. **(C)** Photopatterning with the Primo device produced homogeneous straight FN lanes that could easily be adjusted to all kinds of needs. In this case, a lane numbering was added to facilitate recovering a position on the lane. A typical use case for this scenario would be retrieving fixed cells after a time-lapse measurement. Scale bars in (B,C) represent 100 µm.

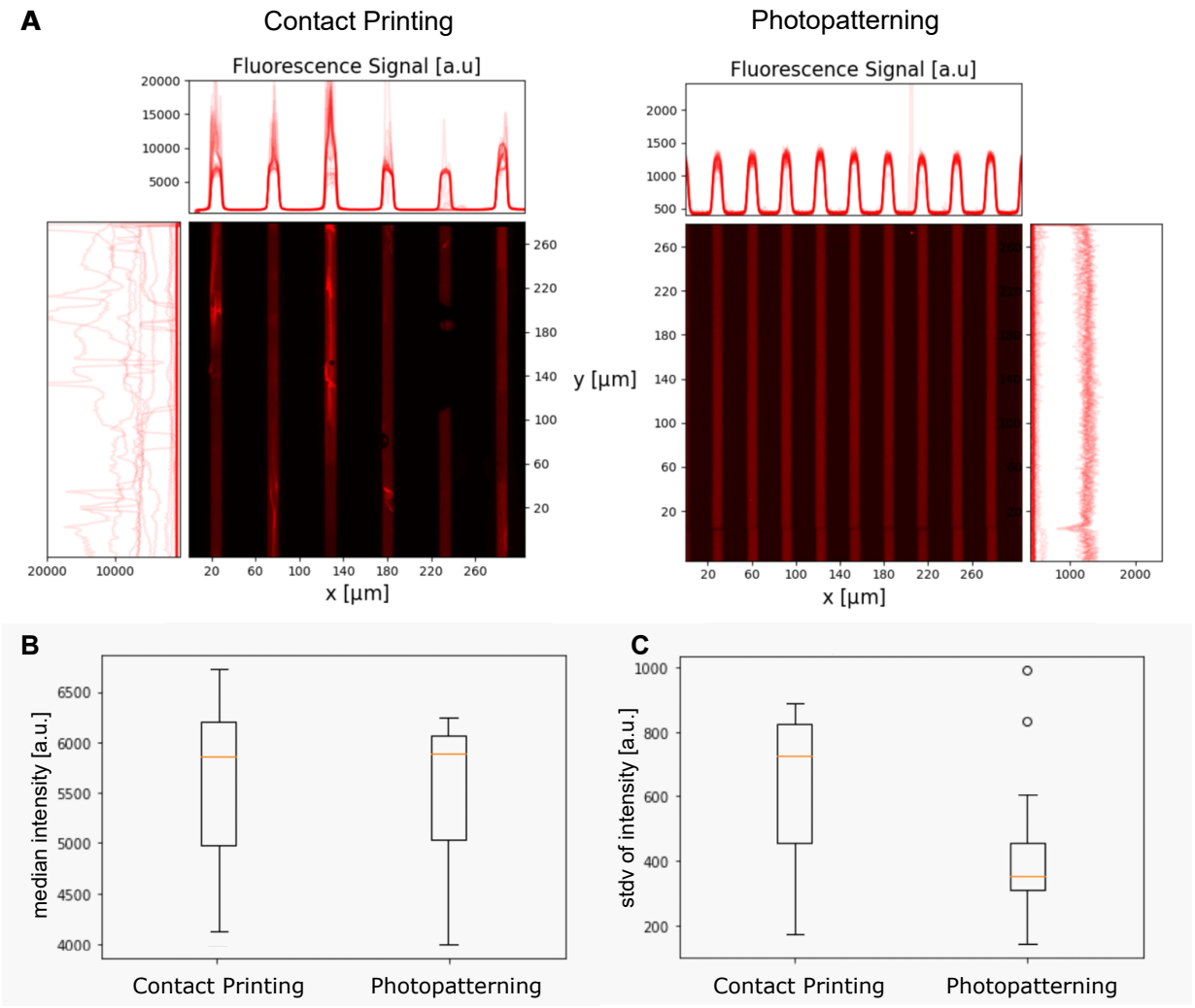

Figure 3.2: Comparison of microfabrication protocols. **(A)** Fluorescence images showcasing fibronectin lanes created via microcontact printing (left) and Primo photopatterning (right). Above these images are intensity profiles measured along 40 lines in the x direction, while to the side, there are 40 intensity profiles measured in the y axis. Adapted from M. Atienza Juanatey 2023 [218]. **(B)** Median intensity of microcontact printed vs photopatterned pattern. The fibronectin density, as measured as fluorescent intensity, can be matched between the two protocols which is important if photopatterning is to replace the microcontact printing protocol. **(C)** Standard deviation of the fluorescence signal. Within a single fibronectin (FN) lane the standard deviation is much lower for patterns created with photopatterning. Photopatterned lanes are more homogeneous than their microcontact printed counterparts.

practically not feasible. Also, for every new pattern design, a new stamp mould needs to be manufactured. This makes prototyping time consuming and expensive. And on top of all that, the fabrication of migration assays is not scalable using microcontact printing because of the manual placement of the stamps.

In recent years, photopatterning has emerged as an increasingly popular alternative to microcontact printing techniques, see Fundamental Concepts. I adapted a photopatterning protocol initially developed by Strale et al. and Studer [167, 219], where a polymer brush functions as an anti-fouling layer that is ablated using benzophenone and UV illumination. Illuminating the polymer brush in the presence of benzophenone makes it adhesive, facilitating the subsequent adhesion of FN. As illumination device, I used a Primo 2 module (Alvéole) mounted on an Eclipse Ti microscope (Nikon, Tokyo, Japan) which allowed a precise spatial modulation of the UV-illumination. The protocol can be found in Materials and Methods.

The Primo module is a maskless illumination device that allows one to pattern grey scale motifs that can be designed with very little constraint, see Fig. 3.1. Each pixel in the motif is assigned to a mirror in the digital micromirror device (DMD) of the Primo. The translation of the pixel size from the motif to the protein pattern depends on the magnification of the objective used to illuminate the photoactive layer on the imaging dish. For a 4x magnification, the conversion is approximately 1.3 µm/px, while it is 0.5 µm/px for 10x and 0.3 µm/px for 20x magnification. Panel (B) in Fig. 3.1 shows the result of transferring the motif in (A) with a 4x magnification, which is sufficient to spatially resolve up to a few micrometres. The 1D lanes that I produced for this thesis typically had a width of 15 µm. Therefore, the spatial resolution achieved with a 4x magnification objective was sufficient and my preferred setting. Although larger magnifications might have provided even greater resolutions, they would have also increased production times due to the smaller illuminated motif area, requiring the Primo device to take additional steps to scan the imaging dish. An advantage of the photopatterning protocol compared to microcontact printing is its flexibility. The design can be easily modified, adapted, and refined, allowing for the optimisation of factors such as the ideal spacing between FN lanes, which varies by cell type. It also enables the addition of markers to identify the location of specific cells after completing a time-lapse measurement, as illustrated in Fig. 3.1 (C).

A direct comparison of photopatterned and microcontact printed patterns reveals that photopatterning produces significantly more homogeneous lanes, see Fig. 3.2. Although both methods yield lanes with a sharp side edge at the transition from FN to the antifouling layer, the intensity of the fluorescence signal and therefore the FN density varies significantly along the printed lanes. Hence, when it comes to the fabrication of homogeneous patterns, the Primo photopatterning technique is clearly preferable to microcontact printing. Switching between the two techniques was facilitated by the fact, that the photopatterning protocol was easily adjusted to produce patterns with the same FN density (measured as fluorescent intensity) as the microcontact printing protocol, see Fig. 3.2 (B).

However, the photopatterning protocol also had some disadvantages. The protocol consists of a number of steps that are more sensitive and error prone than the microcontact printing procedure. The antifouling layer could crystallise, negatively affecting

the micropattern. The photoactive gel needed to be evenly spread on the imaging dish; otherwise, the pattern would also be uneven. The optics of the Primo module had to be well aligned and focused to produce crisp patterns. If the motif was bigger than a single DMD field, the motif needed to be "stitched", that is, two DMD's would be placed right next to each other to produce a continuous pattern. This worked only after careful alignment of the beam, which made the production of long FN lanes challenging. For examples of possible pitfalls of the Primo photopatterning protocol, see Figs. B.1, B.2, B.3. Several parameters, such as the illumination dose, the concentration of the PEG in the antifouling coating, the concentration of FN in the protein coating and incubation times, had to be adjusted before patterning was possible. Additionally, the illumination process can take relatively long (>1 h) if a large area is to be patterned. Depending on the magnification of the objective used for the illumination, the dimension of the area that the DMD can illuminate at once is small (approximately 620 µm x 360 µm for a magnification of 20x) compared to the area of the imaging dish (radius 21 000 µm), requiring the Primo device to sequentially scan the dish.

Despite the limitations mentioned above, the Primo photopatterning technique led to patterns of superior quality compared with those produced by microcontact printing and offered almost endless options of pattern design to address various aspects of cell migration. These were the main reasons why I chose photopatterning for experiments in Chapter 6.

2 Time-lapse Optimisation

Data acquisition was achieved by scanning time-lapse light microscopy, employing both phase contrast and fluorescent imaging.

Phase contrast microscopy is a technique that enhances the visibility of transparent specimens by transforming variations in their refractive indices into contrast. This process involves specialized condenser and objective lenses to impart phase shifts to light as it moves through different areas of the specimen. While light passing straight through the sample remains unchanged, light that is diffracted and phase-altered by the sample's structures experiences phase changes. To boost image contrast, constructive interference is achieved between the diffracted and unchanged light. This is done by sending background light through a phase ring, which alters the light by a quarter of a wavelength. When the light is focused on the detector, this phase shift leads to constructive interference between the background light and the scattered light emanating from sample-filled regions in the field of view, thereby increasing brightness in these regions relative to those without the sample [220–222].

Fluorescence microscopy is a standard method employed in cell biology that uses fluorescent dyes or tagged molecules to visualise specific structures. This process begins with excitation light from a white-light source passing through an excitation filter, which allows only light of a particular wavelength capable of exciting the fluorophore to pass. Alternatively, the light source can already be monochromatic, which is the case for most

LED's and lasers, which makes the use of an excitation filter superfluous. The excitation light is then directed by a dichroic mirror and concentrated through the objective lens onto the specimen. When excited, the fluorescent molecules in the sample are temporarily elevated to a higher energy level. As they return to their normal state, they emit a photon of a longer wavelength. Some of this emitted light is captured by the objective and travels through the dichroic mirror and the emission filter, which block the excitation light while allowing the emitted light to reach the eyepiece or camera for viewing or capturing images. This technique, which uses the same objective lens for both excitation and emitted light paths, is known as epifluorescence [223–225]. Moreover, advancements in synthetic molecules and the application of genetically encoded fluorescent proteins, such as those labelled with green fluorescent protein (GFP), enable prolonged live imaging of cellular activities with exceptional spatial and temporal detail [217].

For the experiments in this thesis, cells were seeded into imaging dishes and incubated for 2 h to 3 h. When cells adhered to the patterns, the dishes were transferred to the imaging setup consisting of an inverted fluorescence microscope equipped with an XY-motorised stage, a so-called "Perfect Focus System" which kept the sample in focus, and a heating chamber set to 37 °C. The imaging protocol can be found in Materials and Methods. For most experiments, the data of interest were the position of the front, nucleus and back of the cell over time plus the local FN density in the vicinity of the cell. The FN density was not time-dependent, and the fluorescent intensity of the pattern was the same before and after the experiment. Therefore, it was not necessary to image the pattern at every time step. Instead, the fluorescent pattern was imaged once before the start of the experiment, which saved valuable acquisition time and avoided unnecessary, non-informative data. The position of the nucleus was recorded by epi-fluorescence imaging of the nuclear marker Hoechst 33342 or H2B mCherry and the position of the front and back of the cell along the lane by phase contrast imaging. To minimise the acquisition time, phase contrast images were performed using the same filter set as for the nuclear imaging, which avoided having to change filter cubes between images. The short acquisition times (in the order of 1 s) and the motorised stage allowed to scan the imaging dish and capture multiple fields of view per time step. The number of fields of view that could be captured and consequentially the number of recorded cell trajectories was limited by the temporal resolution. A temporal resolution of 10 min allowed to scan approximately 300 fields of view, while 30 s was only enough to scan up to 20 fields of view. Therefore, temporal resolution is among the biggest leavers to acquire large data and should be considered carefully. Another important setting is the magnification of the imaging. The higher the magnification the better is the spatial resolution (up to a certain degree) but the smaller is the field of view and hence the number of cell trajectories that can be recorded. I found 10x magnification to be the lowest magnification that still delivers enough spatial resolution to detect the nucleus, as well as the cell front and back. A single time-lapse measurement over 48 h with a 10x magnification and a temporal resolution of 10 min resulted in the acquisition of time stacks of thousands of cells. These cells needed to be segmented, tracked and the trajectories filtered, which is only scalable if this process is automated.

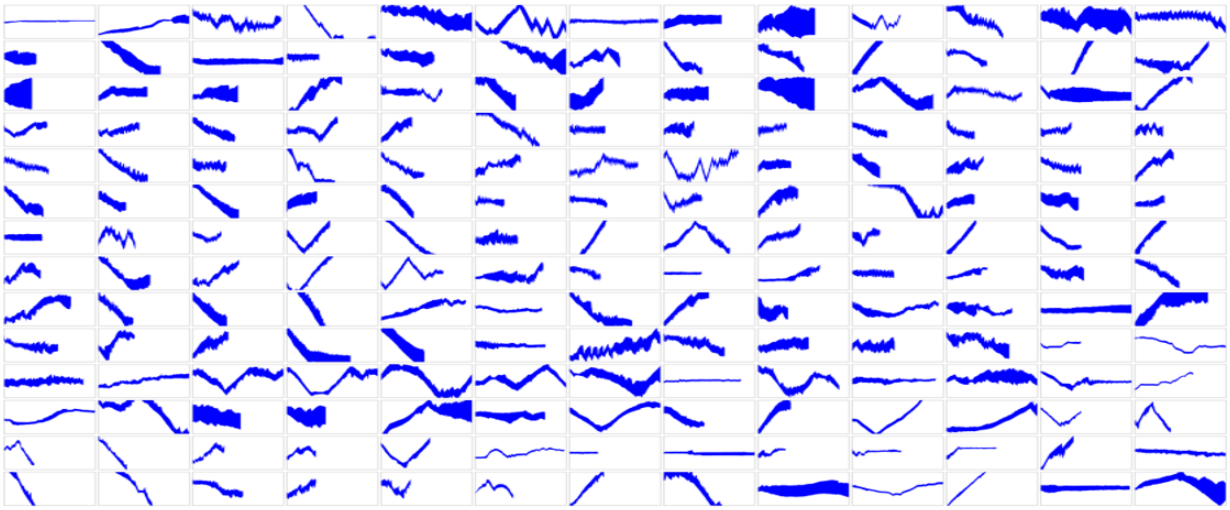

Figure 3.3: Standardised high-throughput experiments make it possible to acquire and analyse a large number of trajectories. Each panel depicts the kymograph of a single segmented MDA-MB-231 cell for 40 h, with time running from left to right. The 182 trajectories depicted here are only a small, randomly chosen selection of the more than 20,000 trajectories collected for this work. Visual inspection already hints at a large cell-to-cell variance of cell lengths, migration velocity and persistence time even within the same cell line and under identical experimental conditions.

3 Data Analysis Pipeline

Each measurement yielded time stacks with a size of a few hundred gigabytes. The relevant information in the acquired data, however, was only the FN density and the position of the cells with respect to the FN lane over time. To extract these informations, the positions of the FN lanes and of the nuclei were detected via a threshold to the fluorescent signals, see Materials and Methods. The positions of the nuclei were tracked and their coordinates transformed to align with the direction of the FN lanes. The detection of the front and back of cells from the phase-contrast images was more challenging because a simple threshold algorithm would not be able to identify the correct outline of cells. Therefore, I initially created kymographs of cells and manually traced the front and rear positions; see Fig. 2.3 for an example of a kymograph. However, this approach was time consuming and hardly scalable. Consequentially, I moved to an automated pipeline that employed the deep learning algorithm “cellpose” to automatically segment cells [218, 226, 227]. The segmentation and tracking still needed approximately 48 h even on a dedicated server (AMD EPYC 7402P 24-Core Processor with 256 GB DDR4 RAM and Nvidia RTX Titan 24GB GPU) but the work was no longer manual and could even be performed for multiple measurements at the same time. This made it possible to acquire and analysis a large number of trajectories, see Fig. 3.3.

Due to the substantial number of experiments (n>100), a data management system had to be established. The metadata was organised in compliance with the Cell Migration Standardisation Organisation (CMSO) reporting guidelines, specifically through the

	id	date ▾1	name	microscope	author_id	study_id	basic_approach	cell_model	ecific_cell_deta
	Filter	Filter	Filter	Filter	Filter	Filter	Filter	Filter	Filter
69	106	2022-12-02	221202_Ti2_RPE_10min	Ti2	1	2	in vitro	cell line	RPE, RPE My...
70	107	2022-12-07	221207_TIRF_RPE_10min	TIRF	1	2	in vitro	cell line	RPE, RPE My...
71	1	2023-03-22	230322_Ti2_FN-lanes_MDA_2min	Ti2	1	1	in vitro	cell line	MDA-MB-231 ...
72	2	2023-03-22	230322_TIRF_FN-lanes_MDA_2min	TIRF	1	1	in vitro	cell line	MDA-MB-231 ...
73	3	2023-03-22	230322_UNikon_FN-lanes_MDA_2min	UNikon	1	1	in vitro	cell line	MDA-MB-231 ...
74	4	2023-03-24	230324_UNikon_FN-fail	UNikon	1	1	in vitro	cell line	MDA-MB-231 ...
75	5	2023-04-06	230406_Ti2_MDAs_2min	Ti2	1	1	in vitro	cell line	MDA-MB-231 ...
76	6	2023-04-06	230406_UNikon_FN-lanes_MDAs_2min	UNikon	1	1	in vitro	cell line	MDA-MB-231 ...
77	7	2023-04-14	230414_Ti2_FN-lanes_MDAs_2min	Ti2	1	1	in vitro	cell line	MDA-MB-231 ...
78	8	2023-04-14	230414_TIRF_FN-lanes_MDAs_2min	TIRF	1	1	in vitro	cell line	MDA-MB-231 ...
79	9	2023-04-14	230414_UNikon_FN-lanes_MDAs_2min	UNikon	1	1	in vitro	cell line	MDA-MB-231 ...
80	10	2023-04-28	230428_Ti2_FN-lanes_MCF10A_10min	Ti2	1	1	in vitro	cell line	MCF 10A
81	11	2023-04-28	230428_UNikon_MCF10A	UNikon	1	1	in vitro	cell line	MCF 10A
82	12	2023-05-01	230501_Ti2_FN-lanes_MCF10A_10min	Ti2	1	1	in vitro	cell line	MCF 10A

Figure 3.4: Screenshot of experimental data base. The large number of experiments made it necessary, to implement a data management system. Metadata was stored according to the reporting guidelines of the Cell Migration Standardisation Organisation (CMSO), the so called Minimum Information About Cell Migration Experiments (MIACME) checklist. Using a database written in SQL made it possible to store, sort and filter the metadata either by code or via a graphical user interface such as the one seen in this screenshot (DB Browser for SQLite). The complete SQL data base of experimental meta data is accessible on my GitLab repository.

Minimum Information About Cell Migration Experiments (MIACME) checklist [228]. This included information about the experimental setup (cell type, treatment, etc.), the imaging condition (temporal resolution, magnification, etc.) and the data itself (number of fields of view, extrated trajectories, etc.). The use of a SQL-based database enabled the storage, sorting, and filtering of metadata, either by employing scripts or through a graphical user interface like the one displayed in Fig. 3.4. An SQL-version of my experimental data base can be found on my GitLab repository.

4 Discussion

The consistent improvement of the data acquisition and analysis towards a high-throughput of cell trajectories made it possible to retrieve several thousand trajectories per week. Except for the microfabrication of 1D FN lanes, the process could easily be parallelised by deploying multiple microscopes and computational resources at the same time. As a result vast amounts of data could be amassed which allowed a quantitative comparison of experimental data to models.

Future development is likely to see further enhancements. Once a pattern motif is established and the ability of the Primo device for rapid prototyping is no longer needed, micropatterns can be fabricated using a mask of the motif and parallel illumination. This way, the scanning illumination of the Primo module is avoided which reduces the illumination step from around one hour to a few minutes. The imaging dishes could also

be exchanged with channel slides. Channel slides consist of a number of low volume channels (height of 100 µm) that run across the slide with in- and outlets to each channel. Slides have the advantage of a smaller sample volume, which reduces the cost of consumables like cell culture media and cell treatment solutions. Additionally, slides would offer the possibility to exchange the medium during the measurement. This would significantly extend the capabilities of the migration platform by being able to measure live the response to drug treatments, different flow rates and different viscosities. The time-lapse imaging can be improved by making use of larger camera sensors. The sensor area of newer models with full frame specifications can be almost twice as big compared to the setup presented in this thesis. An increased sensor area directly results in a higher sample throughput and a more efficient workflow.

With an increasing number of experiments the collection of cell trajectories becomes interesting to a rising number of stakeholders from academia, industry and scholarly publishers. The reuse of the data requires a supporting infrastructure. To this end, Wilkinson et al. proposed guidelines in the form of the so-called “FAIR Principles” [229]. The foundational principles – Findability, Accessibility, Interoperability, and Reusability – were chosen to support the reuse of data by individuals but additionally enhance the ability of machines to automatically find and use the data. If the experimental data was made public in adherence with community specific adaptations of the FAIR principles, it would facilitate data-driven discoveries in the cell migration community [230–232].

Intrinsic Cell-to-Cell Variability

Experimental observations of cell trajectories reveal an apparent variability among trajectories in parameters such as velocity and persistence time, see Figs. 3.3 and B.4. This variability arises from a convolution of three factors: the inherent stochasticity of the motion itself (i.e. at the level of an individual), measurement errors, and intrinsic differences between individual cells of the population. Quantifying the variability in migrating cells is challenging and requires an assay that allows to monitor cells under identical conditions over an extended period of time at a certain spatial-temporal resolution. This chapter aims to quantify intrinsic cell-to-cell differences in migrating cells using the aforementioned 1D cell migration assay and the generalised Langevin equation (GLE). The content of this chapter is based on the manuscript “Intrinsic cell-to-cell variance from experimental single-cell motility data” by A. Klimek, J.C.J. Heyn, D. Mondal, S. Schwartz, J.O. Rädler, P. Sharma, S. Block and R.R. Netz to which I contributed in investigation and data curation of cell trajectories [5].

When looking at a randomly chosen sample of trajectories that were obtained from the same cell line and under identical conditions, such as in Fig. 3.3, it becomes quickly apparent that trajectories differ in metrics such as average velocity, acceleration, cell length, and occurrence of directional changes. The fact that there are these phenotypic cell-to-cell differences in the motile behaviour of cells is striking and might even be surprising, considering that the experimental setup with its standardised 1D Fibronectin lanes was designed to minimise noisy external factors that could influence the cell trajectories. However, each experimental assessment, that tries to characterise trajectories, will always exhibit a spread arising from the randomness of the motion, measurement inaccuracies and the variability stemming from differences among the individual single cells. The goal of this study is to determine how much of the parameter spread is caused by cell-to-cell differences.

To analyse the source(s) of the stochasticity one first needs to quantitatively characterise trajectories to then compare the characteristic metrics. To this end, a mathematical model is needed. The most general exact model describing cell motion is the generalised Langevin equation (GLE):

$$\ddot{x}(t) = -\int_{t_0}^{t} \Gamma_v(t-t')\dot{x}(t')\mathrm{d}t' + F_\mathrm{R}(t) \tag{4.1}$$

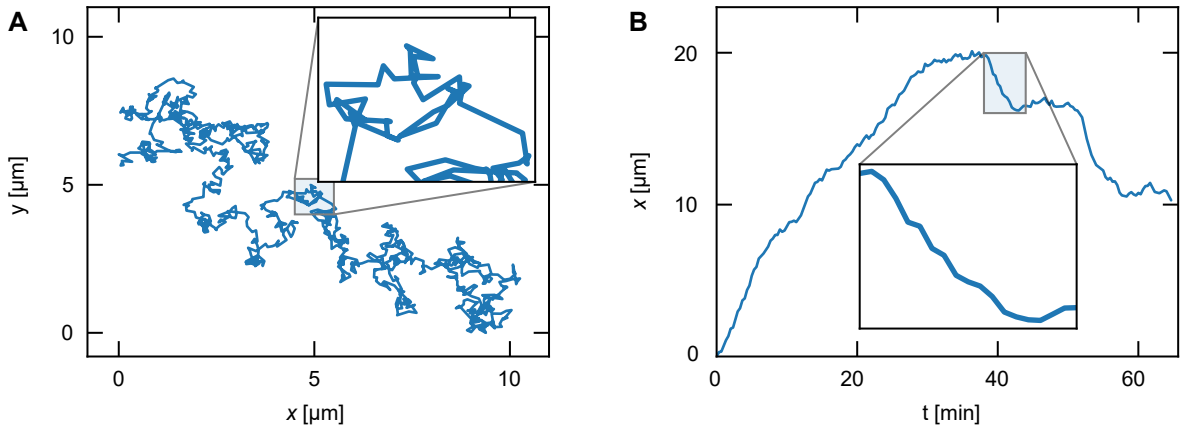

Figure 4.1: Exemplary trajectories of a polystyrene bead with radius $r = 0.5\,\mu\text{m}$ in an aqueous solution **(A)** and of an MDA-MB-231 breast cancer cell in 1D confinement **(B)**. For (A) the trajectory length is $L = 24\,\text{s}$ and for (B) $L = 65\,\text{min}$. The insets show enlarged sections of the trajectories. These zoom-ins, especially for (A), hint at the effect of discrete time steps on the observed trajectory. Adapted from Klimek, Heyn et al. 2024 [5].

Here, $\ddot{x}(t)$ is the acceleration of the position $x(t)$ at time t. $\Gamma_v(t)$ is the memory kernel that characterises how the acceleration at time t depends on the velocity $\dot{x}(t')$ of previous times. $F_\text{R}(t)$ is a random force that represents the stochastic noise of the system. F_R is agnostic to the source of the noise, which means that it captures both the interactions of the cell with its surroundings and intracellular force-generating processes. The GLE is a universally applicable model that captures both passive and active motion.

In the following, we tested our GLE-based analysis first on a well-understood system before moving on to cells. We chose polystyrene beads in an aqueous solution with a known size distribution, a passive system, as control and then breast cancer cells of the type MDA-MB-231 in 1D confinement, an active system, as the actual target. We extracted the respective memory kernels and used them to simulate trajectories with the same time length and temporal resolution as in our experiments. By varying the variance of simulation parameters, we successfully estimated the intrinsic variance of the parameters that characterise the individual objects in the experiments.

1 GLE-Based Analysis of Individual Trajectories

Exemplary trajectories of the polystyrene beads and the cancer cells are shown in Fig. 4.1. We assume that the parameters governing the movement of the beads and the cancer cells are stationary, i.e. do not evolve in time, and that they are Gaussian distributed. The justification of these assumptions is given in the Supplementary Information in the appendix of this thesis. We can then extract their memory kernels $\Gamma(t)$ via the velocity

autocorrelation function (VACF) C_{vv} [233–235]. The VACF is defined as

$$C_{vv}(t) = \langle v(0)v(t)\rangle. \tag{4.2}$$

The VACF C_{vv} is the second derivative of the mean squared displacement (MSD), $C_{vv}(t) = \frac{\mathrm{d}^2}{\mathrm{d}t^2}C_{\mathrm{MSD}}(t)$, with C_{MSD} defined as in Eq. 2.1. The VACF can be connected to the GLE in Eq. 4.1 by averaging over the random force $F_{\mathrm{R}}(t)$ and multiplying both sides with the initial velocity $\dot{x}(t_0)$. The resulting equation can be inverted to extract the memory kernel $\Gamma(t)$ from the VACF. For a detailed description of the scheme, see SI of A. Klimek et al. 2024 [5]. The MSD, however, is usually a more intuitive metric to describe random motile processes as it is a measure of the displacement of a particle over time.

For purely diffusive processes, such as the passive motion of beads in water, we expect the MSD to follow the Brownian prediction, $C_{\mathrm{MSD}}(t) = 2nDt$ Eq. 2.2, for a movement in n dimensions. The motion of the beads in water can be decomposed into orthogonal coordinates because there is no coupling between the components of the motion. This means that each component of the bead's positional vector $\mathbf{x}(t)$ can be analysed separately, i.e. $x(t), y(t)$ This results in a dimensionality of $n = 1$ for each component and a MSD of $C_{\mathrm{MSD}}(t) = 2Dt$ with the diffusion constant D. As the beads are almost perfect spheres of radius r, the viscous friction can be calculated using the Einstein-Stokes relation $D = k_{\mathrm{B}}T/\gamma = k_{\mathrm{B}}T/(6\pi\eta r)$, Eq. 2.3. For the observed length of the trajectories and at the experimental temporal resolution Δ, the MSD's for the trajectories of the polystyrene beads show a linear behaviour in time, i.e. $C_{\mathrm{MSD}}(t) \propto t$, see Fig. 4.2 (A). Moreover, the MSD's are in good agreement with the theoretical prediction of eqs. 2.2 and 2.3 for a sphere with radius $r = 0.5\,\mu\mathrm{m}$, as represented as a green dashed line. The only peak of the VACF of the polystyrene beads in Fig. 4.2 (B) is at time zero, indicating that consecutive displacements are not correlated. This demonstrates that the persistence time of the beads is shorter than the temporal resolution of the experiment Δ. Consequently, the extracted memory kernel $\Gamma(t)$ is a delta function, see Fig. 4.2 (C). These analysis results for the trajectories of the passive beads differ substantially from those of the actively moving cancer cells. The MSD of the cancer cells behaves as $C_{\mathrm{MSD}}(t) \propto t^{1.6}$ which indicates super-diffusive motility, see Fig. 4.2 (D). It is important to note that the majority of the cell trajectories of the experimental data set, which is studied here, are shorter than 100 min, see Fig. B.4 (A). This scarcity of data for long time scales means that the error bars of the mean MSD (not shown) increase for larger t and longer trajectories would be required to thoroughly analyse this time regime, see Fig. 4.2 (D). For long time scales we would expect a transition from the ballistic ($\propto t^2$) to the diffusive regime ($\propto t$) in accordance with the literature [188, 236–238]. The VACF of the cancer cells peaks at time zero, Fig. 4.2 (E). This peak is followed by a pronounced dip at the first time step ($t = \Delta = 20\,\mathrm{s}$), before the VACF falls off to zero within a few minutes, indicating no correlation for longer time shifts. The apparent two regimes of the VACF – first the dip, then the decay – are also visible in the extracted memory kernel in Panel (F), where $\Gamma(t)$ quickly decreases and even becomes negative for small t before rising again to zero where it remains for larger t. The dip is due to localisation noise that counteracts the correlation of consecutive velocities and is therefore not a cell specific property [189, 233].

The differences in the VACF's, MSD's and kernels for the beads and the cancer cells imply that the two systems underlie different modes of motion and, consequently, that the GLEs (Eq. 4.1) will differ. As foreshadowed by the dashed green line in Panel 4.2 (A) already, the polystyrene beads can be considered as a purely diffusive system. This is due to the fact that the persistence time of the beads is shorter than the experimental time resolution Δ, see Panel 4.2 (B). This allows for an over-damped approximation and simplifies the GLE to

$$\dot{x}(t) = \sqrt{D}\xi(t) \tag{4.3}$$

with the uncorrelated white noise $\xi(t)$ ($\langle\xi(t)\rangle = 0$ and $\langle\xi(0)\xi(t)\rangle = 2\delta(t)$). For the cancer cells, the extracted kernel suggests a simple persistent random walk (PRW), which can be formulated as a GLE with the memory kernel

$$\Gamma(t) = 2\delta(t)/\tau_\mathrm{p} \tag{4.4}$$

with $\tau_\mathrm{p} \approx 2\,\mathrm{min}$ as persistence time. For large t the term $\tau_\mathrm{p}(1-e^{-t/\tau_\mathrm{p}})$ in Eq. 2.4 goes to zero, resulting in an effective diffusion with diffusivity $D = V\tau_\mathrm{p}$. The observed super-diffusive behaviour in Fig. 4.2 (D) comes from the transition from the ballistic ($C_\mathrm{MSD}(t) \propto t^2$) to the diffusive regime ($\propto t$). The VACF is given by

$$C_\mathrm{vv}(t) = Ve^{-t/\tau_\mathrm{p}}. \tag{4.5}$$

The analytical models for both the polystyrene beads and the cancer cells were fitted to each trajectory individually – as opposed to the VACF of the mean trajectory. The fitting procedure also takes into account the discretisation and the localisation errors of the experimental data. The parameters that were fitted are the diffusion constant D (Eq. 4.3) and the localisation noise σ_loc for the beads and the mean squared velocity V, the persistence time τ_p (Eq. 4.5) and σ_loc for the cells. The procedure is described in detail in A. Klimek et al. 2024 [5]. Two randomly chosen examples are shown in Fig. 4.3. The fits are in good agreement with the experimental data, which confirms the choice of analytical models.

2 Reproducing Experimental Parameter Distributions by Simulation

Now that the MSD and VACF are established as quantitative metrics to characterise individual trajectories and an analytical model is found for each motile system, we can tackle the main question of this chapter: To what extent does the variability in parameters obtained from experimental data arise due to individual differences compared to the variability resulting from stochastic motion and experimental errors? To answer this, we use simulations of our mathematical model that we compare with the experiment.

If all individual motile objects were identical, then one parameter set would be sufficient to model all observed trajectories. We used the two analytical models given in Eqs. 4.3 and

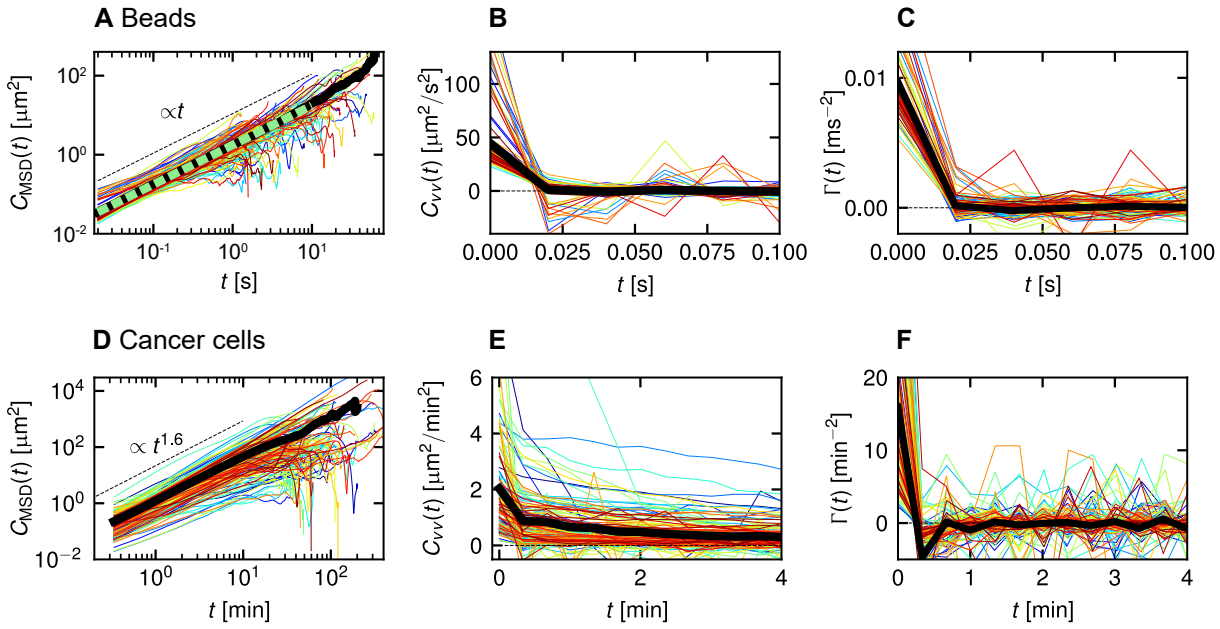

Figure 4.2: Experimentally determined MSD, VACF and memory kernels for beads **(A-C)** and cells **D-F**. Each colour represents the data for a single individual trajectory, while the black lines represent the respective population average. Memory kernels $\Gamma(t)$ were calculated from VACFs. The dashed green line in panel (A) represents the prediction of the Einstein relation Eq. 2.3 for the diffusion of a sphere with radius $r = 0.5\,\mu\text{m}$ in water. The black dashed lines in (A) and (D) represent the scaling behaviour for the MSD. Adapted from Klimek, Heyn et al. 2024 [5].

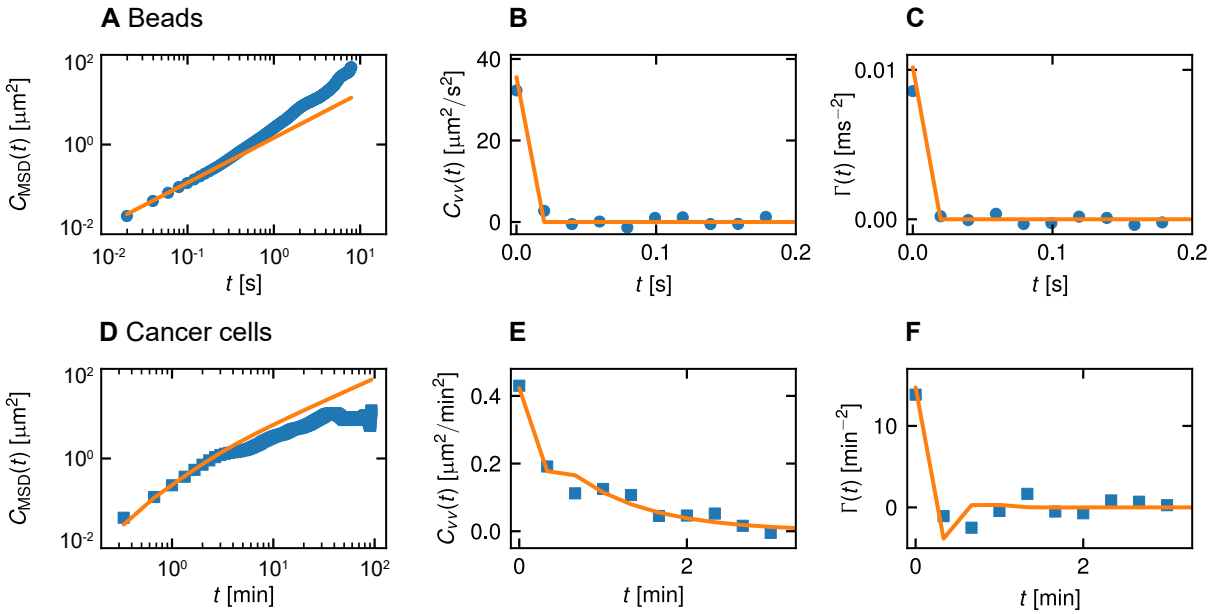

Figure 4.3: The analytical solutions of the generalised Langevin equation, Eq. 4.1, are fitted to each trajectory individually, with pure diffusion for the polystyrene beads, Eq. 4.3, and a persistent random walk for the cancer cells, Eq. 4.4. The fits are shown as orange lines and the experimental data points as blue dots. The exemplary fits shown here were chosen at random from the total ensemble. Adapted from Klimek, Heyn et al. 2024 [5].

2.4 with the same trajectory length distribution as for the experimental data. Stochasticity in the models paired with the finite observation time and the inevitable localisation error, will always lead to some spread in the extracted parameters. This phenomenon can be seen in Fig. 4.4 where the parameters extracted from fitting experimental data are shown in blue and the parameters extracted from simulated data are shown in orange. In Panels 4.4 (B) and (E) orange triangles originate from trajectories that were simulated using a single parameter set, indicated by empty, light green symbols. The parameter sets used as input are the median values of the experimental parameter sets. The spread in the values for the parameters that have been extracted from the simulated data is due solely to the inherent stochasticity of finite-length trajectories and σ_{loc}. The difference between the spread of experimental versus simulated data therefore gives an indication of the individual-to-individual variation. For the polystyrene beads in Panel 4.4 (B) the spreads of the parameters retrieved from experimental and simulated data are almost identical. The experimentally observed spread hence originates largely from the finite length of the measurement and experimental noise, hence indicating a low bead-to-bead variance. The opposite is true for the cancer cells in Panel 4.4 (E) where the variance from simulated data is way smaller than the one found from experimental data. Here, the discrete nature of the data and the localisation error alone can't explain the spread of the experimental data and it is unlikely that cells share the same identical parameter set.

Next, instead of using a single parameter set, we drew parameters from Gaussian

distributions to simulate trajectories from which we then extracted parameters. By varying the variance of the Gaussian input distribution and comparing the covariance to that of the parameter distribution extracted from the experiment, we arrived at the optimal input spread to explain the observed distributions, see Fig. 4.4 (C) and (F). For a detailed description of the optimisation scheme, see A. Klimek et al. 2024 [5]. While the spread of the experimental parameters for the beads was small and mostly due to the finite length of the measurement, we find that the beads were actually not identical. We retrieved a standard deviation of the bead radius $\Delta r = 86 \pm 63\,\mathrm{nm}$ which is in agreement with the standard deviation of $\Delta r \approx 25\,\mathrm{nm}$ listed by the manufacturer. For cells, we obtained a spread spanning nearly two orders of magnitude in both the mean squared cell speed V ($\approx 10^{-1} - 10^{1}\mu\mathrm{m}^2/\mathrm{min}^2$) and the persistence time τ_p ($\approx 10^{-1} - 10^{1}\mathrm{min}$). This large spread is despite the genomic identity and the controlled experimental environment.

3 Discussion

The approach presented here, using the generalised Langevin equation (GLE) and simulating data with parameters from Gaussian distributions, can distinguish cell-to-cell variance from motion stochasticity in experimentally obtained data. This method correctly predicted the standard deviation of the radius of the polystyrene beads solely on the basis of the trajectories of individual beads. The prediction was in good agreement with the actual standard deviation of the beads radii as given by the manufacturer and experimentally verified by atomic force microscopy (AFM). For cancer cells, the predicted parameter spread is much larger than for polystyrene beads, which is in itself not surprising. Upon visual inspection, one can already tell that the trajectories of the passively diffusing beads are more similar to each other than the trajectories of the actively migrating cells. The predicted spread of two orders of magnitude for the cells, however, is fascinating. All cells are from the same cell line and therefore carry identical genomes. Although mutation rates can be higher in cancer cells, it is unlikely that these can explain the large cell-to-cell variance observed in this study [239, 240]. An analysis of the trajectories of healthy cells should easily clarify this point. However, there might be a non-negligible *epigenomic* variance between cells that results in differences in chromatin accessibility or promoter architectures and, as a consequence, in gene expression levels [241, 242]. This is particularly likely since the recorded trajectory lengths are much shorter than the doubling time of MDA-MB-231 cells ($\approx 2\,\mathrm{h}$ vs $\approx 25\,\mathrm{h}$, respectively [243, 244]). As a consequence, each trajectory provides only a snapshot of the cell's dynamics during its cell cycle and different trajectories are likely to be measured in different stages of the cycle, leading to different gene expression levels [245]. Additionally, local changes in the environment of cells such as inhomogeneities in the Fibronectin density affect the cell's motile behaviour [1]. Although the fibronectin lanes were designed to be of constant protein density and homogeneous throughout, they inevitably contain some impurities and local imperfections. This is especially true since the micropatterns used for this study were fabricated according to the microcontact printing protocol, see Microfabrication of

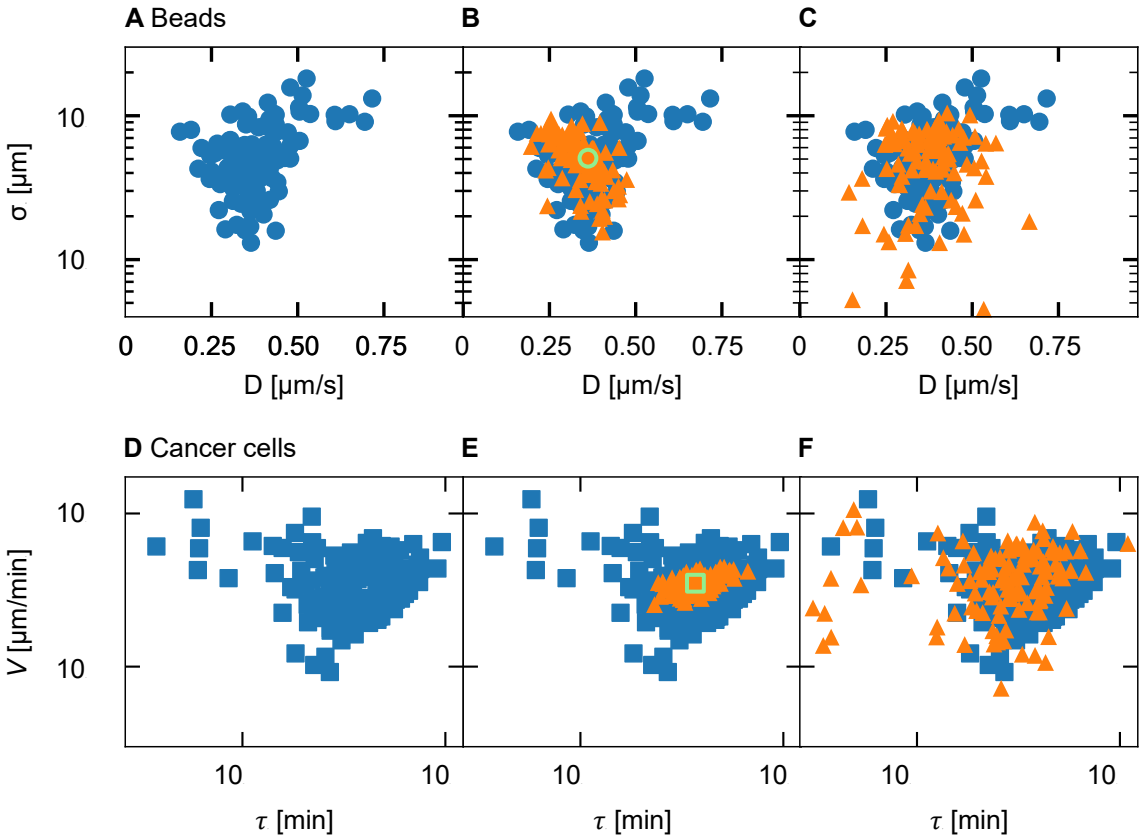

Figure 4.4: Distribution of model parameters for polystyrene beads **(A-C)** and cancer cells **(D-F)**. Localisation error σ_{loc} and diffusion constant D are shown for the beads, mean squared velocity V and persistence time τ_{p} for the cells. The parameter values that were extracted from the individual experimental trajectories are shown in blue. Parameters extracted from simulated trajectories are shown in orange. Simulations for **(B)** and **(E)** only used a single parameter set as input, i.e. the median experimental values represented as empty green triangles. Hence, the spread of the extracted parameters of the simulated trajectories in (B) and (E) is only due to time discretisation and localisation errors. Trajectories for **(C)** and **(F)** were simulated by drawing input parameters from a Gaussian distribution with the goal to achieve the same variance as for the experimental data. The spread of the extracted parameters, again taking into account time discretisation and localisation errors, is – per construction – identical to that of the experimental distribution. Adapted from Klimek, Heyn et al. 2024 [5].

1D Migration Platforms. Photopatterned substrates might lead to less external noise. To further elucidate the effect of Fibronectin inhomogeneities it might be worthwhile to compare the auto-correlation of the Fibronectin signal along the lane to that of the cells. Future studies should also increase both the length of single cell trajectories and the temporal resolution. As could be shown in Fig. 4.4 (B&E), finite and discrete measurement intervals alone already lead to a significant spread in the extracted parameter distribution. While the persistent random walk (PRW) fits the experimental data very well, its choice as the analytical solution of the GLE is based mainly on the analysis of the velocity autocorrelation function (VACF) $C_{\mathrm{VV}}(t)$ for $0\,\mathrm{min} < t < 1\,\mathrm{min}$ which comprises only 3 sampling intervals $\Delta = 20\,\mathrm{s}$. A higher sampling rate would strengthen the claim, that the cell trajectories can be described by a PRW.

While the generalised Langevin equation is the most general description of single cell motility, it offers little insight into the cell-mechanical dynamics underlying cell locomotion. To understand the connection between cytoskeletal processes and cell motility a biomechanical model is needed.

Biophysical Modelling of Cell Migration

The variability and randomness of cell motility were the focus of the last chapter. This chapter is about the general mechanisms underlying motile behaviour. Several observations on cell motility have been made for a variety of cell lines and are therefore considered universal: cells exhibit a maximum velocity for intermediate adhesion strengths [173]; there is a universal coupling between cell speed and cell persistence (UCSP) [142]; and the morphodynamics of cells can be classified into different coexisting motile states.

In this chapter, I propose and discuss a novel biophysical model that relates the observed phenomena to the cytoskeletal dynamics and interactions of the cell with its environment. The mathematical model is a result of the collaboration with the group of Martin Falcke. It is based on the force balance at the leading edge of the cell, the noisy clutch of retrograde flow, and friction and drag which depend on integrin signalling. One-dimensional fibronectin (FN) lanes provide the experimental control necessary to quantitatively study cell motility and test the biophysical model. The content of this chapter is based on the two journal articles “On the adhesion-velocity relation and length adaptation of motile cells on stepped fibronectin lanes” by C. Schreiber, B. Amiri, J.C.J. Heyn, J.O. Rädler and M. Falcke, to which I contributed in investigation (mainly visualisation of adhesion sites), and “On multistability and constitutive relations of cell motion on fibronectin lanes” by B. Amiri, J.C.J. Heyn, J.O. Rädler and M. Falcke, to which I contributed in investigation, data curation, visualisation and writing [1, 2].

1 Adhesion-Velocity Relation

For this study, we restricted cell motion again to 1D lanes coated with fibronectin (FN) and passivated with PLL PEG everywhere else. With the lanes being 15 µm wide, the cell morphology remained largely comparable to their two-dimensional shape, but major protrusions were restricted to the direction of the lane. The confinement had several advantages. It made it possible to expose cells to a well-defined homogeneous density of ligands that could be measured using the intensity of the fluorescent FN label, see Materials and Methods. The surface density of FN, B, was varied from 1 ng cm^{-2} up to 200 ng cm^{-2}. Furthermore, cells could be exposed to perturbations caused by local changes in FN density using a two-stamp version of the microcontact printing protocol,

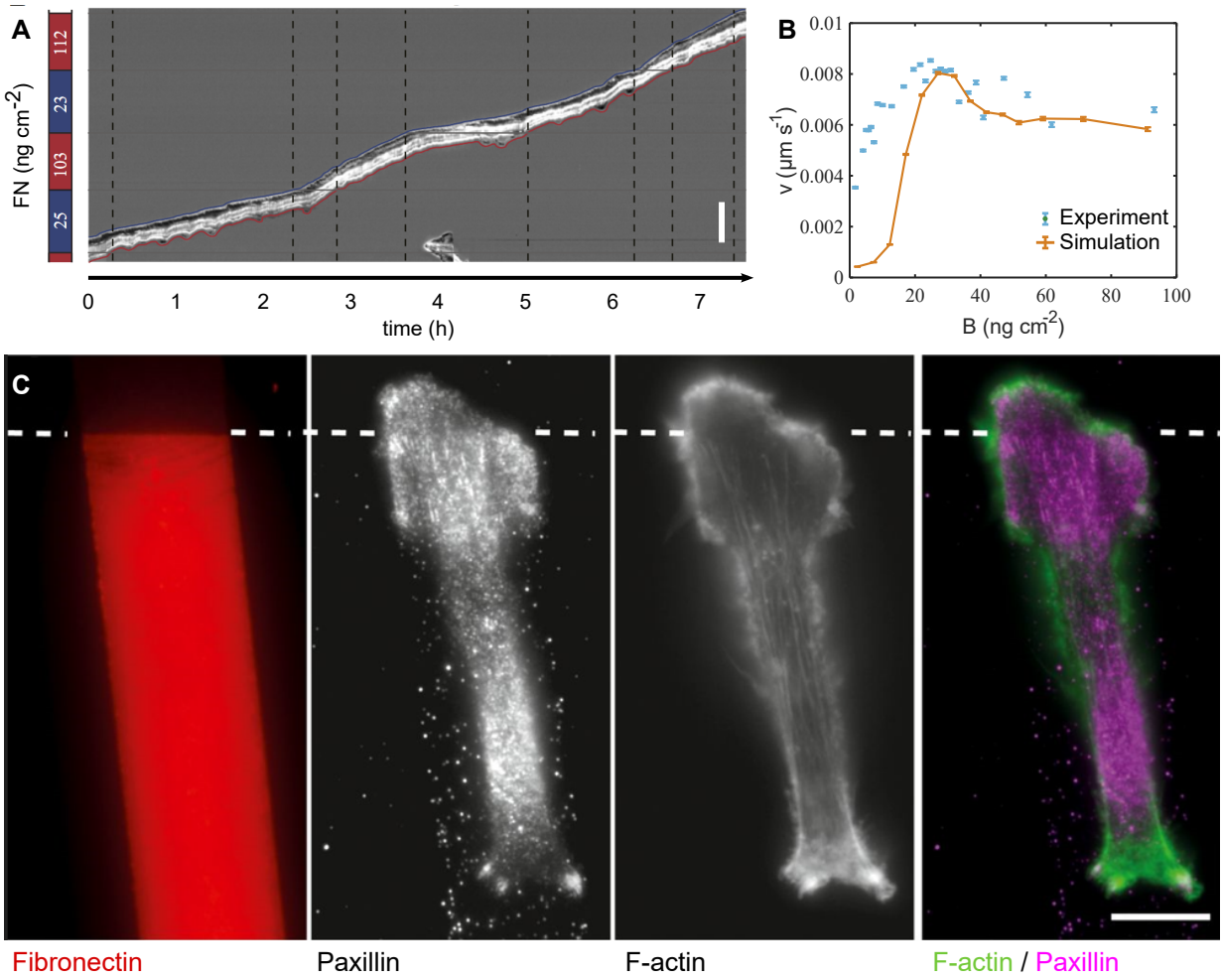

Figure 5.1: Mesenchymal cells migrate fastest for intermediate adhesion strengths. **(A)** The kymograph displays a single cell that migrates along a 1D fibronectin (FN) lane. The FN density varies between strips of constant density, as indicated on the left side. The slope of the cell in the kymograph, that is the cell velocity, changes noticeably between stripes of different FN densities. **(B)** Quantification of the biphasic adhesion-velocity relation for $N = 6261$ trajectories of single MDA-MB-231 cells (blue dots). Error bars represent the standard error of the mean. **(C)** Fixed MDA-MB-231 cell on a FN step (moving upwards from 8 ng cm^{-2} to 40 ng cm^{-2}). The position of the step is indicated by the white dotted line. Images of labelled FN and phalloidin-stained f-actin were acquired with epifluorescence, and antibody-stained paxillin with total internal reflection (TIRF). The density of the focal adhesion protein paxillin correlates with the FN density and the location of the adhesion sites coincides with the ends, or anchor points, of the actin stress fibres. Scale bar 10 µm. (A,C) adapted from C. Schreiber et al. 2021 [1], (B) adapted from B. Amiri, J. Heyn et al. 2023 [2].

see Microcontact Printing. Additionally, this setup simplified the analysis of cell trajectories and the formulation of a biophysical model by confining the movement to 1D.

An example of a single MDA-MB-231 cell on a 1D lane is shown in Figure 5.1, Panel A. The cell moves along the lane, crossing fields of varying FN density B, as indicated by the red and blue rectangles on the left side. The kymograph reveals the trajectory of the cell in a single image as a projection to the time axis. Changes in the slope of the cells position over time, i.e. the cell velocity, are apparent at every change of FN density.

I observed the migration of MDA-MB-231 cells on FN coated lanes over a period of 48 h using scanning time-lapse microscopy. As detailed in Materials and Methods, a series of fields of view were imaged sequentially at intervals of either 10 min or 30 s, collecting data from 144 to 16 fields of view per round, respectively, averaging 23 trajectories of individual cells per field. The mean duration of a single-cell trajectory was 11.6 ± 8.0 h, with longer trajectories becoming increasingly rare due to cell division, cell-cell interaction and movement out of the field of view (Table B.1 and Fig. B.5). For the data in this section, I tracked the position of the fluorescently labelled nuclei of N = 6261 MDA-MB-231 H2B mCherry cells with a time resolution of Δ =10 min. Next, I calculated the instantaneous velocity $v = \frac{x_{i+1}-x_i}{\Delta}$ and plotted the velocities against the FN density B. The result is shown in Figure 5.1, Panel B. The instantaneous velocity, averaged over all cell trajectories, increases with increasing FN density up to a maximum of $v = 0.0084\,\mu m\,s^{-1}$ at $B = 24\,ng\,cm^{-2}$. Velocities for FN densities higher than that decrease again before slowly plateauing at ca $v = 0.0065\,\mu m\,s^{-1}$. Our observation of the biphasic dependency of the velocity on the ligand density is in good agreement with reports on similar cell lines, as discussed in Fundamental Concepts [80, 81, 83, 84, 173, 175–177]. Mesenchymal cells exert forces on their environment via focal adhesions (FA) sites [246]. The FAs anchor the cell to the substrate, often with the support of bundles of actin, also called stress fibres, thereby causing friction between the retrograde flow of the actin network and their stationary structures. To see if the density of adhesion structures correlates with ligand density, I stained fixed cells for paxillin, an FA protein, and for f-actin using phalloidin, see Materials and Methods. The MDA-MB-231 cell depicted in Fig. 5.1 (C) crosses from an area of high FN density (40 ng cm^{-2}) to an area of low FN density (8 ng cm^{-2}). The cell exhibits a high density of adhesion sites just a few micrometres back from the leading edge, where stress fibres are also anchored (as seen in the f-actin image). The concentration of f-actin is highest within the lamellipodium. However, the distribution of paxillin depends not only on the relative position within the cell but also on the FN density, with a higher density of paxillin in the region of high FN density.

In summary, cell velocity increases with ligand density up to a peak, after which it decreases and plateaus. This biphasic velocity response is likely to be related to the density of adhesion structures. Any biophysical model that aims to describe and explain cell motility should cover this biphasic adhesion-velocity relation. There are, however, further phenomena that should also be included.

2 Motile States

In addition to the 6 000 single cell trajectories of the last section, we analysed more than 14 000 trajectories with 10 min resolution and 400 trajectories with 30 s resolution (Table B.1). This large amount of data made it possible to identify four distinct motile states, see Fig. 5.2. We observed cells that were in a non-moving spread state and cells that were in a moving state. Independent of that, cells kept a steady length or showed oscillations in the length(s) of their protrusion(s). By combining the two metrics (spread vs moving and oscillating vs steady length), we arrived at the four motile states depicted as kymographs in Fig. 5.2 (B-E) and as segmented trajectories in Fig. 5.3. The state of a spread cell with a steady cell length we call SS, a spread cell with oscillating length we refer to as SO, cells that are moving with a steady length are assigned the state MS and cells that are moving with oscillating length are MO. Hennig et al. have also presented the states SS and MO with RPE1 cells and NIH-3T3 fibroblasts [138]. The two moving states, MS and MO, manifest as movements in upward and downward directions, MS↑, MS↓, MO↑, and MO↓, resulting in a total of six states observable.

A selection of six distinct state transitions are shown in Fig. 5.2 (F-K). Each transition shown occurs on uniform lanes of homogeneous FN density without external influence. Consequently, we refer to these as spontaneous transitions. Such a transition can also be a change in direction, as in Panel (F), where the cell first moves downward (MS↓) and then upward (MS↑).

To quantitatively analyse the motile states and transitions between them, the states needed to be defined by a mathematical metric and thresholds, see Materials and Methods. This allowed to automatically assign a motile state to each point in time for each segmented cell trajectory, see Fig. 5.3. For a complete list of all possible state transitions in MDA-MB-231 cells, see Fig. B.6.

The oscillatory behaviour observed in SO and MO often lacks consistent periodicity, Fig. 3.3. This variability in repetitive protrusion events suggests a noisy excitable state rather than the strictly defined regular oscillations of dynamical systems theory. In the following section, it will become evident that our biophysical model encompasses regular oscillations, noisy oscillations, and a noisy excitable regime.

Spread cells demonstrate a symmetrical appearance, with extensions emerging from both ends, Fig. 5.2 (B,C). Cells in motion naturally show extensions at the leading edge, e.g. Fig. 5.2 (D-J). Yet, additional rear extensions can be identified by detecting negative rear edge velocities during oscillatory phases, as illustrated in Fig. 5.2 (E,J). Consequently, oscillatory cells in motion have extensions at both the front and the rear. Fig. 5.2 (F) does not allow us to determine whether there is a rear extension in a cell in the MS state during continuous movement. Should rear extensions be present under these conditions, they are presumably shorter than those at the front. Notably, the formation or elongation of a rear extension precedes a change in direction in Fig. 5.2 (F) by approximately 30 min. Therefore, extensions are present at both the front and rear during the transition. This observation leads to the hypothesis that direction reversals may result from competition

of the front and rear protrusion, as will be discussed later.

3 Biophysical Model

The biophysical model is motivated by the aforementioned universal observations and consists of well-established force balances at the leading and trailing edge of the cell and for the cell body, see Fig. 5.4 [124, 178–180, 190, 247–249]. The force of the polymerisation of the actin network at the front of the cell F_f pushes the membrane outward against an elastic force $F_{\text{spring}} = E(L_f - L_0)$, that depends linearly on the difference of the actual protrusion length L_f and the resting protrusion length L_0, and against drag $F_{\text{drag}} = \zeta_f v_f$, that depends linearly on the velocity of the protrusion v_f and the drag coefficient ζ:

$$F_f - F_{\text{spring}} - F_{\text{drag}} = 0 \tag{5.1}$$

The polymerisation force F_f at the front of the cell arises from actin filaments pushing against the membrane (see “Brownian ratchet”) and drives a retrograde flow of actin filaments v_{r_f} against friction [180]: $F_f = \kappa_f v_{r_f}$ with the friction coefficient κ. For an illustration see Fig. 5.4 (A), insets I and II. The elastic force F_{spring} couples the leading edge with the cell body, approximated by the centre of the nucleus, through the membrane tension, which most likely originates from one-dimensional (1D) volume homeostasis [250]. The cell experiences drag F_{drag} mainly due to adhesions that bond the cell to the substrate (Fig. 5.4 (A), inset III). The observation of the existence of rear protrusions even for polarised cells mentioned above motivated us to model the 1D migration of mesenchymal cells by defining the force balance at three points: the front (denoted by the subscript $_f$), the centre ($_c$) and the back ($_b$) of the cell. Thus, the model is defined by the following system of equations:

$$\kappa_{\text{f}} v_{\text{r}_{\text{f}}} - E(L_{\text{f}} - L_0) - \zeta_{\text{f}} v_{\text{f}} = 0 \tag{5.2}$$

$$E(L_{\text{f}} - L_0) - E(L_{\text{b}} - L_0) - \zeta_{\text{c}} v_{\text{c}} = 0 \tag{5.3}$$

$$-\kappa_{\text{b}} v_{\text{r}_{\text{b}}} + E(L_{\text{b}} - L_0) - \zeta_{\text{b}} v_{\text{b}} = 0 \tag{5.4}$$

The inclusion of the cell body and the back protrusion is an extension to the model presented in Schreiber et al. 2021 [1]. Front and back protrusions, as well as drag, act on the cell body, Eq. 5.3. The extension was necessary to account for the morphodynamics of the cell, e.g. oscillations of protrusion length. Another modification of the model compared to Schreiber et al. 2021 [1] is the addition of a noisy clutch.

Various studies [193, 251–255] report the noisy clutch phenomenon from the retrograde flow of f-actin within protrusions [256]. This movement creates friction with structures like stress fibres and adhesion sites [246, 257], enabling protrusion force transmission to the substrate. The friction coefficient κ indicates clutch engagement, with higher values showing engagement and lower values showing disengagement. Initially, friction force increases with slow retrograde flow velocity, then decreases past a critical velocity

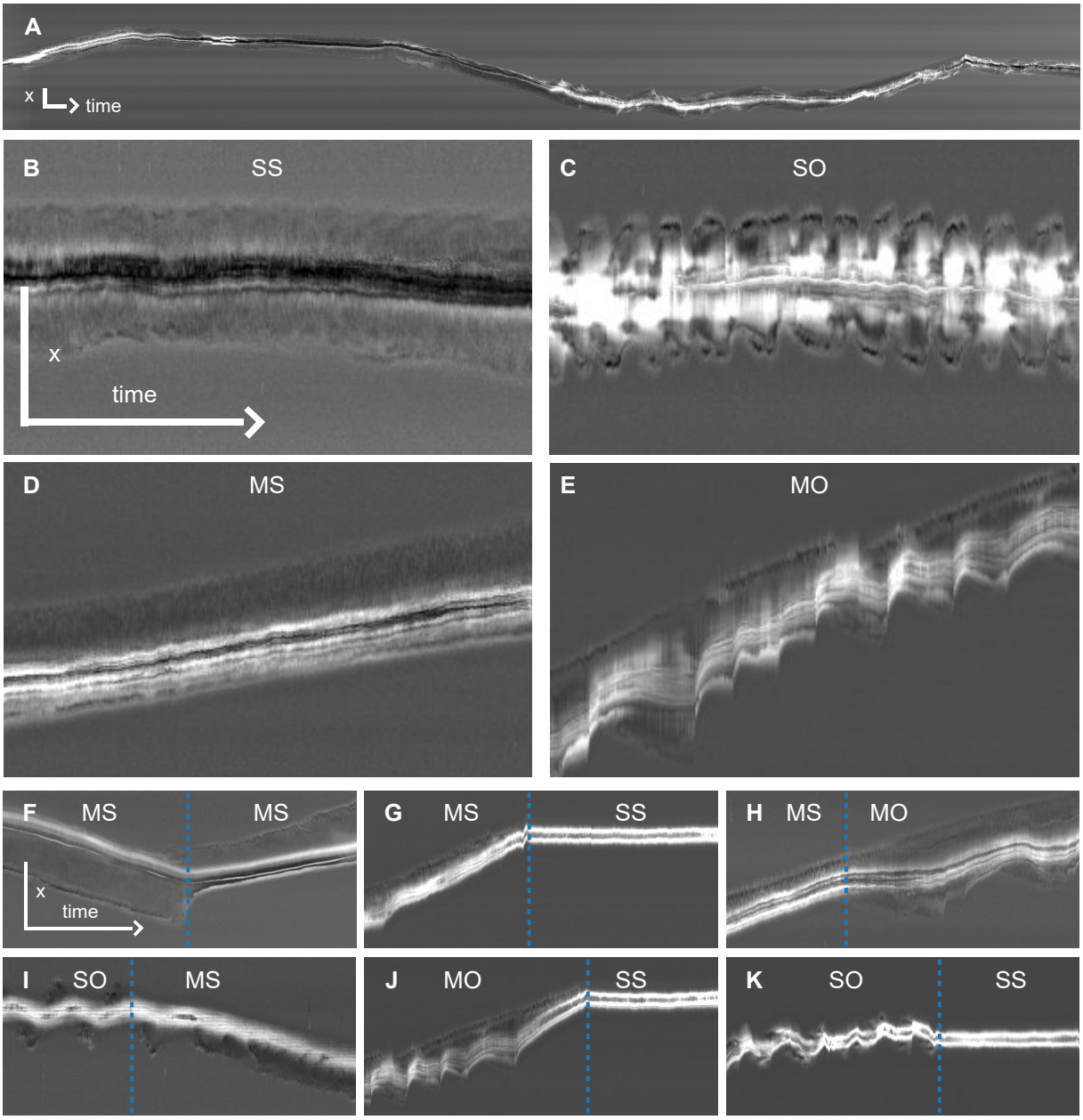

Figure 5.2: Four motile states, as well as transitions between them, can be observed for MDA-MB-231 cells on FN lanes. **(A)** Kymograph of a typical 48 h trajectory. **(B)** Spread cell with steady length (SS). **(C)** Spread cell with oscillating length (SO). **(D)** Moving cell with steady length (MS). **(E)** Moving cell with oscillating length (MO). **(F)** Transition from downward to upward-moving MS state. **(G–K)** Transitions: MS-SS (G), MS-MO (H), SO-MS (I), MO-SS (J), SO-SS (K). Vertical blue lines show state transition points from the change point algorithm defined in Materials and Methods. Kymographs have a 30 s time resolution. Time moves left to right. Vertical scale: 100 µm, horizontal scale: 60 min. Scale in (B) applies to (B–E); scale in (F) applies to (F–K). Adapted from Amiri, Heyn et al. 2023 [2].

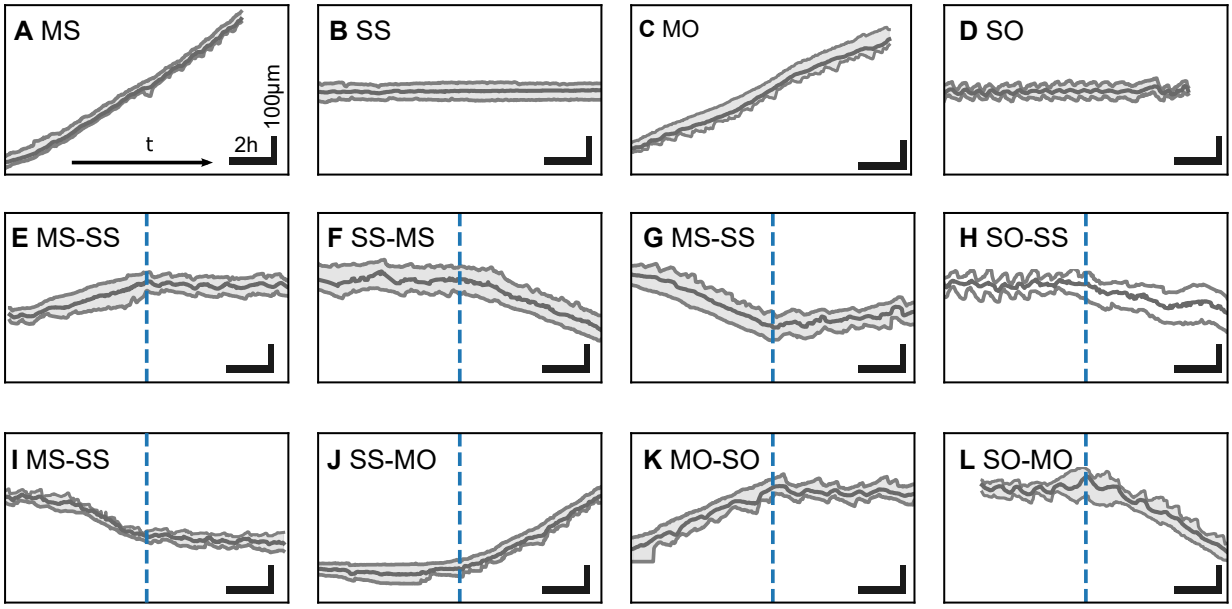

Figure 5.3: Automation enables high-throughput analysis of state transitions. Cells are automatically segmented and tracked. The resulting trajectories are cut into phases of pure motile states, such as in Panels **(A-D)**, and are labelled accordingly. **(E-L)** This process makes it easy to study transitions between motile states, such as the ones depicted here. For a complete list of all possible state transitions in MDA-MB-231 cells, see Fig. B.6. Adapted from Heyn et al. 2024 [4].

(Fig. 5.4 (A) and (C), Panels II, respectively), leading to stick-slip transitions where reduced resistance and constant driving force cause sudden acceleration. Friction force links to transient bonds between the f-actin network and immobile structures. Its biphasic behaviour arises when these bonds dissociate at high velocities, causing clutch disengagement [258]. Rebinding restores equilibrium density after high-speed phases, which motivates the κ-dynamics adapted from Craig et al. (2015) [193]:

$$\frac{\mathrm{d}\kappa_\mathrm{f}}{\mathrm{d}t} = k_\mathrm{on}(\kappa_f^\mathrm{lim} - \kappa_\mathrm{f}) - k_\mathrm{off} e^{-\frac{v_\mathrm{rf}}{v_\mathrm{slip}}} \kappa_\mathrm{f} + \eta_f(t) \tag{5.5}$$

$$\frac{\mathrm{d}\kappa_\mathrm{b}}{\mathrm{d}t} = k_\mathrm{on}(\kappa_b^\mathrm{lim} - \kappa_\mathrm{b}) - k_\mathrm{off} e^{-\frac{v_\mathrm{rb}}{v_\mathrm{slip}}} \kappa_\mathrm{b} + \eta_b(t) \tag{5.6}$$

with the binding rate k_on and the unbinding rate k_off and an exponential acceleration of bond dissociation by retrograde flow velocity v_r [258]. κ^lim represents the maximum value of κ, defined by the adhesion strength of the substrate. The variables η_f and η_b with $\langle \eta_{f,b}(t) \rangle = 0$ introduce Gaussian white noise, caused by the stochastic process of bond creation and cleavage within the f-actin network and its interaction with stationary structures. Note that I renamed c_1 as k_on, c_2 as k_off and c_3 to v_slip for clarity compared to Amiri et al. (2023) [2]. Schreiber et al. (2023) showed that Hill-type equations of the relation of friction coefficients κ and drag coefficients ζ with the Fibronectin density B

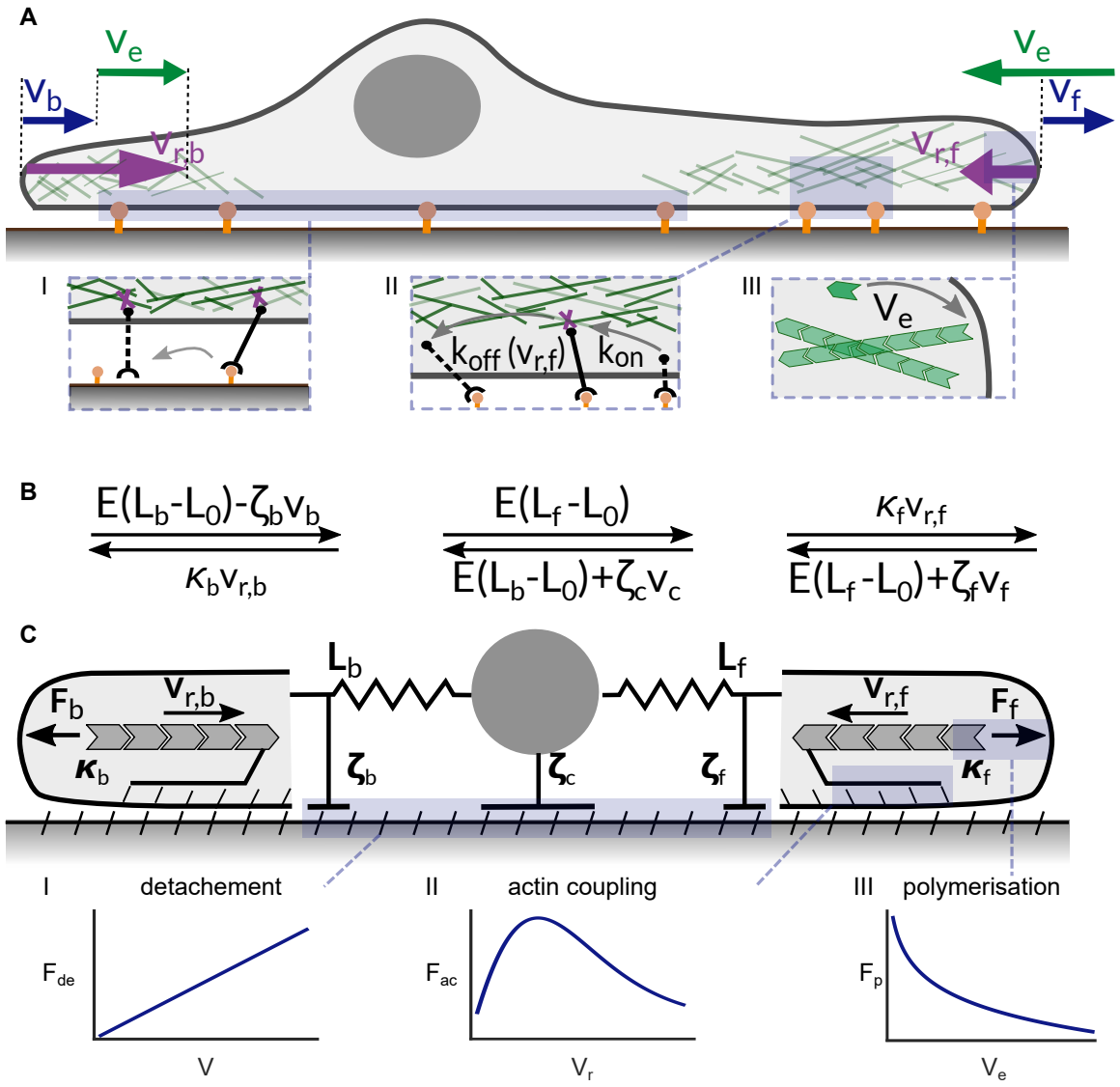

Figure 5.4: Cartoon of a mesenchymal cell on a one-dimensional fibronectin lane **(A)**, the force balances **(B)**, and the model's mechanical elements **(C)**. The velocities of the leading and trailing protrusion edges are v_f and v_b, respectively. The flow of f-actin networks occurs at retrograde flow rates v_{r_f} and v_{r_b}. Forces $F_b = \kappa_b v_{r_b}$ and $F_f = \kappa_f v_{r_f}$ result from f-actin polymerisation, influencing the protrusion edge membrane and facilitating retrograde flow against frictional forces. Drag experienced by the front and back edge membranes has coefficients ζ_f and ζ_b, accordingly. Elastic forces $E(L_f - L_0)$ and $E(L_b - L_0)$ are exerted between the cell body and the edges, with L_0 as the equilibrium length. The balance of elastic forces influences the movement of the cell body against the drag force $\zeta_c v_c$. The lower panels display key relational types of the model. The detachment force F_{de} at the rear is directly proportional to the velocity. The frictional force between the retrograde flow of the f-actin network v_r and static structures shows a peak in its relationship with retrograde flow (clutch). The polymerisation force F_p is logarithmically tied to the network extension rate v_e, influenced by the force-dependent polymerisation rate. Adapted from Amiri, Heyn et al. 2023 [2].

quantitatively describe the adhesion-velocity relation [1]:

$$\kappa_f^{\lim} = \kappa_0 + \frac{\kappa^{\max} B_f^{n_\kappa}}{K_\kappa^{n_\kappa} + B_f^{n_\kappa}} \tag{5.7}$$

$$\kappa_b^{\lim} = \kappa_0 + \frac{\kappa^{\max} B_b^{n_\kappa}}{K_\kappa^{n_\kappa} + B_b^{n_\kappa}} \tag{5.8}$$

and

$$\zeta_f = \zeta_0 + \frac{\zeta^{\max} B_f^{n_\zeta}}{K_\zeta^{n_\zeta} + B_f^{n_\zeta}} \tag{5.9}$$

$$\zeta_c = \zeta_0 + b\left(\frac{\zeta^{\max} B_c^{n_\zeta}}{K_\zeta^{n_\zeta} + B_c^{n_\zeta}}\right) \tag{5.10}$$

$$\zeta_b = \zeta_0 + \frac{\zeta^{\max} B_b^{n_\zeta}}{K_\zeta^{n_\zeta} + B_b^{n_\zeta}} \tag{5.11}$$

$$\tag{5.12}$$

The base values for the drag coefficient and the friction coefficient are denoted as κ_0 and ζ_0, respectively. The Hill coefficients are n_κ and n_ζ, respectively, and K^n is the ligand concentration that produces half the occupation. The variable b quantifies the influence of the cell body on the overall drag exerted by the cell, relative to that of the protrusion. It is important to note that the equations for the front and back of the cell are symmetric.

To relate the velocity of the actin retrograde flow from the laboratory reference system to that of the cell, a Galilean transformation can be used to arrive at the extension rate of the actin network v_e. The extension rate of the actin network is the vectorial sum of the retrograde actin flow $v_{\mathrm{r_f}}$ and the cell velocity v: $v_{r_f} + v_f = v_{\mathrm{e}}$. The network extension rate is set by the polymerisation rate of g-actin to f-actin, which is force dependent. This motivates to model v_e with an Arrhenius factor [257, 259]:

$$v_{\mathrm{r_f}} + v_{\mathrm{f}} = V_{\mathrm{e}}^0 \exp\left(\frac{-aF_{\mathrm{f}}}{N}\right) - k^- \tag{5.13}$$

$$v_{\mathrm{r_b}} - v_{\mathrm{b}} = V_{\mathrm{e}}^0 \exp\left(\frac{-aF_{\mathrm{b}}}{N}\right) - k^- \tag{5.14}$$

with the base actin network extension rate V_{e}^0. The coefficient $a = gd/k_bT$ incorporates a geometrical component g that results from averaging the orientation of the filaments within the network, the increase in length d=2.7 nm contributed by each actin monomer to the filament, and the thermal energy k_bT. The variable N denotes the number of filaments per unit edge contour length, while k^- represents the rate of depolymerisation. We used a value of N=248 µm^{-1} for all simulations, consistent with the work of Schreiber et al. [1]. This particular value leads to a/N=1 µm/nN.

Changes in the protrusion length L arise from the difference of the velocities of cell edge and nucleus:

$$\frac{\mathrm{d}L_\mathrm{f}}{\mathrm{d}t} = v_\mathrm{f} - v_\mathrm{c} \tag{5.15}$$

$$\frac{\mathrm{d}L_\mathrm{b}}{\mathrm{d}t} = -v_\mathrm{b} + v_\mathrm{c} \tag{5.16}$$

Using the length dynamics of Eqs. 5.15 and 5.16 the velocity of the cell body is given by Eq. 5.3

$$v_c = \frac{E(L_f - L_b)}{\zeta_c}. \tag{5.17}$$

Eqs. 5.5, 5.6, 5.15, 5.16 establish a fourth-order dynamical system that defines cell motility. The values used for simulations are collected in Tab. B.2. Our findings reveal that this model is capable of representing four distinct cellular states.

4 Analysis of Dynamic Cell States

Our biophysical model provides a framework for the characterisation and qualitative as well as quantitative analysis of the morphodynamics of MDA-MB-231 cells. We simulated approximately 6,100 cell tracks and compared the simulated data to the experimental data. A summary of the simulation process and the simulated data can be found in the Supplementary Information. Simulations using the control parameter value set 1, see Tab. B.2, reproduce the biphasic adhesion-velocity relation with maximal cell velocity at intermediate FN densities with good agreement with the experimental results, see Fig. 5.1 (B). Both the experimental and the simulated velocities saturate for large fibronectin densities. However, unlike the asymmetric model in Schreiber et al. 2021 [1], consisting of only one protrusion, the model presented here, consisting of two symmetrically constructed protrusions, does not perfectly fit the velocities for low FN densities. The present model predicts only spread states (SS and SO) for low FN densities, i.e. cells that are not moving, which obviously decreases the average velocity. This is in contrast to the observed results. A likely explanation is that the model presented here is symmetric with two protrusions, unlike Schreiber et al. 2021, which included only one. This asymmetry in the previous model might more accurately represent cell polarisation at low FN densities.

We applied the same state classification, see Materials and Methods, to both the experimental and simulated data. The result shows a good qualitative agreement, as evidenced in Fig. 5.5 (A). The model successfully reproduces all four dynamic cell states, with oscillations observed on both sides for the SO state and only at the back for the MO state. Furthermore, the model quantitatively captures cell velocity, oscillation period, and amplitude, see Fig. 5.5 (B,C). Additionally, the model is capable of making predictions about κ-dynamics and the forces on the edge membrane that extend beyond the scope of experimentally feasible measurements within this study. The retrograde flow velocity

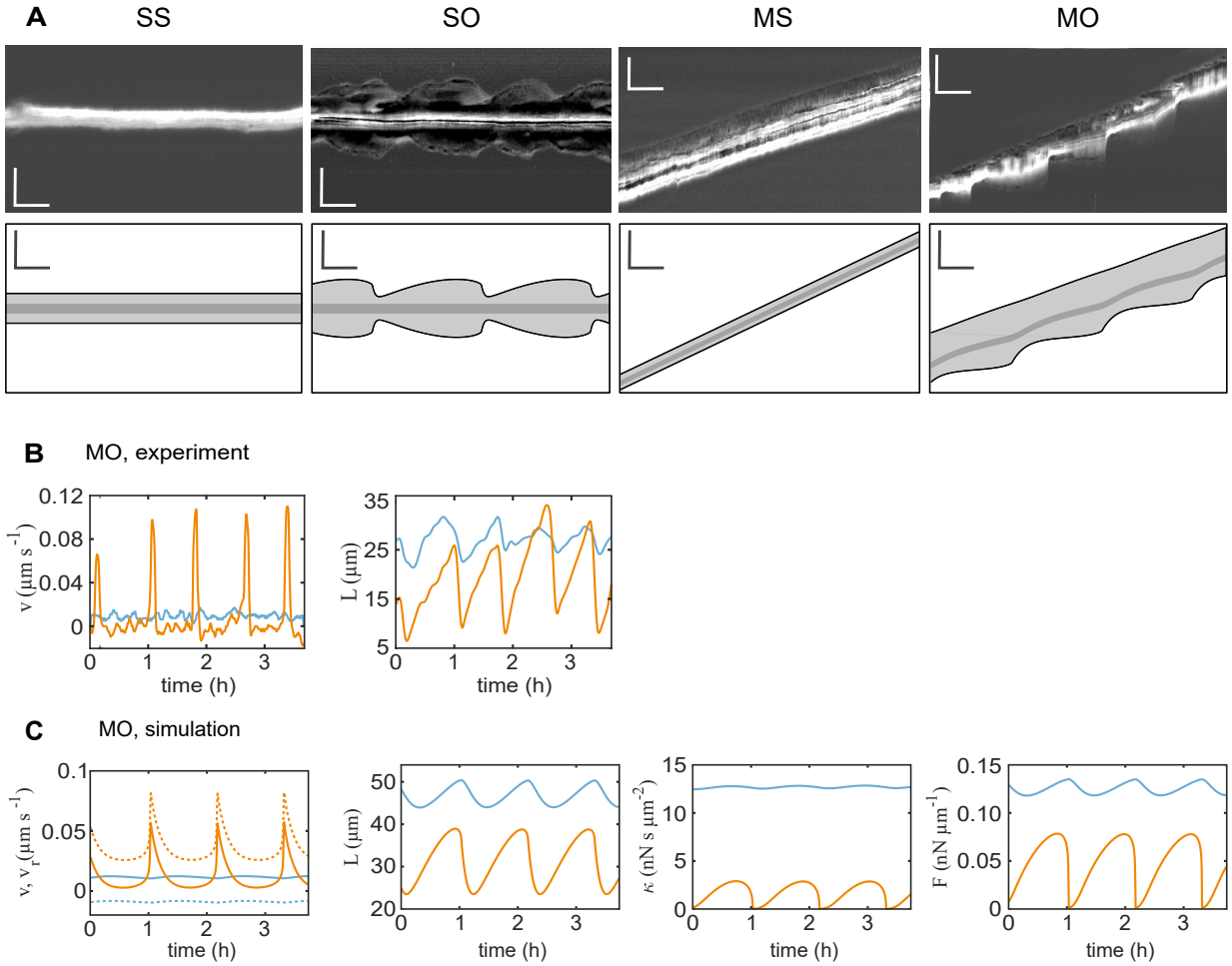

Figure 5.5: Analysis of dynamic cell states. **(A)** The upper panels show experimental kymographs, lower panels depict simulations (without noise). Horizontal scale bars equal 30 min, vertical scale bars 50 µm. Parameters for simulations are listed in Tab. B.2. **(B)** The experimentally determined temporal progression of both the edge velocity and the length of a cell in the MO state is depicted with a blue front and orange back. **(C)** A simulation (without noise) illustrates the temporal progression of parameters including edge velocity v (solid line), retrograde flow v_r (dashed line), cell length L, friction coefficient κ, and force exerted on the edge membrane F in the MO state with a blue front and orange back. The biophysical model qualitatively and quantitatively (velocity, oscillation amplitude and periodicity) captures the observed morphodynamics. Adapted from Amiri, Heyn et al. 2023 [2].

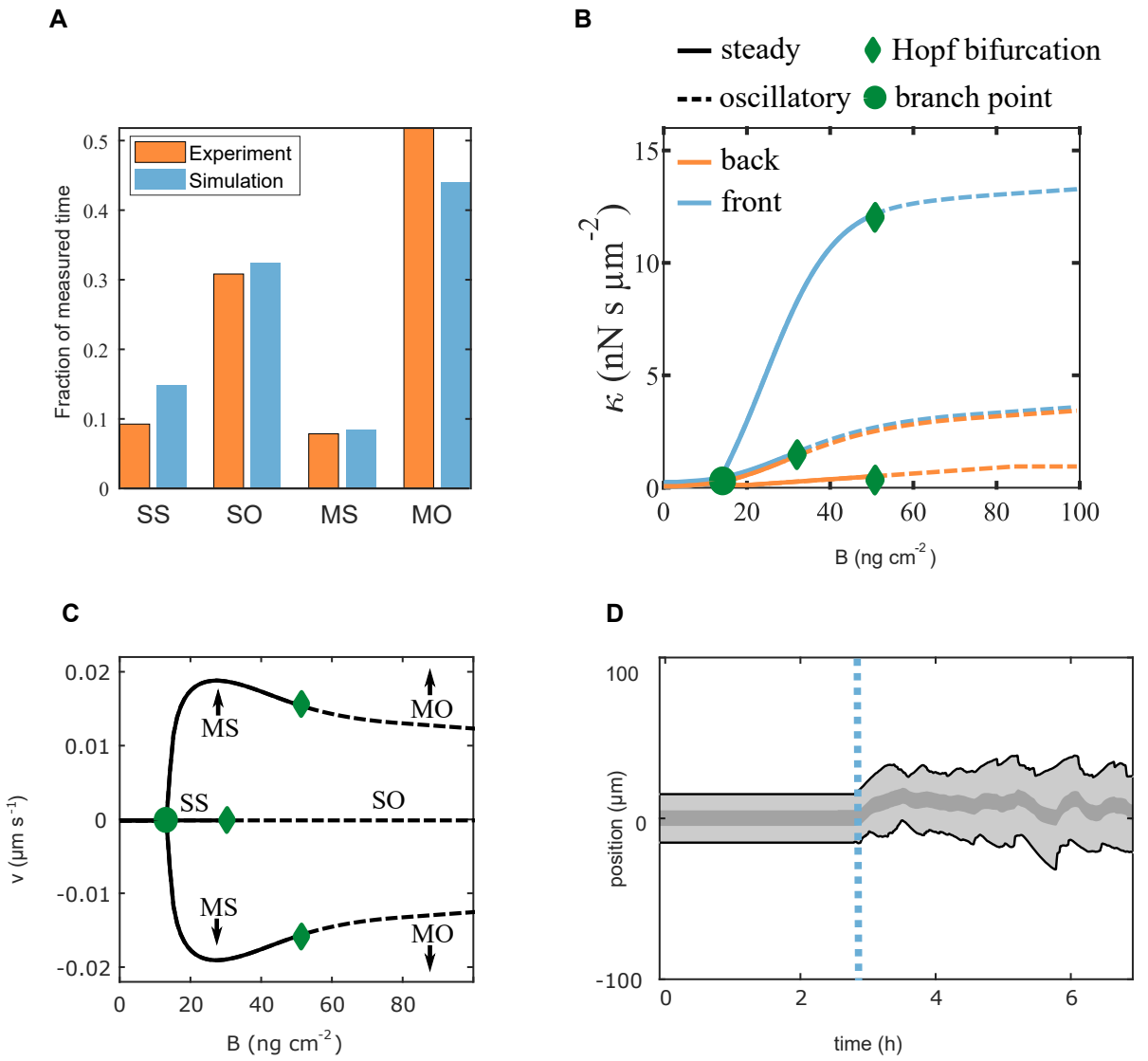

Figure 5.6: Analysis of multistability. **(A)** Fraction of time that cells spend in each of the four motile states for the population average in experiments (2878 h of trajectories) and in simulations sampled from experiments on a range of fibronectin concentrations. **(B,C)** Cell states of the noise-free model are represented by the friction coefficient κ (B) and cell velocity v (C) with respect to fibronectin density B. At low B, only the SS state is present. At the branch point, moving states emerge and coexist with the spread state. Dashed lines indicate oscillations beginning at fibronectin concentrations termed as Hopf bifurcations. All moving states exhibit upward and downward motion (C). **(D)** The steady states are excitable as shown here for SS. Without noise, the state remains steady. However, as soon as noise is switched on, marked by the dashed blue line, excitations are evident. These dynamics are similar to noisy oscillations and can be classified as such by our algorithm despite not being the same state according to dynamical systems theory. Adapted from Amiri, Heyn et al. 2023 [2].

in the back protrusion v_{r_b} is always higher than in the front protrusion v_{r_f} due to the additional edge velocity that pushes the actin network forward:

$$v_{r_f} = v_\mathrm{e} - v_f \tag{5.18}$$

$$v_{r_b} = v_\mathrm{e} + v_b \tag{5.19}$$

$$\rightarrow v_{r_b} > v_{r_f} \tag{5.20}$$

This inequality holds true because v_f would not be the front if both protrusions moved with a negative velocity (v_f and $v_b < 0$). The front protrusion operates in the rising branch ($v_r < v_{r_\mathrm{cr}}$) of the biphasic F-v_r relation (Fig. 5.4 (C) II), while the back protrusion operates on the falling branch [260]. The force at the front edge is thereby higher than at the back which moves the cell forward ($\kappa_f > \kappa_b$ and $F_f > F_b$), Fig. 5.5 (C).

A comparison of the fraction of time that cells spend in each of the four motile states on a population level shows good agreement for experimental and simulated trajectories, Fig. 5.6 (A). For both experiment and simulation, oscillations in the length of the cell (MO, SO) are significantly more prevalent than steady lengths (MS, SS) with moving oscillating (MO) being the most frequent state. The distribution of cell states depends on the fibronectin density B. Panels (B,C) in Fig. 5.6 show a bifurcation analysis of the cell states for a version of the model without noise in the integrin clutch. For low FN densities ($B < 18\,\mathrm{ng\,cm^{-2}}$ for this particular parameter set), only the SS state is accessible. When B is increased up to the first branch point, still only steady protrusion lengths are possible, but the front and back protrusions can have different values of κ, and the cell as a whole can move up or down the lane (MS). This means that for the same value of B the cell can be in an SS, MS↑ or MS↓ state. Panel (C) also displays a biphasic relation for the velocity, with maximum values for $B = 25\,\mathrm{ng\,cm^{-2}}$. However, this should not be confused with the aforementioned plot of the adhesion-velocity relation which displays ensemble averaged data (Fig. 5.1 (B)). Fig. 5.6 (C) does not reveal anything about the distribution of states which influences the averaged velocity values of the ensemble. If B is increased further, to the so-called Hopf bifurcation, the protrusion lengths are no longer steady but start to oscillate (SO and MO). The Hopf bifurcation occurs for smaller B for the spread branch then for the moving branch, resulting in the coexistence of SO and MS for a range of B. For large values of B only SO and MO coexist.

A single cell is characterised in the model by specific parameter values, while the cell population in an experiment reflects numerous parameter sets because of cell variability. Consequently, every possible co-existence pairing may occur within one experiment, allowing both moving states to co-exist with both spread states. To account for cell-to-cell variability, simulations were performed that allowed a variability of ±5% of the parameter values given in Tab. B.2.

So far this analysis has focused only on the noise-free version of the model, i.e. Eqs. 5.5, 5.6 without $\eta(t)$. However, the model captures the observations only if non-linear dynamics are combined with noise. When retrograde flow reaches a velocity of v_slip, it slips, leading to peaks in edge velocity and flow rate, as seen in Fig. 5.5 (B,C), with a sharp drop in the force F. Recovery of κ is gradual and covers most of the period. In the

SS state, characterised by the tension of two opposing forces, the retrograde flow at v_{slip} matches the network extension rate, creating instability against critical κ fluctuations. Such fluctuations might arise from bond changes between the f-actin network and stationary structures. A sufficiently strong perturbation triggers a protrusion-retraction cycle. The random occurrence of these perturbations is called noise, a constant factor in systems as small as protrusions and vital in adhesion and retrograde flow, as indicated by several studies [193, 261]. SS and MS states are excitable (Fig. 5.6 (D)), where minor, yet critical, disturbances provoke large reactions; their cycle post-perturbation mirrors noisy oscillations. Thus, bond noise often causes oscillation-like behaviour even in SS and MS states. Oscillations depend on cell-specific parameters and noise levels, leading to coexistence of oscillation-like and non-oscillation states in SS and MS depending on the noise amplitude. Consequently, we put the noise within the retrograde flow's clutch mechanism, an intracellular process.

5 Transitions Between Cell States

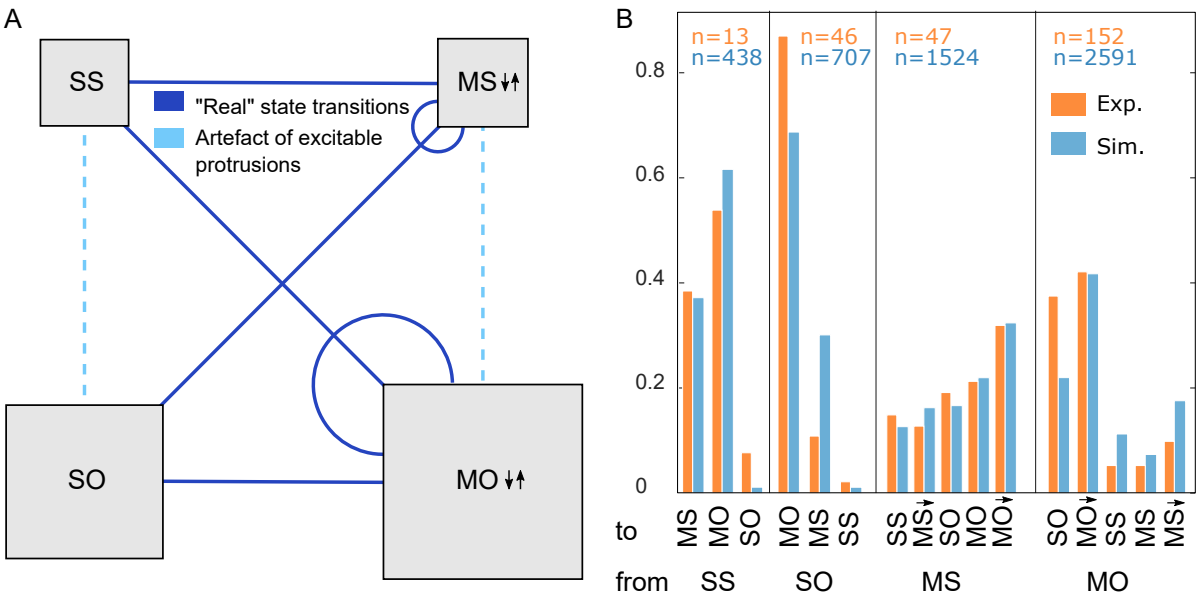

Figure 5.7: **(A)** Schematic of all possible state transitions. The areas of the squares representing the four motile states are proportional to the fraction of time that MDA-MB-231 cells spend in these states, see Fig. 5.6 (A). Dark blue lines show "real" state transitions, while dashed, light-blue lines represent transitions caused by excitations of the two excitable states SS and MS. Transitions in the later case are an artefact of the state classification. **(B)** Frequency plot of the transitions between the cell states for experimental (orange) and simulated data (blue). MS↓ and MO↓ represent reversals of direction. Parameters of all simulations are listed in Tab. B.2. Adapted from Amiri, Heyn et al. 2023 [2].

The phenomenon of multistability is illustrated through transitions, whereby a single cell can exist in multiple states even when there is no variation in the parameters. Within this

framework, states that move upward can co-exist alongside those that move downward and cells can transition from moving to non-moving states and vice versa, see Fig. 5.6 (B,C) and Fig. 5.7. In the context of the biophysical model, these transitions are attributed to stochastic fluctuations within the clutch mechanism of the retrograde flow. It is plausible that the same underlying factor is responsible for transitions in real cellular environments. Due to their minuscule size, cells are notably vulnerable to thermal noise [12, 262, 263].

The bifurcation analysis, Fig. 5.6 (B,C), yields no co-existence of SO and SS, as well as MO and MS, suggesting that there should not be spontaneous transitions between these states. However, this is not what we observed, neither in experiments nor in simulations. These could be perceived as artefacts emerging from the analysis of states. Occasionally, excitable states exhibit oscillations long enough to be classified as an oscillating state, but the detected “transition” does not genuinely represent a state transition. However, the classification algorithm remains consistent across both experimental and simulated datasets, which mitigates concerns about this issue.

Although transitions are postulated to occur spontaneously, it cannot be entirely dismissed that there may be variations in parameter values throughout the duration of the experiment. We did not find any time-dependent changes at the population level, but we cannot exclude the possibility that parameter sets of individual cells might change with the cell cycle. Future work might relate phases of the cell cycle to parameter sets to answer this open question. However, at the population level, simulations of our model with constant parameter sets result in frequencies of state transitions very similar to the observed data, Fig. 5.7 (B).

6 Reversal of Direction

Direction reversal is a critical phenomenon in cell dynamics, and t_{rev} is defined as the precise moment of this reversal. Approximately 10 min prior to t_{rev}, the back protrusion begins to slow down and subsequently shifts into a reverse movement characterised by negative velocity, as depicted in Fig. 5.8 (A-C). Only after this initial deceleration of the back does the front protrusion begin to decelerate, eventually collapsing and manifesting a negative velocity peak, as seen in Fig. 5.8 (A-B,D). Ultimately, both the front and back edges of the cell align to move uniformly.

The underlying mechanism relates to supercritical events that originate in the back protrusion. These events exert a force substantial enough to cause the front protrusion to collapse. In the MS state, this interaction is primarily induced by noise, while in the MO state, it results from a combination of noise and subcritical oscillations.

This analysis indicates a competitive interaction between the rear and front protrusions, reminiscent of a tug-of-war dynamic, that influences the persistence of cellular movement. The duration of persistence is observed to be positively correlated with overall cell velocity, which aligns with the findings of the universal coupling between cell speed and cell persistence (UCSP) by Maiuri et al. [142]. The application of latrunculin A, which impedes actin polymerisation, was modelled by reducing the rate of actin network extension V_{e} in

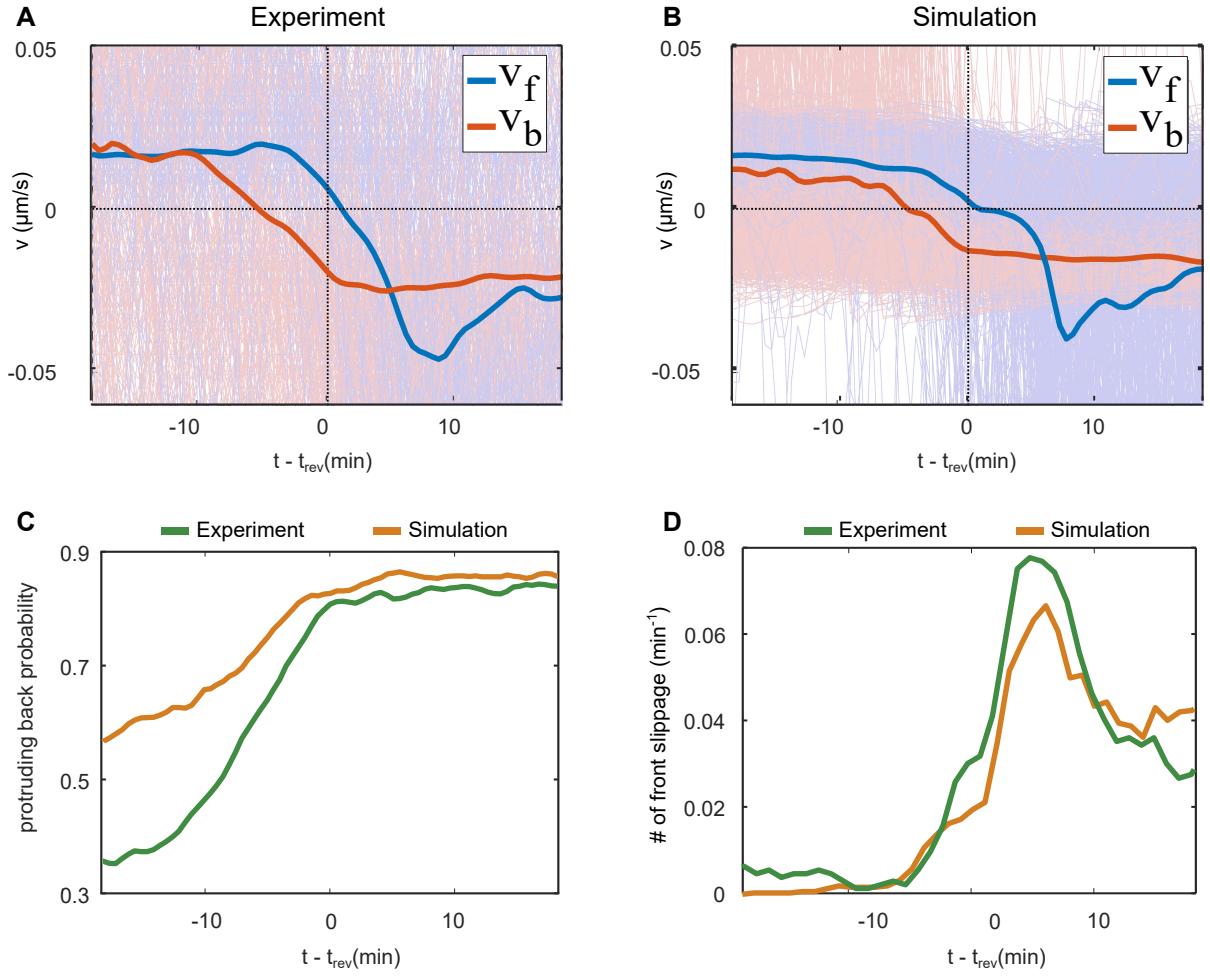

Figure 5.8: Direction reversal mechanism. **(A,B)** The velocities at the front (v_f) and back (v_b) of the cell during reversal transitions, averaged over a multitude of tracks (indicated by thin lines, 221 trajectories for experimental data), are shown for both MS and MO states. The time t_{rev} is defined as the point in time at which the cell nucleus alters its directional movement. A representative example is depicted in Fig. 5.2 (F). The back protrusion starts to slow down and actually has a negative velocity v_b several minutes before the direction reversal of the cell as a whole both in experiments (A) and simulations (B). After the reversal, the (former) front protrusion initially accelerates in the new direction to such an extend that it moves faster than the (former) back protrusion before eventually matching velocities. **(C)** In the minutes leading to the direction reversal, the probability that the back protrusion starts to propagate against the former direction increases. **(D)** Direction reversals go along with an increased number of slippages of the front protrusion, peaking 8 min after the reversal. Adapted from Amiri, Heyn et al. 2023 [2].

simulations. This adjustment led to an increase in persistence time, in agreement with experiments, Fig. 5.9 (A).

The model reveals that, in faster-moving cells, the front protrusion demonstrates greater stability compared to slower-moving cells, whereas the back protrusion exhibits reduced stability. This differential stability contributes to prolonged persistence times. In slower cells, the back protrusion endures longer, exerting a sustained pulling force on the nucleus and front protrusion, which itself produces a lower resistance force. This culminates in more frequent direction reversals and hence in a lower persistence time.

The application of latrunculin A diminishes the actin network extension rate, consequently affecting retrograde flow dynamics in both protrusions. This reduction enhances back pulling but even more the resistance length of the front, ultimately facilitating direction reversal. In conclusion, the described protrusion competition mechanism is rooted in the elastic mechanical linkage between cell protrusions and the cell body, the non-linear friction of the retrograde flow mechanism (clutch), and stochastic variances within the clutch system, providing a coherent framework for understanding UCSP. Cells that move faster exhibit increased retrograde flow resistance in the front and reduced in the rear, thus supporting prolonged migratory persistence.

7 Discussion

For this chapter, I investigated the multistability and dynamics of MDA-MB-231 cells on fibronectin (FN) lanes, focussing on the coexistence of different motile states. To this end I analysed more than 20,000 single cell trajectories in standardised high-throughput experiments. The four states we identified were: spread with steady length (SS), spread with oscillating length (SO), moving with steady length (MS) and moving with oscillating length (MO). We detected spontaneous transitions between motile states which is a hallmark of multistability. Furthermore, we observed the biphasic adhesion-velocity relation and the universal coupling between cell speed and cell persistence (UCSP). We presented a biophysical model that produced simulations which qualitatively and quantitatively matched the observed data suggesting a mechanical mechanism underlying these universal observations of mesenchymal motility. The research revealed that restricting cell motion to one dimension highlighted relationships between motility phenomena. Random migration and UCSP arise from transitions between moving states, influenced by the noisy clutch mechanism of integrin signalling. This mechanism, involving non-linear friction between f-actin flow and stationary structures, is crucial for the cell's multistability and oscillatory behaviour.

The biophysical model consists of three key components: force balance at the cell's protrusion edges, the noisy clutch mechanism, and integrin signalling effects on drag and friction coefficients. The components relate well-established biological observations to mechanical equivalents. The non-linearity in the resulting system of differential equations, in combination with noise, can explain the co-existence of motile states and spontaneous transitions between them.

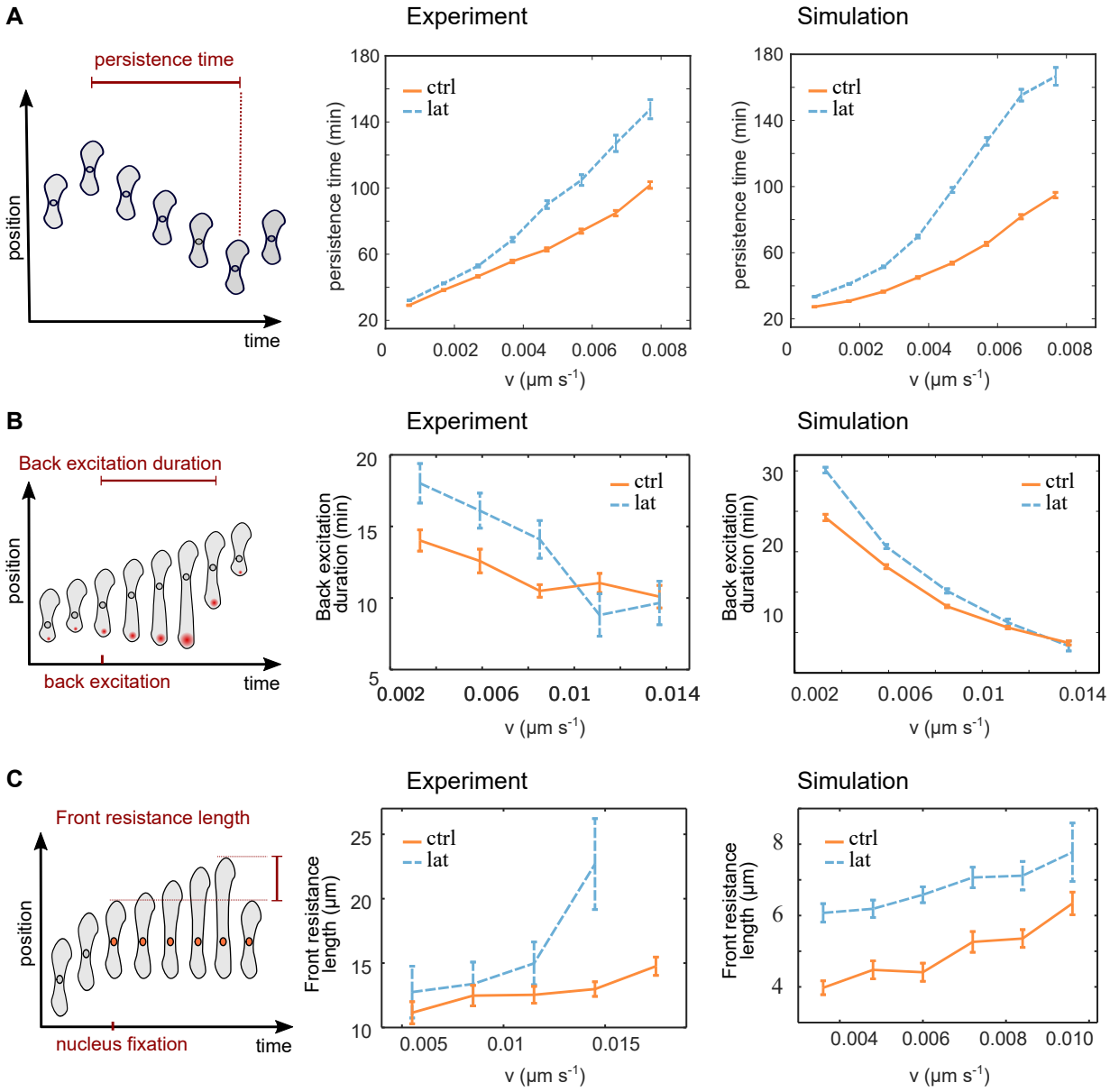

Figure 5.9: **(A)** The cartoon depicts the definition of *persistence time* for this analysis. We defined it as the average time during which a cell body maintains its moving direction on the 1D Fibronectin lanes. The relation between cell speed and persistence time in control cells (9497 experimental trajectories) and with latrunculin A applied (3368 experimental trajectories). Latrunculin A application was modelled by decreasing the network extension rate V_e^0 from 0.030 μm s^{-1} to 0.022 μm s^{-1}. **(B)** Cartoon depicting the concept of back excitation duration. The correlation between back excitation duration and cell velocity is shown through experiments and simulations (221 control experimental trajectories, 127 latrunculin A experiments). At equivalent velocities, latrunculin A's reduction of actin network polymerisation prolongs back excitation duration. **(C)** Cartoon illustrating the concept of front resistance length. Latrunculin A enhances the resistance length of the front protrusion, stabilising cell polarisation. Adapted from Amiri, Heyn et al. 2023 [2].

Our proposition to the ongoing discussion about the mechanism behind the UCSP is that fast cells are more persistent due to a force differential between the front and rear protrusion caused by differences in the retrograde flow of the actin network. This is due to the asymmetric effect of cell speed v on the actin flow, with an increase in the back protrusion (v_{r_b}) and a decrease in the front protrusion (v_{r_f}) at constant actin network extension rate v_e, which effectively stabilises cell polarity.

In both our experiments and model, reducing the network extension rate with latrunculin led to increased persistence. According to our model and results, the noisy clutch mechanism adequately accounts for the UCSP through natural direction changes driven by protrusion competition. Maiuri et al. propose that an increase in network extension rate must correlate with higher protrusion velocity, asserting the proportionality of the velocities $v_\mathrm{e} = av$, where a remains unchanged across different experimental settings [142]. However, reduction of the actin network extension rate by latrunculin A lead to an increased persistence, contrary to the prediction of Maiuri et al.'s theory and in line with our simulations. We therefore have good reason to believe that our assumptions about the mechanism behind direction reversals, namely the protrusion competition caused by geometrical asymmetry of the actin flow, are justified.

Nonetheless, direct quantification of the retrograde actin flow v_r during protrusion oscillations and reversal events would further strengthen our model. Techniques such as fluorescent recovery after photobleaching (FRAP) or fluorescence speckle microscopy are capable of measuring the actin retrograde flow in the lamellipodium and the lamellar region [176, 252, 254, 264–267]. Our examination of cell migration on 1D lanes enhances these measurements by narrowing the focus to the anterior and posterior regions of the cell regarding protrusion dynamics, while cells migrating on two-dimensional substrates may generate protrusions in all planar orientations. The measured retrograde flow velocity can then be compared with predictions of the biophysical model. Observations by Jurado et al. and Vicente-Manzanares et al. support the relation between actin retrograde flow, network extension rate and cell velocity as formulated in Eq. 5.20 but I am not aware of any such data for MDA-MB-231 cells [83, 252].

Future work should also address cell-to-cell variability within the framework of our biophysical model. The variability in this chapter was modelled by drawing from distributions of parameter values with a variability of ±5%, see Tab. B.2. We did not discriminate between different sources of variability but applied the 5% spread to all model parameters. Although this resulted in an ensemble of simulations similar to the experimental data, a more nuanced approach would be preferable. To this end, the approach discussed in Chapter 4 could provide insight into the sources and magnitudes of variability with respect to the model parameters. This would help answer the question which parameters are similar for all cells of a given population and which parameters are highly depended on the individual cell.

For this study, we thoroughly tested our biophysical model against trajectories of MDA-MB-231 cells. Since the model constituents are well established for a number of other cell lines and the model reproduces universally observed phenomena such as the adhesion-velocity relation, multistability and the UCSP, we hypothesise that our model is

universally applicable for mesenchymal cell migration. However, this hypothesis needs to be tested by analysing more and different cell lines on 1D lanes.

The model offered an explanatory connection between the biological processes that make up the model constituents and the resulting motile dynamics. This connection may be used to retrieve cell-specific parameters that explain differences between cell populations, as well as characterise the cytoskeletal mechanisms behind cell migration. However, this requires parameter optimisation in the context of non-linear stochastic systems, which poses a challenging problem. A solution to this problem is presented in the following chapter.

Cell-Mechanical Parameter Estimation using Simulation-Based Inference

For this chapter, I applied simulation-based inference (SBI) to identify cell-specific parameters influencing migration in healthy and cancerous human epithelial cell lines, MCF-10A and MDA-MB-231, respectively. Using 1D trajectory data from automated imaging on micropatterned fibronectin lanes, a neural density estimator (NDE) was trained to infer parameters related to cell dynamics. The results revealed significant differences in actin polymerisation and protrusion length between the two cell lines. SBI effectively captured the effects of two cytoskeletal inhibitors, offering insights into cytoskeletal mechanics and their role in cell motility, which is crucial for understanding metastasis in cancer biology. The content of this chapter is based in large parts on our preprint "Cell-mechanical parameter estimation from 1D cell trajectories using simulation-based inference" by J.C.J. Heyn, M. Atienza Juanatey, M. Falcke and J.O. Rädler [4] to which I contributed in investigation, data curation, visualisation and writing.

Automated time-lapse acquisition and image analysis of cells in 1D confinement give access to large sets of 1D single cell trajectories, as I have shown in previous chapters. When combined with mathematical modelling, these data sets can provide insights into the mechanisms of cell migration. One such mathematical model is our biomechanical model first introduced in Schreiber et al. 2021 [1] and extended in Amiri et al. 2023 [2]. As could be shown, the model quantitatively captures observed phenomena such as the biphasic adhesion velocity, the UCSP, and the characteristic motile states (as well as their transitions) in good agreement with experimental data. However, the non-linear, inherently stochastic nature of our biomechanical model presents significant challenges, as the impact of parameter variations is often non-intuitive. Consequently, parameter optimisation becomes both mathematically and conceptually difficult, with the high dimensionality of the problem rendering rigorous Bayesian inference computationally impractical. This problem, of course, exists not only for our own model, but also for most complex biomechanical models [138, 183, 184, 268]. As a result, researchers frequently rely on intuition or trial-and-error methods for parameter exploration, which are labour-intensive and unsystematic. A systematic and scalable framework for inferring parameters from large-scale cell motility datasets would enable data-driven insights into the regulatory

networks governing cell motility. In recent years, advances in the field of machine learning made new tools available that estimate optimal parameter sets of mechanical models based on large sets of training data. One such promising tool for parameter optimisation is simulation-based inference. As described in Fundamental Concepts SBI is based on a neural network architecture called neural density estimator (NDE). To train SBI, parameter sets are drawn from the prior distribution, which represents a range of candidate values, to generate simulated data using the mechanical model. Subsequently, the deep neural network is trained to infer the parameters that govern the simulated data. Once the neural density estimator is trained, it is applied to the experimental data to estimate the posterior distribution of the underlying parameters. This approach has already been adopted in several studies as a systematic method of parameter optimisation in mechanistic models [209, 213, 269, 270]. However, we are the first, to our knowledge, to apply SBI in the context of 1D cell migration.

1 SBI Correctly Estimates Parameters of Simulated Data

We started by simulating 1D cell trajectories of 24 h length, using the biomechanical model as described in Amiri et al. [2]. Initial attempts with trajectories of shorter durations had resulted in broad posterior distributions with smeared out peaks (data not shown). We divided the simulated data into a training and a test data set. The neural density estimator was trained on the training data set with the goal to estimate a posterior distribution for each free parameter from a single trajectory with a known uniform prior, see Materials and Methods. We then tested the trained neural density estimator on simulated data from the test data set to which the network had not been exposed to. We compared the inferred posterior distributions to the parameter sets that were actually used to simulate the data. It became quickly apparent that the number of free parameters that are the target of the neural density estimator had to be reduced because the estimated posterior distributions were too smeared out and the true parameter values could not be identified precisely, see Fig. 6.1 for the inference results for 10 free parameters. The problem, that density estimation becomes drastically harder as dimensionality increases is called the *curse of dimensionality* [271, 272]. Consequently, we reduced the complexity of the model by fixing a number of parameters to constant values and removing some degrees of freedom that had a negligible influence on the model's dynamics, see Supplementary Information. The 5 most influential model parameters that we chose as targets for SBI are the following:

- L_0: resting protrusion length,
- V_e^0: actin network extension rate,
- k_on: on-rate for dynamic integrin signalling,
- κ_max: maximum friction coefficient for integrin signalling,
- v_slip: critical retrograde flow velocity.

A complete table of the fixed and variable parameters along with a short description and the prior values can be found at the Supplementary Information, Table B.3.

With the now reduced number of free parameters, we used 1,000,000 simulated trajectories with known parameter values to train an NDE to infer the posterior distributions of the 5 parameters listed above. The confidence level of the NDE was determined via simulation-based calibration, see Supplementary Information. We found the trained NDE to be unbiased and well calibrated, see Fig. B.7. To test the accuracy and predictive power of the NDE we exposed it to test trajectories, i.e. simulated data with known parameters. Just as for experimentally observed data, the test data would exhibit directional changes, varying cell velocities and oscillating protrusion lengths. An example of a simulated trajectory is displayed in the lower left corner of Fig. 6.2. The parameter set used for this particular trajectory is indicated as vertical orange lines in the plots displaying the posterior distributions on the diagonal and as white crosses in the plots of joint distributions in the right-hand corner of the figure. The x-axes of the plots on the diagonal represent the parameter values with the range set by the prior, the y-axes represent the probability $p(\theta_i)$. The uniform posterior is indicated by grey horizontal lines for each parameter and the inferred posterior distribution $p(\theta_i \mid \mathbf{x})$ by bold blue lines. All inferred distributions display a symmetric, pronounced peak, centred around the true parameter value as indicated by the orange line. This result validates our approach as it implies an accurate and unbiased inference. For the heat maps on the off-diagonal plane, the colour indicates the joint probability $p(\theta_{i,j} \mid \mathbf{x})$ with dark blue being the lowest probability and bright yellow the highest. The sensitivity with which parameters are inferred shows variation. Parameters such as the resting cell length L_0 and the network extension rate V_e^0, which display a sharp prior distribution, can be estimated with particular precision. To summarise, utilising a simulated trajectory with known parameters on the trained NDE accurately infers posterior distributions for five free parameters that encompass the desired parameters with the method's precision.

2 Parameter Estimation from Experimental Trajectories

After the successful validation of the approach on simulated data, we applied the NDE to experimentally obtained trajectories. The NDE estimates the posterior probabilities for the experimental trajectory. Unlike for the simulated data, there is no ground truth or known true parameter set θ_{true} on which the estimates can be validated. Consequently, we used the most likely parameter set to simulate new trajectories to see if the inference results were plausible. The simulated trajectory was then subjected to the NDE. This routine tests if the biophysical model and the parameter sets inferred by the NDE capture the motile dynamics of the cells.

Examples of 24 h long experimental trajectories $\mathbf{x}_{\text{E}}(t)$ of MDA-MB-231 cells are shown in Fig. 6.3 (A, E). The trajectory in Panel (A) displays little movement of the cell's nucleus but constant oscillations of the cell's protrusion lengths, corresponding to an SO-state. In Panel (E), the trajectory is constantly moving in the same direction but slows down

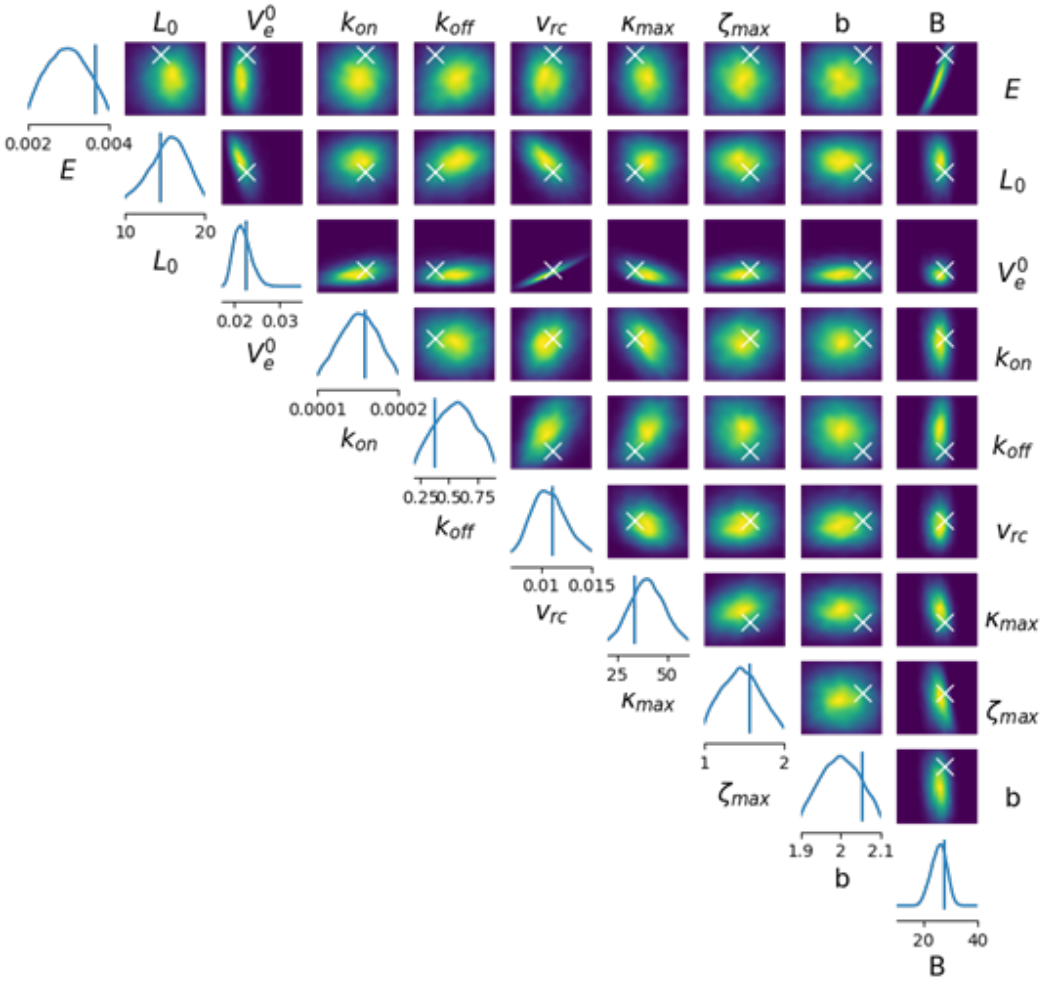

Figure 6.1: A large number of free parameters leads to imprecise inference results. A neural density estimator trained to infer the posterior probabilities $p(\theta \mid \mathbf{x})$ of 10 free parameters is applied to a simulated test trajectory. The line plots on the diagonal represent the posterior distribution for each individual parameter $p(\theta_i \mid x)$, the 2D heatmaps above the diagonal show the distributions for each pairwise-combination of parameters $p(\theta_{ij} \mid x)$ with blue representing the lowest and yellow the highest probability for a parameter combination. Vertical lines in the plots on the diagonal and white crosses in the plots on the off-diagonal represent the values that were used for the simulated trajectory. The pairwise distributions indicate correlations such as for B and any other parameter or for v_{rc} and V_{e}^0. The fact that the posterior distributions are smeared out across the range of prior distributions, as marked by the range of the x-axis, indicates that the imprecision of the NDE is in the order of the system size and consequently offers little insight.Adapted from Heyn, Atienza Juanatey et al. 2024 [4].

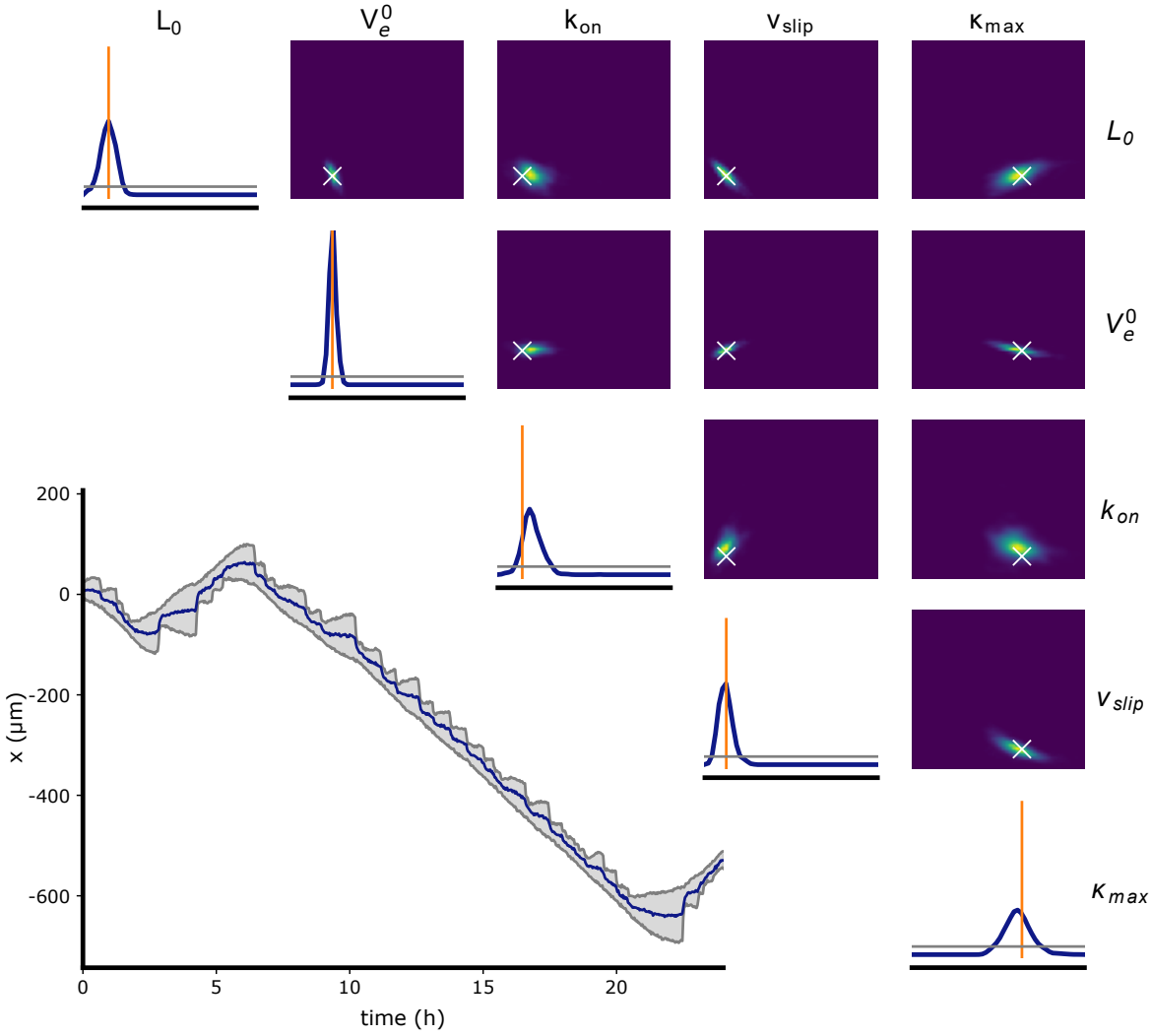

Figure 6.2: Simulation-based inference predicts the correct parameter values for simulated trajectories. The distance-time graph in the lower left corner shows a simulated trajectory as described by eqs.5.2-5.4. The blue line represents the position of the nucleus $x_{\mathrm{c}}(t)$ and grey lines represent the front and back of the cell $x_{\mathrm{f,b}}(t)$. The plots on the diagonal show the corresponding posterior probabilities $p(\theta_i \mid \mathbf{x})$ as inferred by the trained neural density estimator (NDE) as blue lines. The limits of the x-axis correspond to those of the prior, see Table B.3. Vertical orange lines indicate the true parameter values used for the simulated trajectory shown here. Horizontal grey lines represent the uniform prior. The heatmaps in the upper right hand corner show the posterior distributions for each pair of parameters $p(\theta_{i,j} \mid \mathbf{x})$ with the true parameters plotted as white crosses. Adapted from Heyn, Atienza Juanatey et al. 2024 [4].

noticeably after ca 9 h. At the same point in time the initial length oscillations stop and the cell length remains constant for the rest of the observation time. Panels (B,F) show the posterior distributions $p(\theta_{\mathrm{E}} \mid \mathbf{x}_{\mathrm{E}})$ as inferred by the NDE. For both trajectories, the posterior distribution for the actin network extension rate V_{e}^{0} is sharply peaked, whereas the distribution for v_{slip} is quite expansive and nearly resembles a uniform posterior distribution (indicated by the horizontal grey line). The resting protrusion length L_0 displays a pronounced peak for trajectory (A), which is in the same motile state throughout the observation time. For the trajectory (E), which changes its motile behaviour, the distribution for L_0 is much broader. The integrin parameters k_{on} and κ_{max} are comparable for both trajectories. Panels (C,G) show simulated trajectories sampled from the most likely parameter values in Panels (B,F), respectively. The simulated trajectories display a noticeable similarity to their experimental counterparts. The overall net displacement (or lack thereof for Panels (A,C)), speed and length oscillations appear to be well captured, particularly for Panels (A,C). However, the transition from oscillating to steady protrusion lengths in Panel (E) is not visible in Panel (G). The posterior distributions for the simulated trajectories can be seen in Panels (D,H). The distributions are very similar to those in Panels (B,F), respectively. However, the inferred distributions for k_{on} in (D) and for v_{slip} in (H) are not better than the uniform prior. This means that the NDE either could not infer any more information from the simulated data regarding the concerned parameters or that all values within the prior could lead to such simulation results. Additionally, the fact that the posterior distributions for the experimental trajectories and simulated trajectories vary, implies that the biophysical model, while successfully reproducing all observed motile states, does not reproduce all aspects of the experimental data which the NDE uses to infer parameter distributions. Some details seem to get lost, which results in slightly different trajectories.

However, overall, SBI can reliably infer probabilistic distributions of parameters for single cell trajectories. Following this, we demonstrate that the parameter sets inferred for populations of different cell types provide a significant characterisation, allowing the distinction between cell lines.

3 Inference of Cell Type Specific Properties

The large intrinsic cell-to-cell variability means that single-valued metrics do not characterise cell types well, see Chapter 4. A good characterisation of the motile behaviour of one cell might be completely wrong for another cell of the same cell line. It seems therefore natural to compare not single values but distributions of properties when comparing different ensembles of cells. To this end, we analysed $\mathrm{N_{MDA}} = 85$ single cell trajectories for the breast cancer cell line MDA-MB-231 and $\mathrm{N_{MCF}} = 301$ single cell trajectories for the healthy breast epithelia cell line MCF-10A. Ten randomly chosen trajectories per cell line can be seen in Fig. 6.4 (A,B). The invasive MDA-MB-231 cells generally display a more active motile behaviour compared to that of the healthy cell line MCF-10A. However, there is also a fraction of MDA-MB-231 cells that is spread and does not show any displacement,

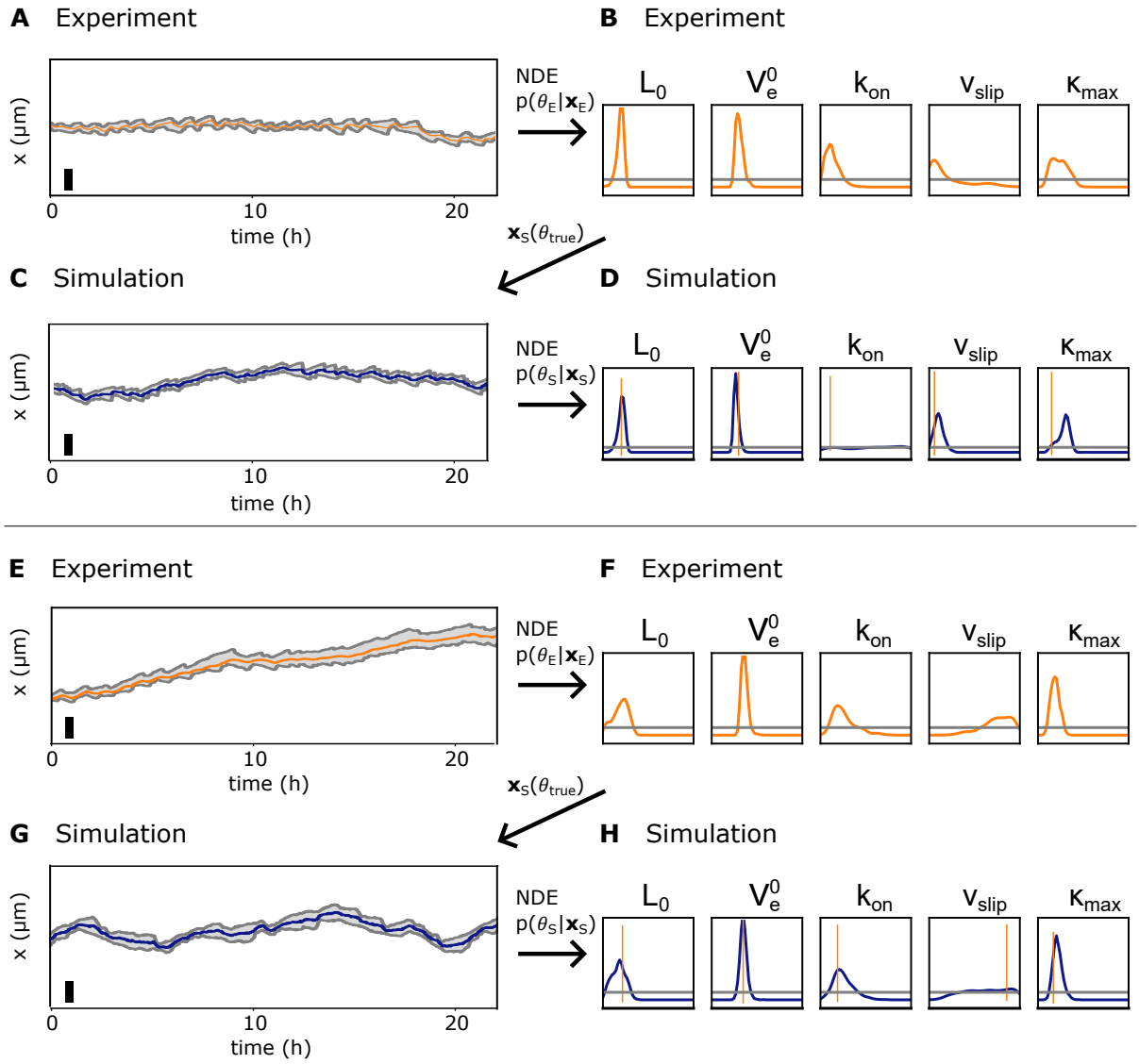

Figure 6.3: Inference of posterior probabilities for experimental data. **(A)** A typical 24 h long trajectory of an MDA-MB-231 cell. The cell shows little displacement but oscillatory changes in its protrusion lengths. The histograms in panel **(B)** display the posterior distributions $p(\theta_\mathrm{i} \mid \mathbf{x})$ for the five free parameters as inferred by the neural density estimator (NDE). Horizontal grey lines represent the uniform prior, again. The most likely parameter values θ_true for the trajectory in (A), i.e. the maximum values of the distributions in (B), were used for the simulation of the trajectory in **(C)**. Just like the experimental trajectory, the simulated trajectory displays oscillating protrusions and little displacement. **(D)** The NDE correctly estimates the values of L_0 and V_e^0 but does not provide a better estimate for k_on than the uniform prior. Panels **(E-H)** are analogous to panels (A-D). However, the trajectory in panel **(E)** is constantly moving albeit at different speeds. The protrusion lengths in (E) oscillate for the first 9 h before staying relatively constant. The inferred posterior distribution for V_e^0 is again prominently peaked **(F)**. The simulation in **(G)** captures the movement of the cell's nucleus well and much better than the protrusion oscillations. The posterior distributions in **(H)**, again peak nicely for L_0 and V_e^0 but are no better than the uniform prior for v_slip. Vertical scale bars in (A, C, E, G) represent 100 µm, vertical orange lines in (D, H) show the most likely parameter set θ_true. Adapted from Heyn, Atienza Juanatey et al. 2024 [4].

see also Chapter 5. The NDE estimated a posterior distribution for the model parameters for each trajectory individually. These posterior distributions were merged for each cell line, resulting in an ensemble distribution of cytoskeletal parameters, see Fig. 6.4 (C).

The ensemble distributions reveal that the primary differences between the MDA-MB-231 and MCF-10A cell populations lie in the distribution of the parameters L_0 and V_e^0, with MDA-MB-231 exhibiting a notably faster actin network extension rate. Both populations show a wide and almost uniform distribution concerning the parameters k_{on} and v_{slip}. Either the NDE can't infer these parameters with any certainty or each trajectory has it's own distinct values for these parameters, resulting in a uniform distribution when averaged over the population. The examples in Fig. 6.3 suggest it to be a combination of the two. Both cell lines display a similar peak in the distribution of κ_{max}, suggesting a consistently preserved signalling pathway among the cell lines.

In summary, determining five cell-type-specific model parameters via SBI facilitates an objective and automated analysis of cell characteristics. The resting length L_0 and the extension rate of the actin network V_e^0 emerged as the most notable cell parameters.

4 SBI Analysis on the Effect of Inhibitors

To evaluate SBI's potential further, we expose both cell lines to the cytoskeleton inhibitors latrunculin A and Y-27632. Latrunculin A interferes with f-actin polymerisation; Y-27632 specifically targets the Rho-associated protein kinase (ROCK) within the Rho/ROCK pathway, see Fundamental Concepts. We use the trained NDE, without applying any pre-existing knowledge about the inhibitors' mechanisms, to analyse the data sets. Treatment with latrunculin A, when compared to the untreated control group in both MDA-MB-231 and MCF-10A cells, leads to changes in the estimated posterior distributions in only one parameter. Only the actin polymerisation rate (V_e^0) shows a significant decrease upon treatment, see Fig. 6.5 (A). Similarly, Y-27632 decreases the polymerisation rate, too, but additionally also shifts the probability distribution of the resting protrusion length L_0 towards greater values, Fig. 6.5 (B).

The changes inferred in the parameter probability distribution align well with the expected effects of the inhibitors. For latrunculin A, we anticipate a reduction in the actin network extension rate V_e^0 because latrunculin A binds specifically to the barbed ends of actin filaments. In our model, all other parameters are unrelated to actin polymerisation and should remain unaffected by latrunculin A. The resulting distribution functions correspond closely to these expectations.

The Rho/ROCK pathway is a crucial regulatory element in mesenchymal cell migration, exhibiting complex effects. ROCK phosphorylates LIM kinases, which subsequently phosphorylate cofilin, a critical regulator of actin turnover that depolymerises f-actin. By phosphorylating cofilin, ROCK/LIMK effectively inhibits actin depolymerisation. Additionally, ROCK enhances myosin II activity and contractility by preventing myosin light chain (MLC) dephosphorylation. Moreover, Rho and ROCK regulate cell-substratum adhesion by promoting the assembly and turnover of focal adhesions [56].

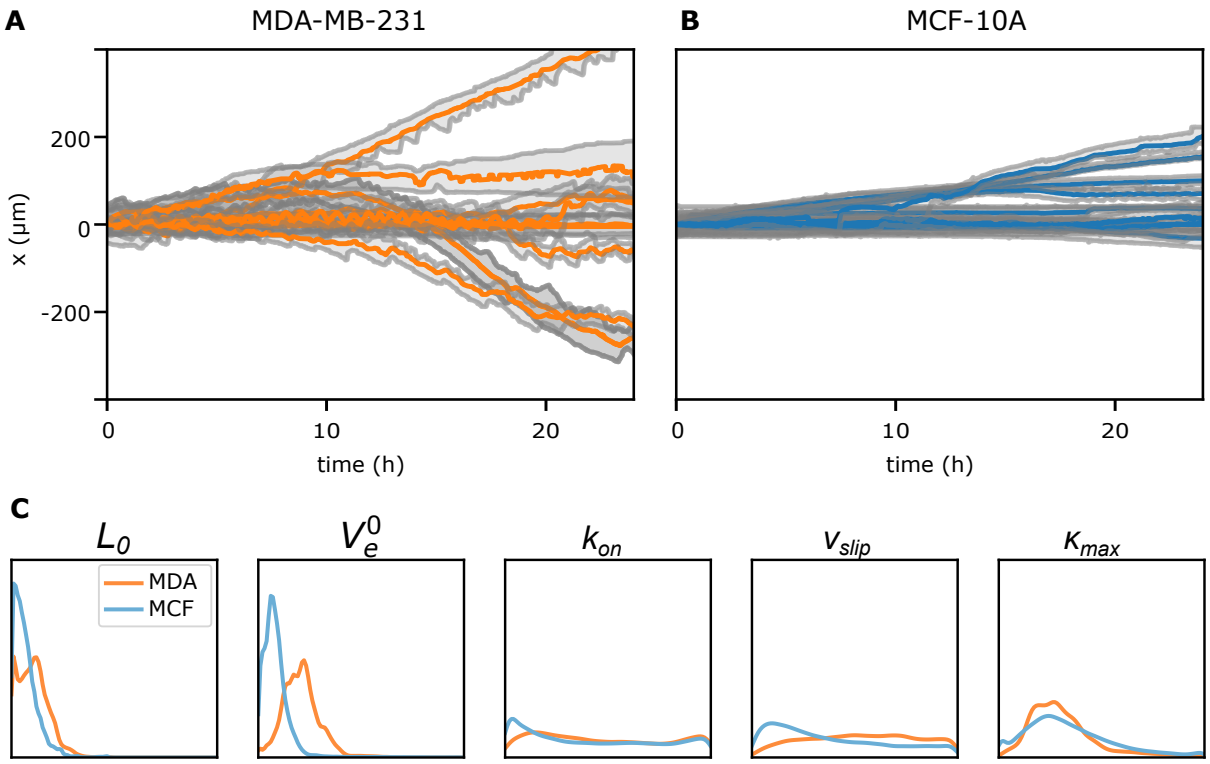

Figure 6.4: Inference of cell type specific properties. **(A,B)** Shown here are 10 randomly chosen experimental trajectories for the breast cancer cell line MDA-MB-231 and the healthy breast epithelia cell line MCF-10A, respectively. Trajectories of the invasive MDA-MB-231 cell line generally display a bigger motile activity compared to that of the healthy cell line MCF-10A. **(C)** Ensemble posterior distribution of estimated model parameters via SBI. The plots show the ensemble average of all sampled points for all trajectories of a given population (N_{MDA} = 85, N_{MCF} = 301). The parameters that stand out most distinctly are the resting length L_0 and the actin polymerisation rate v_e^0. Adapted from Heyn, Atienza Juanatey et al. 2024 [4].

Srinivasan et al. observed that the inhibition of ROCK by Y-27632 in healthy primary keratinocytes (HPKs) and epidermal carcinoma cell line (A-431 cells) resulted in the loss of migration, contractility, focal adhesions, and stress fibres [273]. Our SBI analysis indicates that Y-27632 reduces the polymerisation rate and prolongs the resting length of cells, likely due to diminished contractility, which aligns with the general understanding of Rho/ROCK signalling. It is unexpected, though, that Y-27632 does not lead to clear changes in focal adhesion parameters k_{on} and κ_{max} which is what we would expect from the ROCK inhibitor. However, these parameter distributions appear too broad and insensitive to show treatment effects.

In summary, we demonstrate that SBI effectively captures the effects of the inhibitors latrunculin A and Y-27632 within an interpretable parameter space. An important finding is the observation that the consistent reactions of both cell lines to the same treatments suggest a common underlying mechanism.

5 Discussion

Estimating the optimal parameter set of complex, non-linear models, such as our biophysical model of single cell motility, for real-world data is a mathematically and conceptually challenging problem. We introduced simulation-based inference (SBI) as a method to solve this problem. Using our biophysical model as simulator, we trained a neural density estimator (NDE) on 1,000,000 simulated cell trajectories to estimate posterior distributions over the biophysical model parameters. We showed that the trained NDE could successfully and without bias estimate posterior distributions based on observed data. These distributions suggest the most probable values for the parameters, while also measuring uncertainty and highlighting possible interactions among them. SBI can not only characterise single trajectories but whole populations of cells, too. Because the inferred parameters of the mechanistic model are interpretable, the results allow a meaningful characterisation and comparison of migratory phenotypes and cytoskeleton inhibitors.

While SBI proved overall successful in this context, we also identified a number of limitations to the approach. The initial number of free parameters had to be reduced to improve the certainty of the inference procedure. Noise obfuscated the true parameter set underlying the trajectories. As discussed in Chapter 4, noise can be found both on a population level (cell-to-cell variability) and on a single cell level. While intra-cellular sources of noise are inevitable and even a necessary aspect of a good characterisation of cell motility, external sources of noise and the influence of latent variables should be eliminated as far as possible. The experimental setup for this study was designed with standardisation and reproducibility in mind. However, it is questionable whether the fixation of the parameter for the fibronectin density B of the model is completely justified by the experiment because small local inhomogeneities can already influence the motile behaviour of cells [1, 2, 171].

In line with the results of Chapter 4, we anticipate that enhancing the data foundation by improving spatial and temporal resolution will further advance the SBI methodology to

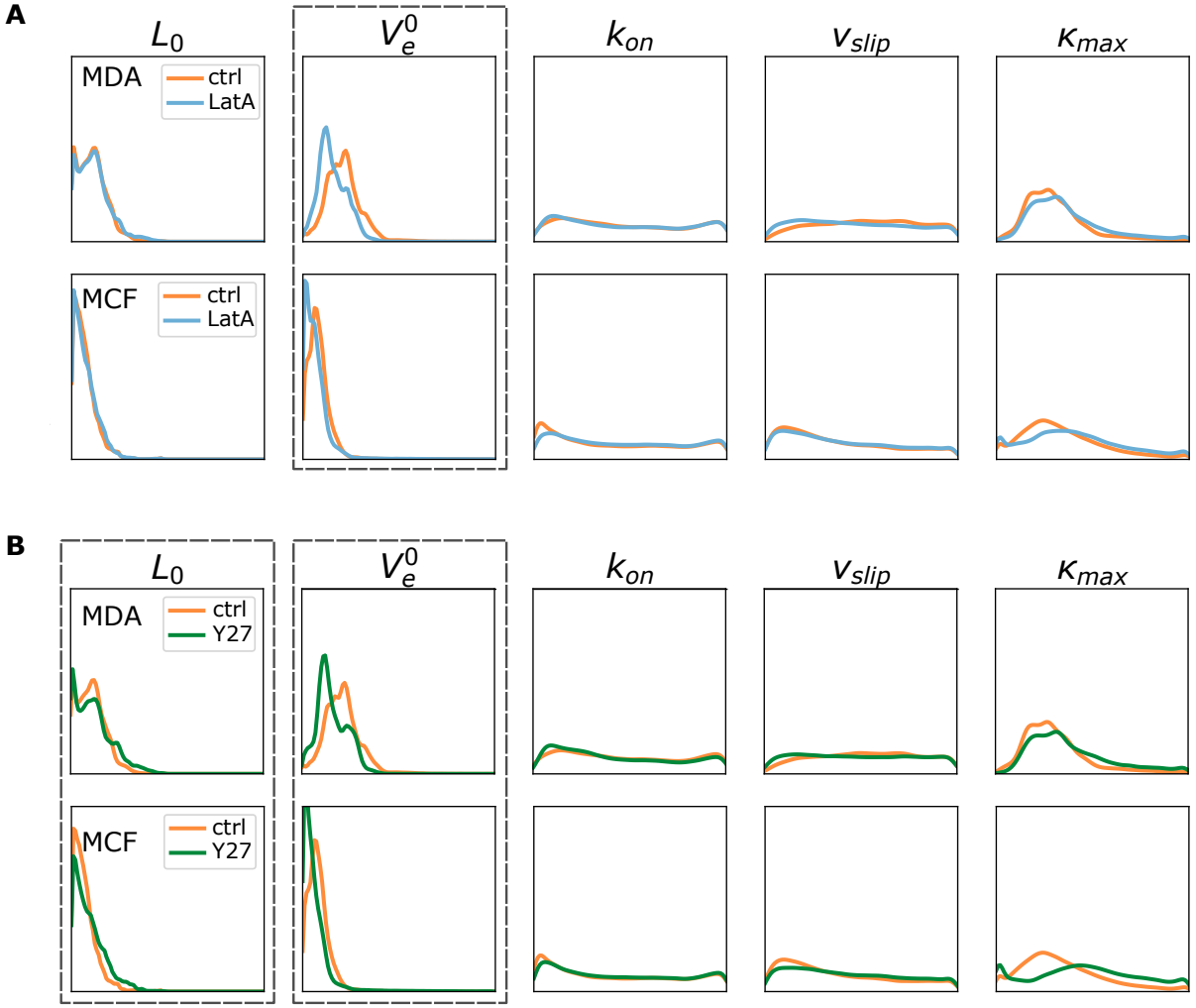

Figure 6.5: Ensemble posterior distribution for trajectories of cells treated with cytoskeletal inhibitors. **(A)** MDA-MB-231 and MCF-10A cells were exposed to latrunculin A (LatA), an inhibitor of actin polymerisation, and a control treatment (ctrl). The plots show the ensemble posterior distributions for the five model parameters as estimated by the neural density estimator (NDE). Latrunculin A treatment leads to a significant decrease of the most likely ensemble values for the actin network extension rate V_e^0 for both cell lines. All other posterior distributions remain unchanged. **(B)** Treatment with the ROCK-inhibitor Y-27632 (Y27) has a similar effect on V_e^0 as latrunculin A. However, Y-27632 also shifts the resting protrusion length L_0 towards larger values. MDA-MB-231 experiments: 5 replications, N_{MDA_ctrl} = 85, N_{MDA_LatA} = 129, N_{MDA_Y27} = 96; MCF-10A experiments: 4 replications, N_{MCF_ctrl} = 301, N_{MCF_LatA} = 465, N_{MCF_Y27} = 507. Adapted from Heyn, Atienza Juanatey et al. 2024 [4].

a certain degree. In our study, we achieved a balance between spatio-temporal resolution and the number of cell trajectories. A higher spatio-temporal resolution inevitably leads to a lower number of cell trajectories per measurement, see Chapter 3. The crucial factor for data quality is the length of each trajectory; short trajectories lack sufficient information to confidently deduce model parameters, whereas longer ones are eventually restricted by the cell division cycle. Increasing the number of trajectories of the same length does not necessarily improve SBI's ability to characterise population ensembles because the information content saturates. It also stands to question whether increasing the temporal resolution (2 min for this study) would lead to better inference results. Whereas the generalised Langevin equation (GLE) (Chapter 4, Eq. 4.1) aims to capture dynamics of all time scales, the biophysical model presented in Chapter 5 was designed with the time scale of a few minutes to several hours in mind. Dynamics on the time scale of seconds, such as membrane ruffles, are not actively accounted for and experimental data including these dynamics might therefore actually not improve SBI. Consequently, future research should focus on expanding the dimensions of the trajectory by incorporating additional metrics. Sensitivity analysis of the biophysical model suggests that measurements like actin retrograde flow velocity or focal adhesion density could greatly enhance SBI's accuracy. The simulator, i.e. the biophysical model, is no black box and knowledge about variables that have so far been treated as latent can be leveraged to increase the certainty of the NDE. The NDE could be tweaked to sample only data in which latent states, such as e.g. force balances, adhere to the physical constraints of the model. To this end, it would also be worthwhile to analyse the summary statistics of the trajectories that are calculated during the feature extraction step, see Fig. 2.6. Investigating the summary statistics of the trajectories might reveal which extracted features are most crucial for NDE. A complementary approach would be to use an autoencoder [274–276]. The autoencoder compresses the data into a low-dimensional vector before expanding it again to represent the original data. This process could be leveraged to find coordinates and governing equations that might describe cell trajectories even better than our current biophysical model. Physics-informed neural networks (PINNs), neural networks that respect the laws of physics, are currently a very actively researched topic [277–281]. The key idea here is to create a loss function that penalises results of the neural network that do not adhere to physical laws or prior domain knowledge. Insights from this research might both support solving the inverse problem and guide the design of mathematical models of cell motility.

High-throughput motility assays are vital for identifying cell-specific characteristics. The standardised confinement of The First World Cell Race, by Maiuri et al., is used to evaluate the speed and persistence of various cell lines [32, 142, 216, 282]. Unlike model-free AI methods, SBI, based on a mechanistic model, infers interpretable features of cell motility. Automated platforms that use SBI with established models can develop standardised parameter databases, potentially advancing cell mechanics, pharmaceuticals, and clinical research [229, 231]. SBI can extend to other cell motility models, such as those that capture cell protrusion dynamics on shorter time scales [127, 283]. Overall, any complex dynamic phenomenon that can be statistically quantified and represented with non-linear partial differential equations is amenable to SBI.

The SBI analysis of cell trajectories presented in this study integrates hypothesis-driven modelling with AI-enabled analysis, which makes it highly beneficial for enhancing our understanding of locomotion.

Conclusion and Outlook

In this thesis, I presented an automated time-lapse analysis of single-cell migration using a high-throughput migration platform and a biophysical model. The comparison of experimental data to models, which required reproducible and standardised conditions as well as large-scale statistics, was made possible by this automated analysis. The scanning time-lapse setup of 1D FN lanes enabled the collection of an extensive number of single-cell trajectories. The data was used to investigate cell-to-cell variance, to explore the broad spectrum of motile behaviour and to scrutinise a cell-mechanical model. We applied a machine-learning approach to assign parameter values of the model to characterise different cell types and identify the site of action for two drugs. This work enables ample testing of universality claims by allowing rapid analysis of numerous cell types.

We found that previous throughputs of hundreds of single-cell trajectories per week on a comparable setup by Schreiber could be increased to several thousand trajectories in the same time [34]. The key to this improvement was the fabrication of 1D FN-coated lanes by photopatterning, in combination with deep learning-based image analysis. Photopatterning improved the quality of the lanes compared to the microprinting method in terms of the homogeneity of the FN coating, resulting in a lower number of rejected imaging positions and hence more imaged cells. In summary, the current state of photoactive microfabrication for cell migration is relatively advanced, attributed to its efficiency, cost-effectiveness, and reproducibility. However, the present photopatterning protocol still involves many manual steps that are time-consuming and error-prone. This limitation can be mitigated by switching from a mask-less photopatterning protocol to a mask-based version. Parallel UV-illumination and sufficiently sized masks render scanning the substrate, a characteristic of mask-less devices like the Primo module, superfluous and make it possible to treat multiple substrates in parallel.

In its present state, the migration assay is designed primarily for simplicity, sometimes at the cost of physiological resemblance. More physiological conditions could be achieved by changing some of the experimental conditions. The imaging dishes used in this thesis had a plastic cover slip bottom. This facilitated reproducible protein coating but with a Young's modules in the range of 25 GPa it is several orders of magnitude stiffer than epithelial tissue, which covers a range from a few kPa to a few MPa [284]. This difference in stiffness is problematic because cells sense and respond to the stiffness of their substrate

which may change their shape and morphodynamics [285]. A solution would be to coat the substrate with PDMS to reduce its stiffness before applying a micropattern [286]. Furthermore, the complexity of *in vivo* environments can be modelled by exchanging the fibronectin-only coating with a coating that contains other ECM proteins, too, such as collagen and fibrinogen. To further increase the versatility of the platform, the imaging dishes could be replaced by channel slides, i.e. imaging slides that carry six parallel channels, each with its own in- and outlet. The channels would add the functionality of a microfluidic setup, including the possibility to exchange reagents, vary the flow rate of the cell culture medium and change the viscosity of the medium, all live during the measurement. This can be used to scrutinise cell-mechanical models as I will discuss further down.

The biophysical model presented in this thesis uses a novel combination of well established model constituents. We assume the force balance, the noisy clutch and integrin signalling to be ubiquitous in mesenchymal cells and, consequentially, our model to be universal. However, the universality of the model needs to be tested. To this end, future work should involve the analysis of additional cell lines, Fig. 7.1 (A). The cell-mechanical parameter estimation via simulation-based inference (SBI) presented in Chapter 6 can support the validation of the model. SBI can determine the optimal model parameter set for each cell line assuming that the model is applicable. Should this not be the case, the model's simulations will not resemble the experimental trajectories, disproving universality.

Another, equally important approach to determine the limitations of the model, is to scrutinise its constituents. Essential for the adhesion-velocity relation of the model is the assumption that adhesion strength directly correlates with ligand density. This could be experimentally verified by measuring the density of FAs at a ligand density step or gradient, Fig. 7.1 (B). For a quantitative determination of the density of FAs, super-resolution microscopy would be advisable [287–291].

The drag factor ζ of our biophysical model mainly entails interactions of the cell with its environment via integrins. However, in contrast to the friction coefficient κ, the drag coefficient also encompasses resistive forces caused by other factors such as the medium viscosity, Fig. 7.1 (C). Pittman et al. could show that cells can use ruffles of the cell membrane to sense extracellular fluid viscosity [292]. On a microfluidic setup, it would be possible to detect morphodynamic changes of cells depending on the viscosity of the medium, which would be primarily connected to the drag coefficient in the model.

Measurements of actin retrograde flow, on the other hand, would be invaluable for experimentally confirming the κ dynamics of the model, Fig. 7.1 (D). Appropriate methods include fluorescent recovery after photobleaching (FRAP) and fluorescence speckle microscopy [176, 252, 254, 264–267]. FRAP uses photobleaching to add a mark to the fluorescently labelled actin network. Time-lapse measurements make it possible to follow the photobleached area and quantify retrograde flow. For an example of FRAP in B16-F1 mouse cells, see Fig. B.8. If the retrograde flow velocity were measured in MDA-MB-231 cells, it could be contrasted with the biophysical model predictions.

Furthermore, the biophysical model and the cell migration platform can be used to

elucidate the role of intracellular components. A worthwhile target would be the unconventional actin motor protein that is myosin VI (myo6), which studies imply to be linked to cancer progression [293–295]. Myosin VI is an actin motor that travels, unlike all other identified myosins, towards the minus end of the polarised actin filament [73]. Its functions include cargo transport during endocytosis and structural support at the Golgi complex but it is also implied in cell migration [296]. Together with the group of Claudia Veigel we started to systematically analyse the effect of myo6 KO and myo6 overexpression on cell migration, see Fig. B.9. To the naked eye, the trajectories of RPE WT display a similar behaviour to the RPE myo6 KO and the RPE myo6 GFP mutants, see Panels (A-C). This impression is supported by an analysis of the motile states for all three cell lines, see Panel (D). However, on closer inspection, the RPE myo6 KO cells show a slightly impaired migration velocity, as can be seen in Panel (E). The next steps would be to quantify the model parameters using SBI. Differences in parameter values for these cell lines would provide information about the site of action of myo6 during cell migration. The localisation of the GFP-labelled myo6 motors would complete this study.

This thesis concentrated on single-cell migration. Nonetheless, with slight modifications to the experimental setup and data analysis, it could be adapted to investigate collective cell behaviour. Interestingly, the raw data already includes cell-cell interactions, but these were purposefully excluded from the analysis. Nevertheless, there were apparent differences in the interaction of cells depending on the cell type. While MCF-10A cells displayed a tendency to form trains and follow each other similar to the behaviour reported by Vercruysse et al. [112], RPE cells showed no apparent interaction, but simply glided past each other. Due to the ubiquity of cell-cell interaction *in vivo*, an extension of our cell-mechanical model to include an interaction term would be a logical step to better understand cell migration.

To conclude, the single-cell migration analysis discussed in this thesis offers an important platform for advancing future research both horizontally, by exploring the universality of models and relations, and vertically, by achieving a deeper and more detailed comprehension of cell migration.

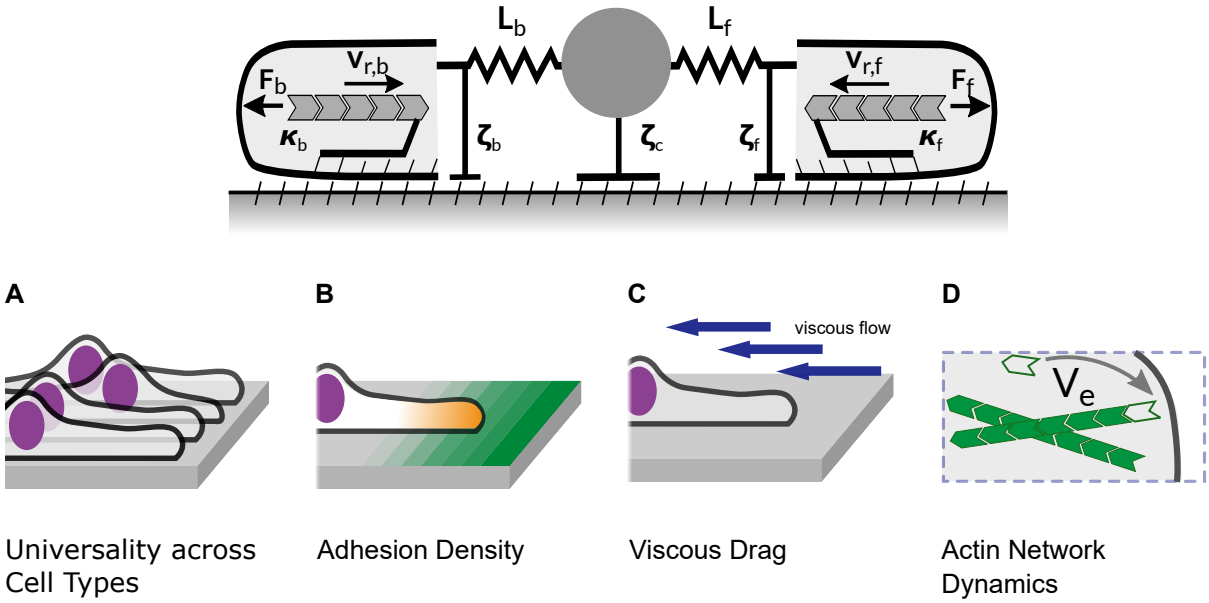

Figure 7.1: Next steps to scrutinize the biophysical model as presented in Amiri et al. (2023) [2]. **(A)** More cell lines need to be analysed to validate the universality of the model. **(B)** Quantifying the density of focal adhesions as a function of ligand density and testing the universality of the model by probing other ECM proteins would further strengthen the model. **(C)** Life at low Reynold's number means viscosity is non-negligible. Applying microfluidics to change the viscosity of the medium decouples viscous ζ drag from adhesion. **(D)**Fluorescent recovery after photobleaching, illustrated in Fig. B.8, measures actin network dynamics, playing a crucial role in confirming the κ-dynamics.

Materials and Methods

1 Micropatterning

We confined the motion of cells to one dimension through micropatterns of the extracellular matrix protein fibronectin (FN). First, we labelled the protein using a fluorescent dye that would facilitate the detection and visual quality control of the micropattern as well as allow for a quantification of the density of the patterned protein later on. Second, we fabricated the desired micropattern onto a substrate using either a micro contact technique or a photolithography technique. Third, depending on the goal of the experiment, the density of FN was determined via fluorescent calibration.

1.1 Protein Labelling

We resuspended lyophilised human FN (YO Proteins, Ronninge, Sweden) in sterile phosphate-buffered saline (PBS). Subsequently, we labelled the protein with one of two fluorescent dyes. The protein was conjugated with either Alexa Fluor 488 5-SDP ester, cat. no. A30052 or Alexa Fluor 647 NHS ester, cat. no. A20006 (Thermo Fisher Scientific, Waltham, MA, USA). After the conjugation reaction, we separated the conjugate from free dye using gel filtration chromatography. As gel filtration columns we used PD MiniTrap G-25 (GE Healthcare Bio-Sciences AB, Uppsala, Sweden) or Zeba Spin Desalting Columns, cat. no. 87768 (Thermo Fisher). We determined the concentration of the FN-solution via optical absorption at 280 nm either on a Nanodrop (Thermo Fisher) or on a Cary 60 UV-Vis spectrophotometer (Agilent, Santa Clara, CA, USA) and via a colorimetric Bradford assay. For the Bradford assay we used the Pierce Bradford Plus Protein Assay Reagent, cat. no. 23236 (Thermo Fisher) and the protein standard bovine serum albumin (BSA), CAS RN 9048-46-8 (Merck, Darmstadt, Germany).

1.2 Microcontact Printing

Imaging dishes with a polymer coverslip bottom (ibidi, Gräfelfing, Germany) were coated with fluorescently labelled FN. To achieve this, a negative mould was fabricated in our in-house clean room. The mould consists of a silicon (Si) wafer and a spin-coated

layer of either the positive photoresist AZ 40XT (Merck) or the negative photoresist SU-8 (Kayaku Advanced Materials, Westborough, MA, USA), depending on the desired dimensions of the stamp. Using a scanning UV-laser device, the ProtoLaser LDI (LPKF Laser & Electronics, Garbsen, Germany), we illuminated a positive (or negative) pattern on the positive (or negative) photoresist. After baking and curing the photoresist, the microstructured Si wafer could be used as a mould. We filled the mould with the polymer polydimethylsiloxane (PDMS) with a monomer-to-cross-linker ratio of 10:1, degassed the polymer, cured it at 50 °C for a few hours, removed it from its mould and cut it into stamps. Then the stamps underwent a UV-treatment (PSD-UV, novascan, Boone, IA, USA) for 5 min before we incubated them with a diluted solution of fluorescently labelled FN. For most measurements the concentration of the solution was in the range of 1-100 µg/ml. Subsequently we washed the coated stamps with purified water and placed them on the UV-treated coverslip bottoms of the imaging dishes with the protein coated side facing the substrate to transfer the protein. We filled the negative space between the adhesive structures of the pattern with a non-fouling poly(ethylene glycol) (PEG)-solution to block the formation of adhesion sites of cells in this area. If not specified otherwise, the micropatterns that were fabricated using the microcontact printing protocol were homogeneous lanes with a constant width of 15 µm.

Alternating fields of fibronectin densities, such as the ones described in Adhesion-Velocity Relation were produced via an extra stamping step. For the two-proteins version of the protocol, the protein of the first stamp was transferred onto a second stamp. Then, a protein solution (typically of a different concentration than the first one) was filled in-between the two stamps. The second stamp than transferred the two-protein pattern onto the substrate and the protocol continues just like in the standard version.

1.3 Photopatterning

The protocol for the photolithographic micropatterning of proteins on imaging dishes starts with the application of a non-fouling coating of the coverslip's surface that gets selectively removed at a later stage. To this end, we placed a drop of 0.01% (w/v) poly(L-lysine) (PLL) (Merck) in an ibiTreat μ-dish (ibidi) to cover the bottom's negatively charged surface and let it incubate for 30 min at room temperature. Afterwards we thoroughly rinsed the dish with 2-[4-(2-Hydroxyethyl)piperazin-1-yl]ethane-1-sulfonic acid (HEPES) buffer (pH=8.3) (Thermo Fisher) to remove excess PLL. Subsequently, we diluted PEG-SVA (Laysan Bio, Arab, AL, USA) in HEPES buffer to a concentration of 100 µg/ml and applied it to the surface. SVA is the ester that forms amide bonds between PLL and PEG, effectively creating a non-fouling coating. Afterwards we rinsed the dish thoroughly with purified water.

We diluted the photo-activator PLPP (Alvéole, Paris, France) in 99% ethanol so that the PLPP gel could spread homogeneously on the surface of the dish. Next, the desired micropattern was loaded onto the illumination device, which was a Primo 2 module (Alvéole) mounted on an Eclipse Ti microscope (Nikon, Tokyo, Japan) and operated by the dedicated Leonardo software (Alvéole). After a calibration step we brought the PLPP

layer of the μ-dish into the focus of the UV-LED of the Primo device. Then, the device shined the pattern motif onto the μ-dish using its digital micromirror device (DMD). Most patterns had multiple repetitions of the motif resulting in the total dimensions of the pattern being much bigger than the dimensions of a single DMD field. To be able to cover such large areas the Leonardo software controlled the stage of the inverted microscope to move the dish and illuminate the surface one field of DMD after another. For motifs of a pattern that were larger than a single DMD we illuminated neighbouring fields in an overlapping manner with gradients of light doses complementing each other in such a manner that the resulting dose of the overlap would be exactly the same as in the centre of the DMD field. The energy density of the UV beam could be tuned depending on the desired protein density of the pattern. For most measurements we set it to 15 mJ/mm^2. After we had washed the μ-dish thoroughly with purified water, we rehydrated the coating with PBS for 5 min before we incubated the surface with a solution of fluorescently labelled FN. After a thorough wash we incubated the pattern with PBS and stored the dishes at 7 °C until we seeded cells on them.

1.4 Determination of Fibronectin Density

We determined the density of FN proteins of the micropatterns via the intensity of their fluorescent signal. We were able to do this by comparing the fluorescence intensity of the pattern to that of a solution of FN of known concentration in a microfluidic channel of known height. The microfluidic calibration slide was prepared in-house. The calibration slide consists of a PDMS block with 5 channels of a defined height of 20 µm and inlets on one side and outlets on the other side. The PDMS block was cast in a mould of cured photoresist on a Si wafer and cured at 50 °C for a few hours. Afterwards we cut out the PDMS block and bonded it onto a plasma treated glass slide. We filled the channels with a dilution series of labelled FN and measured the intensity of the fluorescent signal on the same microscopy setup and the same settings as for the cell migration experiments. By fitting the intensity/concentration data with a linear function we obtained a calibration factor that allowed to convert from fluorescence intensity to protein density.

2 Cell Lines and Cell Culture

The **MDA-MB-231 H2B-mCherry** and **MDA-MB-231 H2B-mCherry Lifeact GFP** cells (gifts from Timo Betz, WWU Münster, Germany, now moved to Georg-August-University Göttingen, Germany) were cultured in Leibovitz L-15 medium with 2 mM Glutamax (Thermo Fisher) plus 10% fetal bovine serum (FBS) (Thermo Fisher) at 37 °C. The phosphate buffered L-15 medium doesn't require CO_2 equilibration. Cells were passaged every 2-3 days using the cell detachment solution Accutase (Thermo Fisher). For experiments we centrifuged the cell solution at 800 rcf for 3 min and resuspended the cells in medium. We seeded about 5000 cells per dish. After 2–3 h, cells adhered to the micropatterns and we exchanged the medium to L-15 medium without the pH indicator phenol red. We then

transferred the samples to the microscope and started measurements within 1–2 h.

The **MCF-10A** cells (ATCC, Manassas, VA, USA) were cultured at 5% CO_2 at 37 °C in DMEM/F-12 medium including Glutamax (Thermo Fisher) supplemented with 5% horse serum (Merck), 20 ng/ml human epidermal growth factor (Merck), 100 ng/ml cholera toxin (Merck), 10 µg/ml insulin (Merck) and 500 ng/ml hydrocortisone (Merck). For passaging we treated cells with Accutase for 15 min. For experiments we centrifuged at 500 rcf the cell solution for 6 min and resuspended the cells in growth medium. We seeded about 5000 cells per dish. After 2–3 h, cells adhered to the micropatterns and we exchanged the medium to growth medium containing the nuclear stain 25nM Hoechst 33342 (invitrogen, Waltham, MA, USA). We then transferred the samples to the microscope and started measurements within 1–2 h.

The hTERT RPE-1 CRL-4000^{TM} cells, which in the following we refer to as **RPE (WT)** (ATCC) and **RPE MYO6 KO** (KO achieved through CRISPR-Cas9 by Folma Buss, University of Cambridge, Cambridge, UK and kindly provided by Claudia Veigel, LMU, Munich Germany) cells were cultured in DMEM/F-12 medium including Glutamax (Thermo Fisher) supplemented with 10% FBS (Thermo Fisher) at 5% CO_2 at 37 °C. Cells were passaged every 2-3 days using Accutase (Thermo Fisher). For experiments we centrifuged the cell solution at 800 rcf for 3 min and resuspended the cells in medium. We seeded about 5000 cells per dish. After 2-3 h, cells adhered to the micropatterns and we exchanged the medium to growth medium containing the nuclear stain Hoechst 33342 at a concentration of 25 nM. We then transferred the samples to the microscope and started measurements within 1-2 h.

The **RPE MYO6 GFP** (stabily transfected by Folma Buss and kindly provided by Claudia Veigel) cells were cultured the same way as the RPE WT cells except for the fact that the growth medium was additionally supplemented by 500 µg/ml G418-sulfate (Geniticin, Thermo Fisher), an aminoglycoside antibiotic. Other then that the handling was exactly the same.

3 Transfection Procedure

For transfection experiments on RPE MYO6 KO cells we used Lipofectamine 3000^{TM}, cat. no. L3000001 (Thermo Fisher), to introduce DNAs that encode for three different mutations of the myosin VI gene. We split 800-1000k cells into a 6-well-plate and cultured them until they reached roughly 80% confluency as estimated by visual inspection. We diluted 3.7 µL of the Lipofectamine 3000 reagent in 125 µL of Opti-MEM medium (Thermo Fisher) and 1.5 µg of DNA for WT-MYO6 (concentration at 1147 ng/µL), MYO6 S267A (762 ng/µL) or MYO6 S267E (1374 ng/µL) (Maxiprep, Thermo Fisher) likewise in 125 µL of Opti-MEM. We then added 3 µL of the amplifier reagent P3000 (concentration at 2 µL/µg) to the diluted DNA and subsequently mixed it with the diluted Lipofectamine in a 1:1 ratio. Afterwards, we let it incubate for 15 min to form lipoplexes. Finally we added the DNA-lipid complexes to the cells and incubated everything for 24 h at 37 °C.

4 Cytoskeletal Inhibitors

For inhibitor experiments we added 10 µM **(+/-)-blebbistatin** (Cayman Chemical, Ann Arbor, MI, USA), 100 nM **latrunculin A** (Merck), 0.25 nM **calyculin A** (Thermo Fisher), or 30uM **Y-27632** (Merck) to the growth medium 2 h before the start of the experiment. As control we used 0.3% **dimethyl sulfoxide (DMSO)** (Life Technologies, Darmstadt, Germany) in growth medium.

5 Immunostaining

We fixed cells with 3.7% formaldehyde (Merck) in PBS after the time-lapse experiments and permeabilised with 0.5% triton X-100 (Carl Roth, Karlsruhe, Germany). We inhibited unspecific binding with a blocking solution consisting of 3.9% BSA (Thermo-Fisher) and 0.2% triton X-100. We then incubated the cells with a monoclonal mouse anti-paxillin antibody (invitrogen) at a concentration of 5 µg/ml over night. After washing with PBS we used 5 µg/ml goat anti-mouse antibodies conjugated with Alexa Fluor 488 (Abcam, Cambridge, UK) as secondary antibodies. F-actin was labelled with 100 nM rhodamine phalloidin (Abcam) in a blocking solution consisting of 10% normal goat serum in PBS. Lastly, we washed the sample three times with PBS.

6 Microscopy

We conducted time-lapse imaging using an inverted fluorescence microscope (Nikon Eclipse Ti, Nikon, Tokyo, Japan) that featured an XY-motorised stage, Perfect Focus System (Nikon), and a heating chamber (Okolab, Pozzuoli, Italy) set to 37 °C. The motorised stage, Perfect Focus System, a 10x CFI Plan Fluor DL objective (Nikon), a CMOS camera (PCO edge 4.2, Excelitas PCO, Kelheim, Germany), and NIS Elements software (Nikon) were employed to sequentially scan and capture images of arrays of fields of view. Prior to initiating the time-lapse process, epifluorescence images of the FN patterns were acquired. Subsequently, phase contrast images of the cells and epifluorescence images of their nuclei were recorded over a 48 h period at intervals of 10 min or 30 s as specified. A 10 min interval permitted scanning of approximately 17 x 17 = 289 fields of view, while a 30 s interval allowed for 4 x 4 = 16 fields of view.

7 Image and Data Analysis

Image analysis for Chapters 4 and 5 was conducted using a combination of scripts for MATLAB R2020a (MathWorks, Natick, MA, USA) and macros for FIJI (ImageJ). FN lanes were detected through a Hough transformation applied to the fluorescence

signal of labelled FN. Nuclei positions were tracked by using a threshold set post background correction and band-pass filtering on the fluorescent images. The x-coordinates of the nuclei were adjusted to align parallel with the FN lanes. Cell front and back positions were determined using kymographs created along the FN lane centre, followed by manual segmentation of the cell edges. The code is available on GitHub at behnam89amiri/Multistability_and_constitutive_relations_of_cell_motion.

For Chapter 6 the image analysis was conduced using Python (Python Software Foundation) code. Lanes were again detected by a Hough transformation of the fluorescence signal of the labelled FN. However, the cells were segmented using cellpose and the fluorescently labelled nuclei were tracked using trackpy. Cellpose is a generalist algorithm for cell and nucleus segmentation that we trained on our data [226, 227] and trackpy is a Python package for particle tracking in 2D [297]. The cell trajectories were filtered to only include cells that are on a FN lane, not too close to the edge of the field of view, not too close to another cell and contain only one nucleus [218]. The code is available on GitHub miguelatienza/onedcelltrack.

The experimental metadata was organised in compliance with the Minimum Information About Cell Migration Experiments (MIACME) reporting guidelines, which can be found at http://cmso.science/MIACME. The data was entered into a SQLite database file using DB Browser for SQLite. An SQL-version of my data base containing the name, date and meta data of all experiments used for this thesis and many more can be found on my GitLab repository.

8 Classification of Motile States

A reliable and scalable high-throughput analysis of the motile states of single cells requires an automated classification of states. To this end we introduced a minimal time of consistency t_c. Should the motile behaviour during a period $t + t_c$ be indicative of a specific state, we assigned that state to the cell. We selected a duration of 1 h for this period, which is adequately longer than the usual oscillation periods of approximately 15 min and allows us to differentiate between steady and oscillatory states. Identifying transitions necessitates continuous tracks lasting at least $2t_c$ to distinguish between the pre- and post-transition states.

The single-cell trajectories are divided into distinct states. To achieve this, we utilised a technique that involves iterative change-point analysis based on cumulative sum (CUSUM) statistics, akin to the approach in [144], to identify the transition moments between a cell's states. This algorithm is proficient at pinpointing the times when a significant shift in motility pattern occurs. The interval between consecutive change points is considered an episode where the cell maintains a particular state. Episodes shorter than 1 h are merged with the preceding episode.

To classify the episodes into the motile states SS, SO, MS and MO, we established two metrics. First, we assessed whether a cell is moving (MS, MO) or spread (SS, SO) by comparing its average velocity during the episode with a critical speed ($0.002\,\mu m\,s^{-1}$).

Cells are regarded as spread if their average velocity is below this critical speed and as moving if it is above. However, the positional data $\mathbf{X}(t)$ has to be filtered to remove short-term fluctuations and long trends. To this end, we applied a band-pass filter with a cut-off frequency of $1\,\mathrm{h}^{-1}$ and $6\,\mathrm{h}^{-1}$ to discard variations on time scales shorter than 10 min and longer than 1 h.

This filtered data includes the fluctuations in length and position of the cell body over time, which are pertinent to the oscillations resulting from the competition of protrusions. In an oscillatory state, these filtered variables exhibit significant variability, whereas they remain nearly unchanged over time in a steady state. Therefore, summing the average absolute deviations of the filtered length and cell body position serves as a measure of oscillatory magnitude:

$$O = \frac{1}{n} \sum_{i=1}^{n} \left(|L_{f,i}| + |X_{f,i}| \right) \tag{A.1}$$

O represents the oscillation metric, while n denotes the number of time frames for the state. Here, $L_{f,i}$ refers to the length subjected to band-pass filtering, and $X_{f,i}$ indicates the cell body position in the time frame i. We subsequently assessed this oscillation metric for each cell episode against a critical threshold of 5 µm. Through manual evaluation of the cell episodes and their corresponding oscillation metric values, we determined that this threshold effectively classifies the cell states.

For a further discussion of the motility metrics, see Amiri, Heyn, et al. (2023), Supplementary Information [2].

9 Neural Density Estimator

Simulations of the biomechanical model referred to in the chapter Cell-mechanical Parameter Estimation were implemented in Python [298] and Julia [299] by M. Atienza Juanatey and are available from his GitHub repository miguelatienza/onedcellsim. The open-source Python package “sbi”, created by Tejero-Cantero et al. from the Macke lab [210], is employed to deduce the posterior distribution of model parameters of individual cells based on their one-dimensional trajectories. Our neural network designed for density estimation consists of two principal parts. Initially, the input, which is a cell trajectory, undergoes dimensionality reduction and feature extraction through an embedding by a convolutional neural network (CNN). Subsequently, the resulting features from the CNN are processed by a neural spline flow network. Notably, the initial layer of the CNN was altered from a one-dimensional to a two-dimensional structure, enhancing the ability to capture the interconnections among the three time series (front, back, nucleus) that form a single trajectory, thereby preserving relationships between the cell’s positions more effectively.

10 Use of AI Assistance in Writing

In the process of writing this thesis, I utilised the assistance of large language models (LLM's), mainly but not exclusively OpenAI's ChatGPT and Digital Science's Writefull, to aid in the generation of text. ChatGPT was employed to help clarify complex concepts and refine language for certain sections of the thesis. The content produced by the LLM was critically evaluated, revised, and supplemented by my own knowledge, ensuring that the final work reflects my original research and understanding. All instances of AI-assisted text generation were limited to non-technical language and editorial suggestions, without compromising the integrity of the original analysis, data interpretation, or conclusions. The use of such tools was intended to enhance the clarity and precision of the writing, not to contribute to the intellectual content of the research itself.

Supplementary Information

1 Standardised High-Throughput Experiments

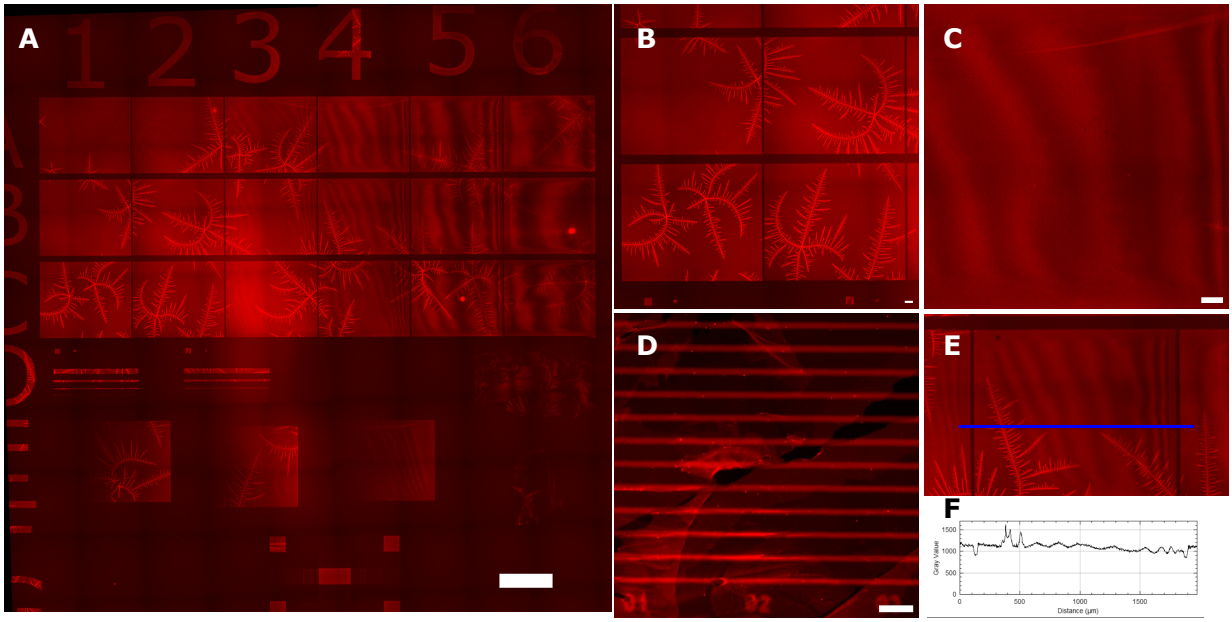

Figure B.1: Examples of possible pitfalls for the Primo photopatterning protocol. Micrographs of fibronectin (FN) micropatterns that were labelled with the fluorescent dye Alexa 647. **(A)** The overview scan reveals a selection of diverse micropattern motifs that were applied to a microwell in a single patterning session using the Primo by Alvéole. The micrographs in **(B-D)** are zoom-ins of panel (A). They reveal various imperfections in the pattern. **(B)** Crystalline structures occur if the passivation layer was not freshly prepared. **(C)** A wave like pattern in FN densities appears if the photoactive gel is unevenly spread which leads to inhomogeneous photoactivation during illumination. **(D)** If the FN is not washed off thoroughly, it leaves irregular patches on an otherwise successfully patterned area. **(E,F)** The fluorescence intensity plot (F) along the 2000 µm long blue lane (E) quantitively captures imperfections in the pattern. Crystalline structures, as shown in Panel (B), appear as pronounced peaks while wave like inhomogeneities such as in (C) appear as undulations. The scale bar in (A) is 1000 µm and 100 um in (B-D).

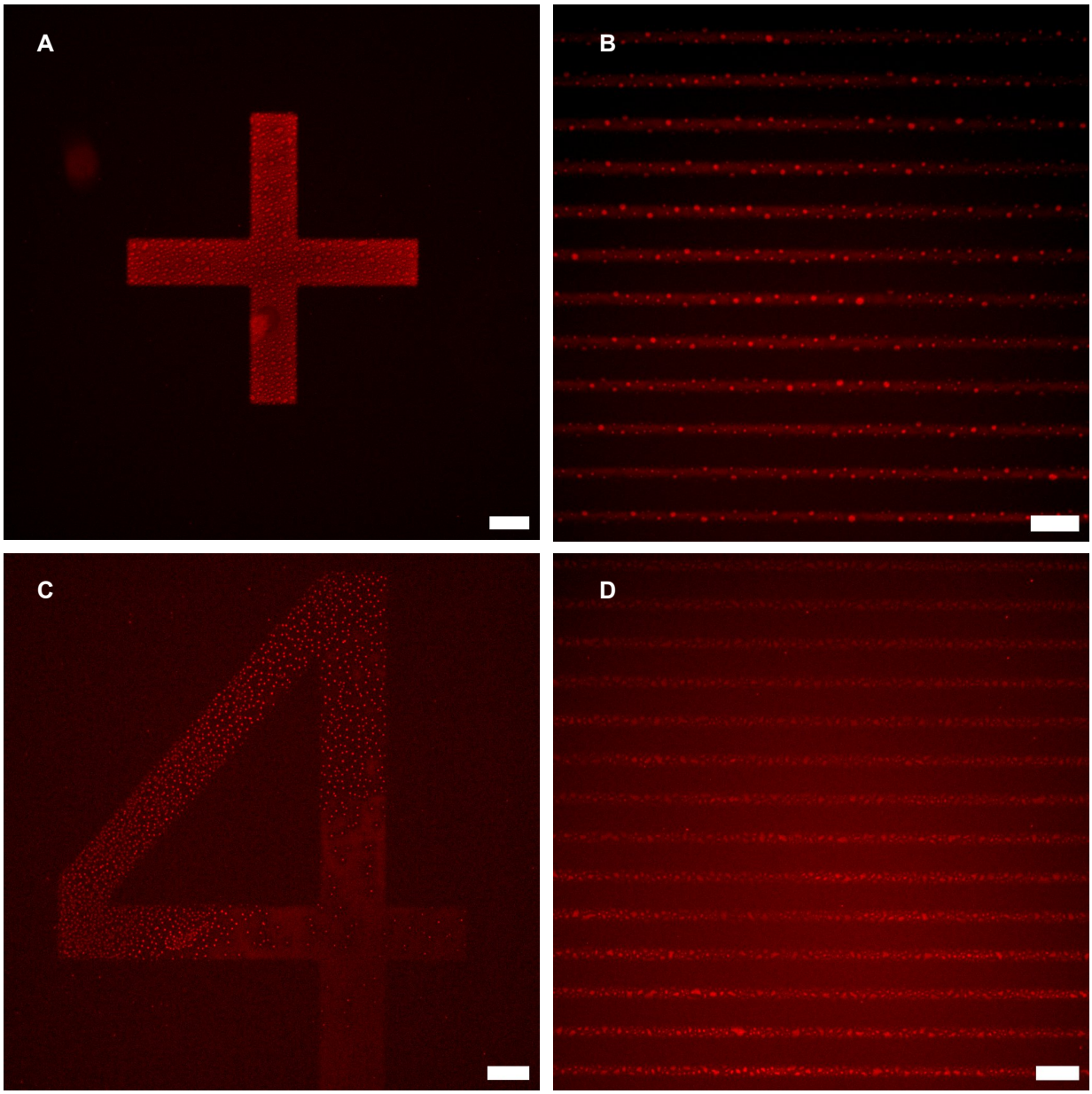

Figure B.2: Impurities in photopatterning. Small, almost monodisperse structures with a diameter of a few micrometres often appear on patterns. The structures are high density accumulations of FN. They can appear as small circular dots **(A-C)** or as patchy speckles **(D)**. The origin of these structures is not quite clear yet but it has its cause probably in the dissolution of the PEG in solvent which may contain small air bubbles after mixing. Scale bars 100 µm

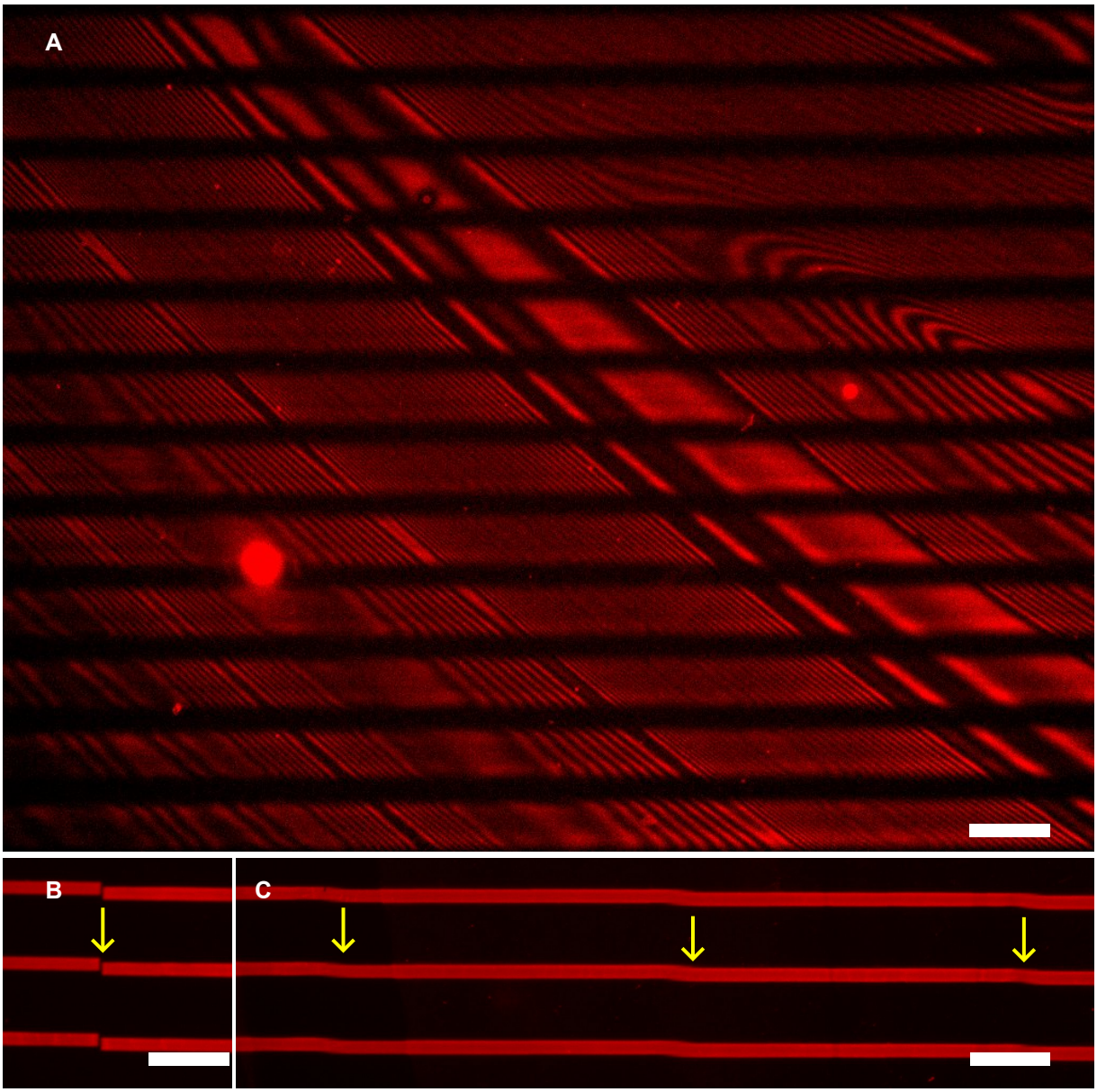

Figure B.3: Alignment issues during photopatterning. Micrographs of fibronectin (FN) micropatterns that were labelled with the fluorescent dye Alexa 647. **(A)** The photactivator is applied in an ethanol solution. The ethanol evaporates and ideally leaves a homogenous layer of photoactivator. This evaporation process, however, depends on experimental conditions such as temperature and humidity which are not always kept constant during preparation. As a consequence, the photoactive layer may vary in thickness, which causes iridescent effects during illumination similar to the colourful patterns on a soup film. Additionally, the UV-laser was not correctly focused in this example, leading to very broad lanes, much wider than the 15 µm target width. **(B)** If the photopatterning device Primo is not well aligned, stitching of the pattern's motif can go awry. A gap is visible between the lane motif in this example. **(C)** Depending on the magnification chosen for the photopatterning, the digital micromirror device (DMD) can be smaller than the actual motif. In the example here, created with a 20x magnification, there is a visible offset along the lanes, where the Primo device moved the stage to illuminate the next DMD of the same motif. Scale bars in (A-C) equal 100 µm.

2 Intrinsic Cell-to-Cell Variance

As Fig. B.4 shows, the parameters of individual moving objects can be described by Gaussian distributions. Furthermore, both systems, i.e. the polystyrene beads in water as well as the cells in confinement are stationary and do not depend on time. As a consequence, the generalised Langevin equation (4.1) can be inverted to extract the memory kernel from the velocity autocorrelation function. For details, see SI of A. Klimek et al. 2024 [5].

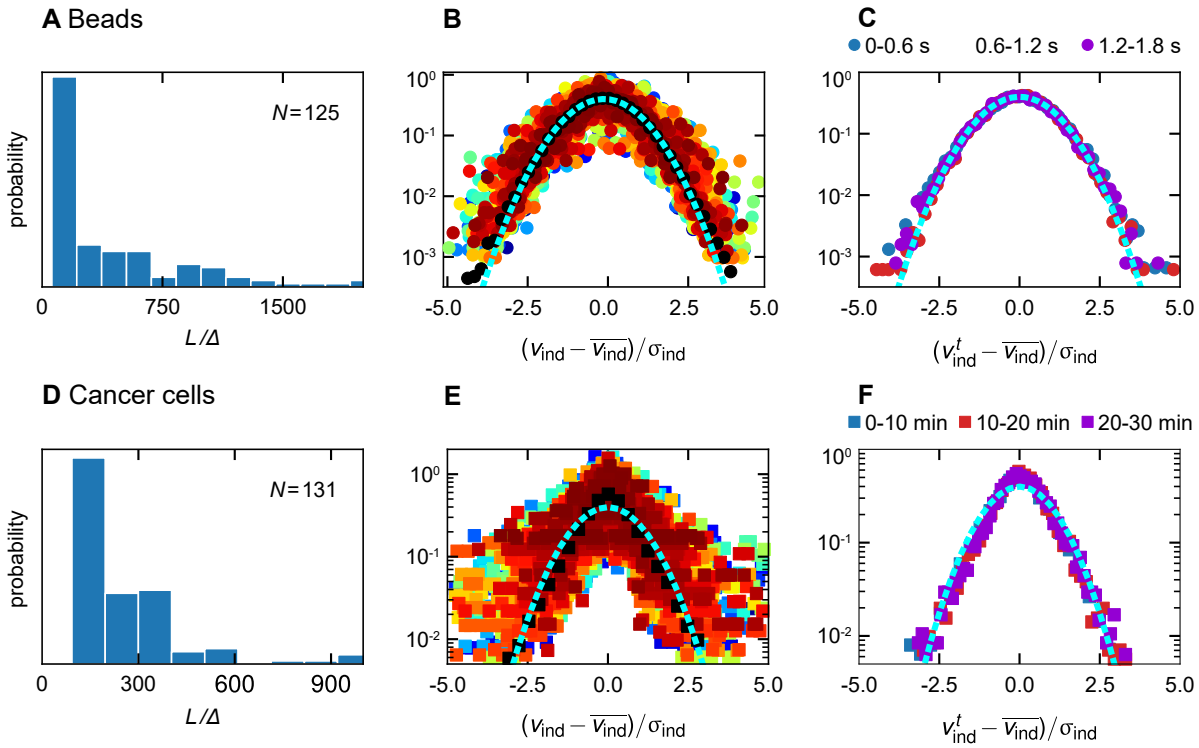

Figure B.4: Assumptions check for the extraction of memory kernels for the polystyrene beads and cancer cells. The first column displays the distributions of trajectory lengths L in units of the experimental discretisation time Δ for **(A)** beads with $\Delta = 0.02\,\mathrm{s}$ and **(D)** breast-cancer cells with $\Delta = 20\,\mathrm{s}$. Simulations were later sampled to follow the same distribution. The second column shows the velocity distributions of individual moving objects. The values have been rescaled by subtracting their *individual* mean velocity $\langle v_{\mathrm{ind}} \rangle$ and dividing by their *individual* standard deviation σ_{ind} for **(B)** polystyrene beads ($\langle \sigma_{\mathrm{inds}} \rangle = 4.6\,\mu\mathrm{m/s}$) and **(E)** breast-cancer cells ($\langle \sigma_{\mathrm{inds}} \rangle = 1.3\,\mu\mathrm{m/s}$. Individual objects are distinguished by colour. The population average is shown in black. It is in good agreement with the standard normal distribution as shown as a bright blue dashed line. For three different time windows, the average over individually rescaled distributions is identical for **(C)** polystyrene beads and **(F)** breast-cancer cells, which suggests the systems not to be time-dependent. Adapted from Klimek, Heyn et al. 2024 [5].

3 Biophysical Modelling

Name of data set	Temporal resolution	Treatment	Number of trajectories	Total time
1_ctrl_30s	30 s	control	221	2878 h
2_lat_30s	30 s	latrunculin A	127	2343 h
3_blebb_30s	30 s	blebbistatin	65	1165 h
4_ctrl_10min	10 min	control	9497	96577 h
5_lat_10min	10 min	latrunculin A	3368	54809 h
6_blebb_10min	10 min	blebbistatin	3728	47638 h
7_untreated_10min	10 min	untreated	6261	65378 h

Table B.1: Details of experimental data sets used for Chapter 5 including temporal resolution, treatment, number of cell tracks, and total trajectory time. See also Fig. B.5. The data was published alongside the journal article [2].

All simulations were executed using MATLAB (Mathworks). We conducted simulations of around 6100 cell tracks, each lasting 15 h. This includes 2500 for the control, 2800 for the latrunculin, and 800 for the blebbistatin conditions. Simulations begin with cells in random states. Fibronectin densities on lanes are uniform across all simulations. The experimental data sets include a variety of Fibronectin densities, and the simulations mirrored these values. Analysis involved averaging across Fibronectin densities, with simulation ensembles weighted identically to the experiments.

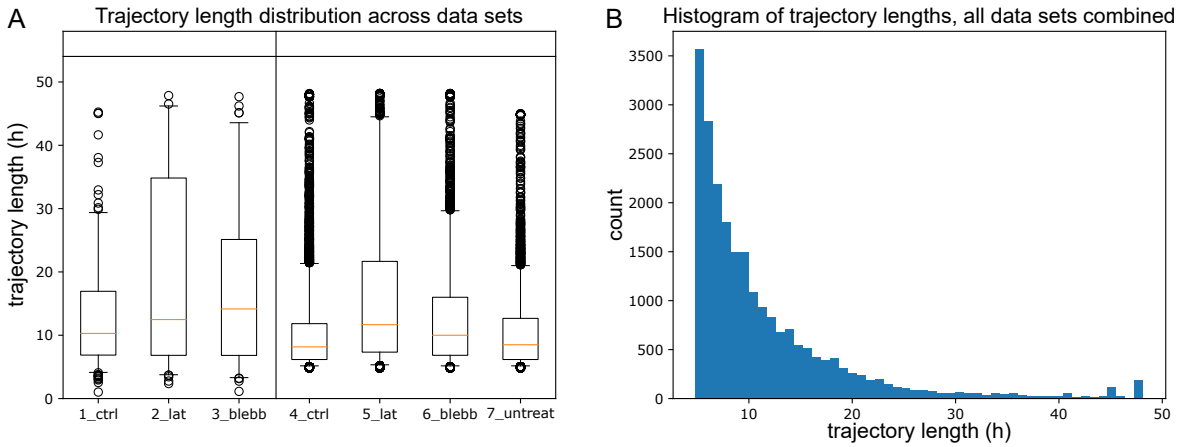

Figure B.5: Distribution of lengths of cell trajectories for Chapter 5. **(A)** Boxplots for data sets 1-7 are displayed (refer to Amiri et al. [2]). The orange lines represent the median track lengths, while the box edges correspond to the first and third quartiles. Whiskers show the 5%- and 95%-percentiles. The symbol N refers to the total number of cell trajectories. Overall, the average trajectory length is 11.6 h. Notably, the distribution is right-skewed, as evidenced by a median trajectory length of 8.8 h, indicating a higher number of trajectories are shorter than the average. The longest trajectory lasts 48 h due to the fixed duration of the experiments. **(B)** A histogram for the trajectory lengths of all combined data sets is shown. The skewness observed earlier is evident, with counts tapering off as trajectory lengths increase. Adapted from B. Amiri, J. Heyn et al. 2023 [2].

Parameter	Set 1: control	Set 2: latrunculin	Set 3: blebbistatin	Units
E	3x10-3	3x10-3	3x10-3	$\mathrm{nN\,\mu m^{-2}}$
L_0	10	10	10	µm
V_e^0	3x10-2	2.2x10-2	3x10-2	$\mathrm{\mu m\,s^{-1}}$
k^-	5x10-3	5x10-3	5x10-3	$\mathrm{\mu m\,s^{-1}}$
k_on	1.5x10-4	1.5x10-4	1.5x10-4	$\mathrm{s^{-1}}$
k_off	7.5x10-5	7.5x10-5	7.5x10-5	$\mathrm{s^{-1}}$
v_slip	7.8x10-3	7.8x10-3	7.8x10-3	$\mathrm{\mu m\,s^{-1}}$
κ^max	35	35	20	$\mathrm{nN\,s\,\mu m^{-2}}$
K_κ	35	35	35	$\mathrm{ng\,cm^{-2}}$
n_κ	3	3	3	
κ_0	1x10-2	1x10-2	1x10-2	$\mathrm{nN\,s\,\mu m^{-2}}$
ζ^max	1.4	1.4	1.2	$\mathrm{nN\,s\,\mu m^{-2}}$
K_ζ	50	50	50	$\mathrm{ng\,cm^{-2}}$
n_ζ	4	4	4	
b	3	3	3	
ζ_0	1x10-1	1x10-1	1x10-1	$\mathrm{nN\,s\,\mu m^{-2}}$
α	4x10-2	4x10-2	4x10-2	$\mathrm{nN^{-2}\,s^{-2}\,\mu m^4}$

Table B.2: The parameters used in the simulations are specified as follows: Set 1 applies to the control condition, Set 2 to the latrunculin condition, and Set 3 to the blebbistatin condition. All simulations employing parameter sets 1, 2, and 3 are conducted on homogeneous Fibronectin lanes.

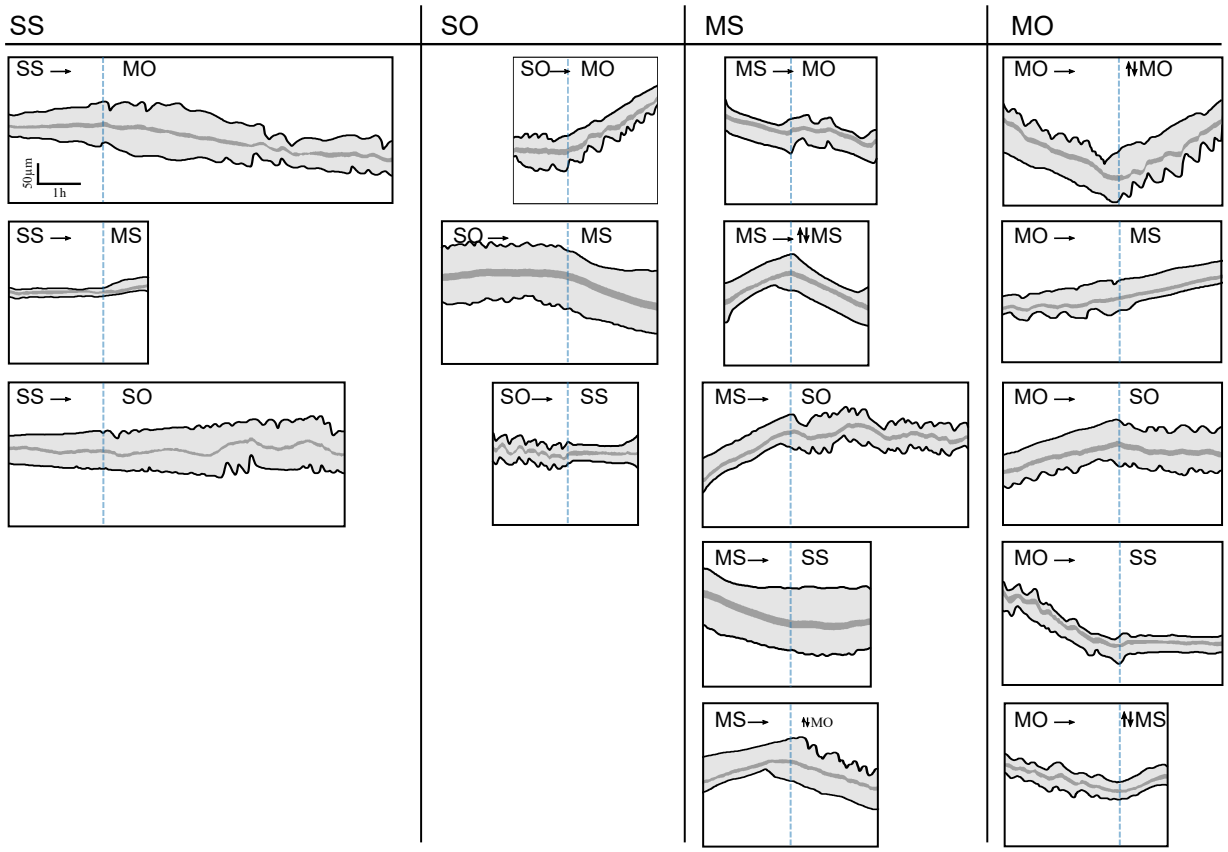

Figure B.6: Complete table of motile state transitions observed in the breast cancer cell line MDA-MB-231. Cells on 1D fibronectin coated lanes were segmented and the cell front, back and nucleus were tracked. The cell trajectories were split into episodes of motile states and each episode was ascribed one of the four motile states: spread and steady length (SS), spread and oscillatory length (SO), motile and steady length (MS), motile and oscillatory length (MO). This figure shows all possible transitions from one motile state to another. Time runs from left to right, the y-axis is the position along the lane. All panels are to scale.

4 Cell-Mechanical Parameter Estimation

Simplification of the Biomechanical Model

To achieve a meaningful parameter inference the size of the latent space of the original model as described in Amiri et al. [2] needed a reduction. We assumed the fibronectin density B as external parameter to be constant because all measurements that were analysed for the chapter Cell-mechanical Parameter Estimation were conducted on 1D lanes of the same fibronectin density. The force-dependence for the actin network extension rate V_e, as well as the depolymerisation rate k^- in Eq. 5.13 are negligible and we therefore set $V_e = V_e^0$. Rescaling of the model proved that essentially 5 parameters are necessary to cover the system's dynamics. The choice of the 5 targets of the SBI procedure was based on interpretability. The resulting parameters are: $L_0, V_e^0, k_{on}, \kappa_{max}$ and v_{slip}, see Table B.3.

Parameter name	Description	Lower bound	Upper bound	Status	Units
L_0	Resting protrusion length	1	40	variable	µm
V_e^0	Actin network extension rate	10^{-3}	$8 * 10^{-2}$	variable	µm/s
k_{on}	On-rate for dynamics integrin signalling	10^{-5}	10^{-3}	variable	1/s
v_{slip}	Critical retrograde flow velocity	$5 * 10^{-3}$	$4 * 10^{-2}$	variable	µm/s
κ_{max}	Maximum friction coefficient for integrin signalling	1	70	variable	nN s µm^{-2}
ζ_{max}	Maximum drag coefficient	1.4	1.4	fixed	nN s µm^{-2}
E	Effective E-modulus	$3 * 10^{-3}$	$3 * 10^{-3}$	fixed	nN µm^{-2}
k_{off}	Off-rate for dynamic integrin signalling	0.5	0.5	fixed	1/s
$b = \zeta_c/\zeta_f$	Contribution of the cell body to the cell drag compared to the protrusions	3	3	fixed	-
B	Fibronectin density	30	30	fixed	ng cm^{-2}
ϵ	Noise in the κ-dynamics	1	1	fixed	-
ϵ_{ext}	Localisation noise	0.5	2	latent	µm

Table B.3: Table of all 10 parameters and the two noise amplitudes that enter the biomechanical model as prior $p(\theta)$ in chapter 6. The 5 variable parameters are the target of the inference procedure, while all other parameters are fixed to a constant value.

Quality of the Neural Density Estimator

To ensure the quality of the neural density estimator, we did not only check the accuracy of its estimations, see Figs. 6.1 and 6.2 but also its calibration. To this end we followed

the simulation-based calibration approach as proposed by Talts et al. [300]. The algorithm to determine the quality of the calibration can be summarised in four steps:

1. N simulations are generated
2. L samples are sampled from the posterior $\theta_1, ..., \theta_\mathrm{L} \approx p(\theta \mid \mathbf{x})$
3. The rank statistics for $\theta_1, ..., \theta_\mathrm{L}$ are computed for each simulation (for more details see Talts et al. [300])
4. The histogram for all N simulations is incremented

If the neural density estimator is well calibrated, the rank statistics for the N_sim simulations is uniformly distributed. If the rank statistics deviate from a uniform distribution the posterior is uncalibrated and, depending on its shape, might be biased towards shifted posterior estimates or it might be over- or underconfident. The rank statistics for our neural density estimator is shown in figure B.7 for 1,000 simulations. Overall the rank statistics for the prior estimations are symmetric and fall within the expected distribution (marked in grey). Consequently, we conclude the neural density estimator to be well calibrated with only L_0 being slightly under-confident, which will result in broader inferred distributions compared to the actual posterior distributions.

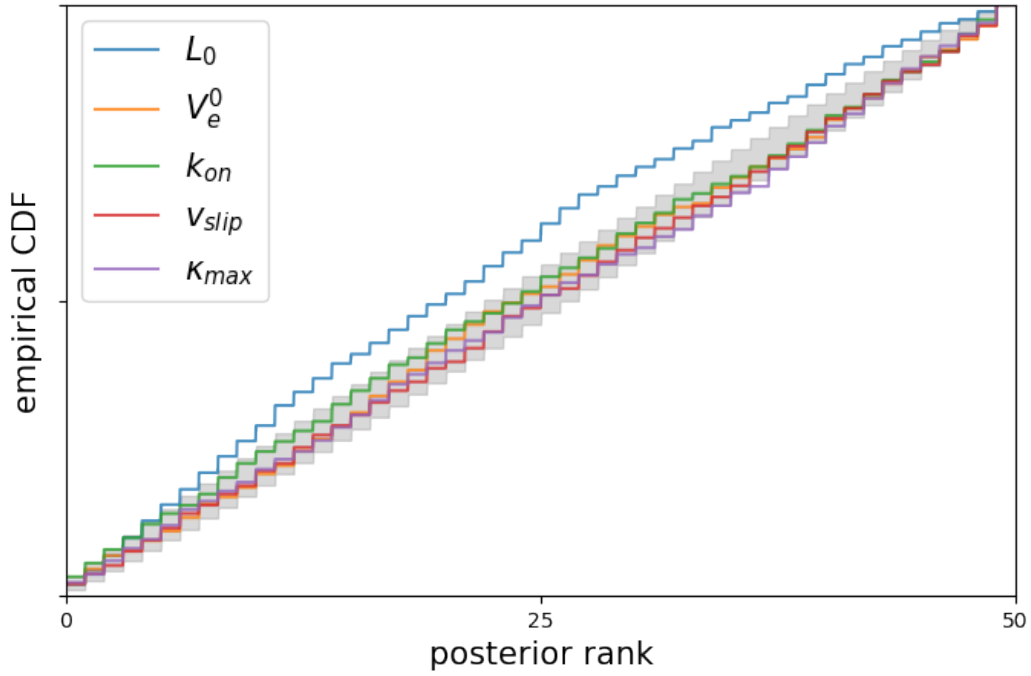

Figure B.7: The rank statistics of 1,000 simulations indicates the quality of the neural density estimator. If the rank statistics are uniformly distributed and unbiased, they fall within the grey area along the diagnoal. According to this criterion, the posterior estimation for the parameters V_e^0, k_{on}, v_{slip} and κ_{max} are well calibrated but L_0 is a little under-confident. We prefer under-confindent estimations over over-confident estimations to avoid unreliable inference results [211]. Adapted from Heyn et al. [4].

5 Conclusion and Outlook

Fluorescent recovery after photobleaching (FRAP) measurements can quantify the actin retrograde flow in the lamellipodium and the lamellar region. The measured retrograde flow velocity can then be compared to predictions of the biophysical model by Amiri et al. 2023 [2]. Fig. B.8 shows an example FRAP measurement on a B16-F1 mouse cell on a 2D substrate. This measurement was made possible by Prof. Dr. Klemens Rottner, TU Braunschweig & Helmholtz-Zentrum für Infektionsforschung. Similar experiments with MDA-MB-231 or MCF-10A cells are worthwhile propositions.

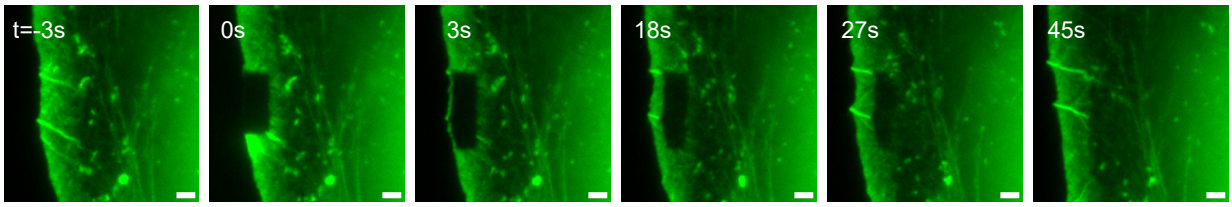

Figure B.8: Time series of micrographs showing GFP-labelled actin in B16-F1 mouse cell during fluorescent recovery after photobleaching (FRAP). Shown is the lamellipodium and the lamellar region of the cell. At time $t = 0\,\mathrm{s}$ (second panel) a powerful laser illuminates a rectangular region which bleaches all fluorescent proteins within. Due to the actin retrograde flow, the dark rectangular region moves inwards. Scale bars represent 10 µm. FRAP measurements like these can be used to scrutinise the biophysical model presented by Amiri et al. (2023) [2].

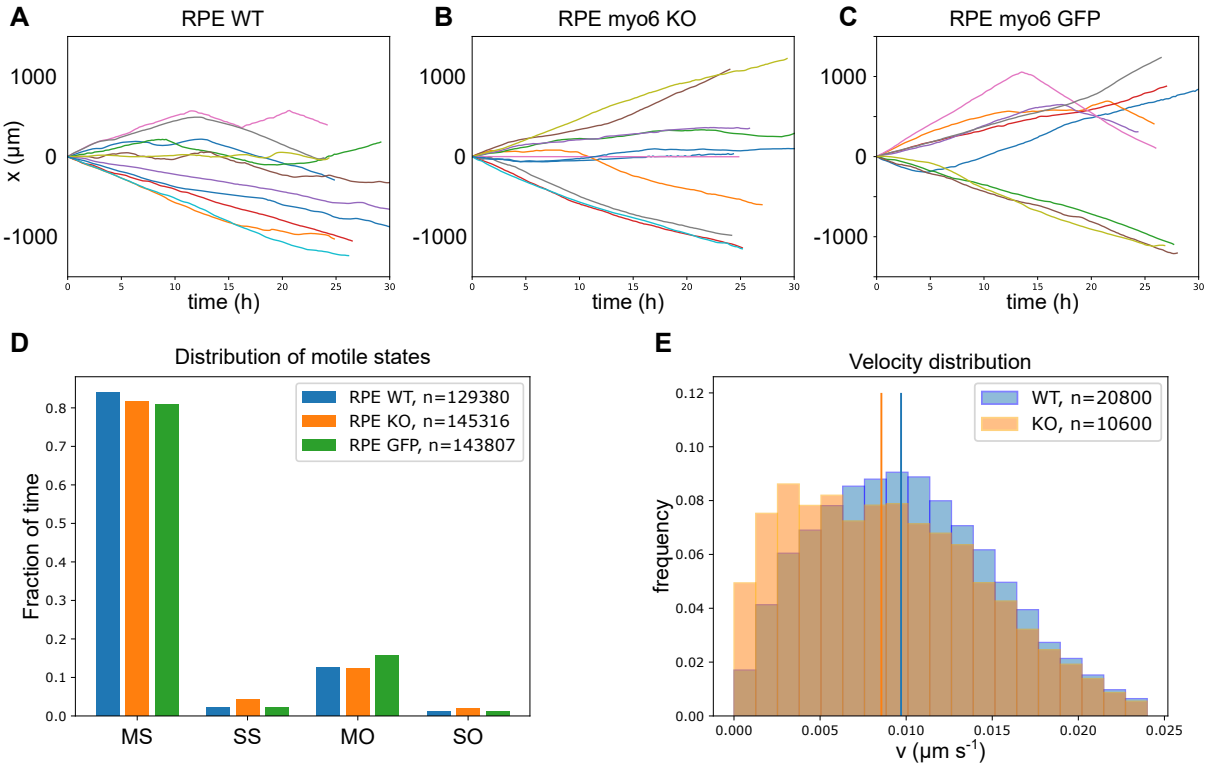

Figure B.9: The effect of a knock out (KO) and overexpression of the motor protein Myosin VI on cell migration. **(A-C)** Trajectories of RPE WT and the two mutants RPE myo6 KO and RPE myo6 GFP (overexpression). **(D)** Distribution of motile states. No significant differences could be observed. **(E)** Velocity distribution of RPE WT and RPE myo6 KO cells. The median velocity of KO cells is slightly reduced.

List of Abbreviations

1D one-dimensional. xi, 2, 5, 11, 12, 23, 27, 31, 33, 34, 43–45, 47, 50, 61–64, 77

2D two-dimensional. 2, 6, 9, 14

3D three-dimensional. 9, 14

AFM atomic force microscopy. 39

ATP Adenosine triphosphate. 7

BSA bovine serum albumin. 81, 85

CAS RN Chemical Abstracts Service Registry Number. 81

cat. no. catalog number. 81, 84

CMSO Cell Migration Standardisation Organisation. 30, 31

CNN convolutional neural network. 21, 22, 87

DMD digital micromirror device. 12, 27, 28, 83, 92

DMSO dimethyl sulfoxide. 85

ECM extracellular matrix. 5, 7, 9–11, 13, 14, 23, 78, 80

EMT epithelial-mesenchymal transition. 5

f-actin filamentous actin. 7

FA focal adhesions. 45, 78

FBS fetal bovine serum. 83, 84

FN fibronectin. 7, 9, 11, 24–31, 43–45, 48, 52, 59, 77, 81–83, 85, 86, 90–92

FRAP fluorescent recovery after photobleaching. 1, 78, 80

g-actin globular actin. 7

GAP GTPase-activating proteins. 6

GEF guanine nucleotide exchange factors. 6

GFP green fluorescent protein. 29

GLE generalised Langevin equation. 33–36, 38, 39, 41, 74, 93

HEPES 2-[4-(2-Hydroxyethyl)piperazin-1-yl]ethane-1-sulfonic acid. 82

HUVECs human umbilical vein endothelial cells. 14

MAF Masked Autoregressive Flow. 20

MDN Mixture-Density Network. 20

MIACME Minimum Information About Cell Migration Experiments. 31, 86

MLCK myosin light chain kinase. 7

MSD mean squared displacement. v, 15, 35–37

myo6 myosin VI. 79

NDE neural density estimator. xi, 21, 22, 63–70, 72–74, 98–100

PBS phosphate-buffered saline. 81, 85

PDMS polydimethylsiloxane. 11, 13, 82, 83

PEG poly(ethylene glycol). 28, 82

PI3Ks phosphoinositide 3-kinases. 6

PINN physics-informed neural network. 74

PLL poly(L-lysine). 82

PLL PEG poly(L-lysine) grafted poly(ethylene glycol). 10, 11, 13, 43

PRW persistent random walk. 15, 17, 36, 41

rcf relative centrifugal force. 83, 84

ROCK Rho-associated protein kinase. 8, 16, 70

SBI simulation-based inference. 5, 18, 21, 22, 63, 64, 67, 70–72, 74, 78, 98

Si silicon. 11, 81

SNPE sequential neural posterior estimation. 19–21

TIRF total internal reflection. 44

UCSP universal coupling between cell speed and cell persistence. xi, 14–17, 23, 43, 57, 59, 61, 63

UV ultraviolet. 12

VACF velocity autocorrelation function. v, 34–37, 41, 93

Y-27632 Trans-4-[(1R)-aminoethyl]-N-(4-pyridinyl)cylohexanecarboxamidedihydrochloride. 8

Bibliography

[1] C. Schreiber, B. Amiri, J. C. J. Heyn, J. O. Rädler, and M. Falcke. “On the adhesion–velocity relation and length adaptation of motile cells on stepped fibronectin lanes”. en. In: *Proceedings of the National Academy of Sciences* 118.4 (2021), e2009959118.

[2] B. Amiri, J. C. J. Heyn, C. Schreiber, J. O. Rädler, and M. Falcke. “On multistability and constitutive relations of cell motion on fibronectin lanes”. en. In: *Biophysical Journal* (2023).

[3] J. C. J. Heyn, J. O. Rädler, and M. Falcke. “Mesenchymal cell migration on one-dimensional micropatterns”. English. In: *Frontiers in Cell and Developmental Biology* 12 (2024).

[4] J. C. J. Heyn, M. A. Juanatey, M. Falcke, and J. O. Rädler. *Cell-mechanical parameter estimation from 1D cell trajectories using simulation-based inference*. en. 2024.

[5] A. Klimek, J. C. J. Heyn, D. Mondal, S. Schwartz, J. O. Rädler, P. Sharma, S. Block, and R. R. Netz. *Intrinsic cell-to-cell variance from experimental single-cell motility data*. 2024.

[6] R. E. Mickens. *Mathematics And Science*. en. World Scientific, 1990.

[7] D. Thompson. *On Growth and Form*. Dover Books on Biology Series v. 1. Dover Publications, 1992.

[8] E. Schrodinger. *What is Life?: With Mind and Matter and Autobiographical Sketches*. en. Cambridge University Press, 2012.

[9] A. N. J. Heyn. “Der Mechanismus der Zellstreckung”. en. In: *Recueil des travaux botaniques néerlandais* 28.1/2 (1931), pp. 113–244.

[10] K. Pearson. *The Grammar of Science*. en. Walter Scott, 1892.

[11] W. Bialek. *Biophysics: Searching for Principles*. en. Princeton University Press, 2012.

[12] L. S. Tsimring. “Noise in Biology”. In: *Reports on progress in physics. Physical Society (Great Britain)* 77.2 (2014), p. 026601.

[13] T. D. Pollard and G. G. Borisy. “Cellular Motility Driven by Assembly and Disassembly of Actin Filaments”. English. In: *Cell* 112.4 (2003), pp. 453–465.

[14] A. I. Bachir, A. R. Horwitz, W. J. Nelson, and J. M. Bianchini. “Actin-Based Adhesion Modules Mediate Cell Interactions with the Extracellular Matrix and Neighboring Cells”. en. In: *Cold Spring Harbor Perspectives in Biology* 9.7 (2017), a023234.

[15] K. Rottner, J. Faix, S. Bogdan, S. Linder, and E. Kerkhoff. “Actin assembly mechanisms at a glance”. In: *Journal of Cell Science* 130.20 (2017), pp. 3427–3435.

[16] D. Hanahan. “Hallmarks of Cancer: New Dimensions”. en. In: *Cancer Discovery* 12.1 (2022), pp. 31–46.

[17] D. Hanahan and R. A. Weinberg. “The Hallmarks of Cancer”. In: *Cell* 100.1 (2000), pp. 57–70.

[18] D. Hanahan and R. A. Weinberg. “Hallmarks of cancer: The next generation”. In: *Cell* 144.5 (2011), pp. 646–674.

[19] D. A. Lauffenburger and A. F. Horwitz. “Cell Migration: A Physically Integrated Molecular Process”. In: *Cell* 84.3 (1996), pp. 359–369.

[20] A. J. Ridley, M. A. Schwartz, K. Burridge, R. A. Firtel, M. H. Ginsberg, G. Borisy, J. T. Parsons, and A. R. Horwitz. “Cell Migration: Integrating Signals from Front to Back”. In: *Science* 302.5651 (2003), pp. 1704–1709.

[21] F. Fäßler, M. G. Javoor, and F. K. Schur. “Deciphering the molecular mechanisms of actin cytoskeleton regulation in cell migration using cryo-EM”. en. In: *Biochemical Society Transactions* (2023), BST20220221.

[22] M. Ladwein and K. Rottner. “On the Rho’d: The regulation of membrane protrusions by Rho-GTPases”. In: *FEBS Letters* 582.14 (2008), pp. 2066–2074.

[23] G. Danuser, J. Allard, and A. Mogilner. “Mathematical Modeling of Eukaryotic Cell Migration: Insights Beyond Experiments”. In: *Annual Review of Cell and Developmental Biology* 29.1 (2013), pp. 501–528.

[24] M. Enculescu and M. Falcke. “Modeling Morphodynamic Phenotypes and Dynamic Regimes of Cell Motion”. en. In: *Advances in Systems Biology*. Ed. by I. I. Goryanin and A. B. Goryachev. New York, NY: Springer, 2012, pp. 337–358.

[25] A. Mogilner. “Mathematics of cell motility: have we got its number?” en. In: *Journal of Mathematical Biology* 58.1 (2009), pp. 105–134.

[26] N. Kramer, A. Walzl, C. Unger, M. Rosner, G. Krupitza, M. Hengstschläger, and H. Dolznig. “*In vitro* cell migration and invasion assays”. In: *Mutation Research/Reviews in Mutation Research* 752.1 (2013), pp. 10–24.

[27] Y. Hu, M. L. Becker, and R. K. Willits. “Quantification of cell migration: metrics selection to model application”. In: *Frontiers in Cell and Developmental Biology* 11 (2023).

[28] L. Tomasova, Z. Guttenberg, B. Hoffmann, and R. Merkel. “Advanced 2D/3D cell migration assay for faster evaluation of chemotaxis of slow-moving cells”. en. In: *PLOS ONE* 14.7 (2019), e0219708.

[29] P. Bouchalova and P. Bouchal. “Current methods for studying metastatic potential of tumor cells”. en. In: *Cancer Cell International* 22.1 (2022), p. 394.

[30] J. Ren, N. Wang, P. Guo, Y. Fan, F. Lin, and J. Wu. “Recent advances in microfluidics-based cell migration research”. en. In: *Lab on a Chip* 22.18 (2022), pp. 3361–3376.

[31] H. J. Choi, C. Wang, X. Pan, J. Jang, M. Cao, J. A. Brazzo, Y. Bae, and K. Lee. “Emerging machine learning approaches to phenotyping cellular motility and morphodynamics”. en. In: *Physical Biology* 18.4 (2021), p. 041001.

[32] P. Maiuri, E. Terriac, P. Paul-Gilloteaux, T. Vignaud, K. McNally, J. Onuffer, K. Thorn, P. A. Nguyen, N. Georgoulia, D. Soong, A. Jayo, N. Beil, J. Beneke, J. C. Hong Lim, C. Pei-Ying Sim, Y.-S. Chu, A. Jiménez-Dalmaroni, J.-F. Joanny, J.-P. Thiery, H. Erfle, M. Parsons, T. J. Mitchison, W. A. Lim, A.-M. Lennon-Duménil, M. Piel, and M. Théry. “The first World Cell Race”. en. In: *Current Biology* 22.17 (2012), R673–R675.

[33] F. Zhou, S. A. Schaffer, C. Schreiber, F. J. Segerer, A. Goychuk, E. Frey, and J. O. Rädler. “Quasi-periodic migration of single cells on short microlanes”. en. In: *PLOS ONE* 15.4 (2020), e0230679.

[34] C. Schreiber. “1D single-cell migration on microlanes and at interfaces”. PhD thesis. Ludwig-Maximilians-Universität, 2019.

[35] K. Patsch, C.-L. Chiu, M. Engeln, D. B. Agus, P. Mallick, S. M. Mumenthaler, and D. Ruderman. “Single cell dynamic phenotyping”. en. In: *Scientific Reports* 6.1 (2016), p. 34785.

[36] F. André, E. Rassy, A. Marabelle, S. Michiels, and B. Besse. “Forget lung, breast or prostate cancer: why tumour naming needs to change”. en. In: *Nature* 626.7997 (2024), pp. 26–29.

[37] X. Fu, G. Liu, A. Halim, Y. Ju, Q. Luo, and G. Song. “Mesenchymal Stem Cell Migration and Tissue Repair”. In: *Cells* 8.8 (2019), p. 784.

[38] J. E. Bear and J. M. Haugh. “Directed migration of mesenchymal cells: where signaling and the cytoskeleton meet”. In: *Current opinion in cell biology* 0 (2014), pp. 74–82.

[39] P. Friedl and D. Gilmour. “Collective cell migration in morphogenesis, regeneration and cancer”. en. In: *Nature Reviews Molecular Cell Biology* 10.7 (2009), pp. 445–457.

[40] Singer Adam J. and Clark Richard A.F. “Cutaneous Wound Healing”. In: *New England Journal of Medicine* 341.10 (1999), pp. 738–746.

[41] A. D. Luster, R. Alon, and U. H. von Andrian. “Immune cell migration in inflammation: present and future therapeutic targets”. en. In: *Nature Immunology* 6.12 (2005), pp. 1182–1190.

[42] A. Mongera, P. Rowghanian, H. J. Gustafson, E. Shelton, D. A. Kealhofer, E. K. Carn, F. Serwane, A. A. Lucio, J. Giammona, and O. Campàs. “A fluid-to-solid jamming transition underlies vertebrate body axis elongation”. en. In: *Nature* 561.7723 (2018), pp. 401–405.

[43] A. K. Lawton, A. Nandi, M. J. Stulberg, N. Dray, M. W. Sneddon, W. Pontius, T. Emonet, and S. A. Holley. “Regulated tissue fluidity steers zebrafish body elongation”. In: *Development* 140.3 (2013), pp. 573–582.

[44] D. Kimelman. “Chapter Twenty-Nine - Tales of Tails (and Trunks): Forming the Posterior Body in Vertebrate Embryos”. In: *Current Topics in Developmental Biology*. Ed. by P. M. Wassarman. Vol. 116. Essays on Developmental Biology, Part A. Academic Press, 2016, pp. 517–536.

[45] *Fibroblast | Definition, Histology, & Function | Britannica*. en.

[46] *Definition of mesenchymal - NCI Dictionary of Cancer Terms - NCI*. en. nciAppModulePage. 2011.

[47] K. MacCord. *Mesenchyme*. en. Tech. rep. Arizona State University. School of Life Sciences. Center for Biology and Society. Embryo Project Encyclopedia.|Arizona Board of Regents, 2012.

[48] T. W. Sadler. *Langman’s Medical Embryology*. en. Lippincott Williams & Wilkins, 2022.

[49] P. Singleton and D. Sainsbury. *Dictionary of microbiology and molecular biology. 2nd ed*. United States, 1988.

[50] F. Merino-Casallo, M. J. Gomez-Benito, S. Hervas-Raluy, and J. M. Garcia-Aznar. “Unravelling cell migration: defining movement from the cell surface”. In: *Cell Adhesion & Migration* 16.1 (2022), pp. 25–64.

[51] A. J. Ridley. “Life at the leading edge”. In: *Cell* 145.7 (2011), pp. 1012–1022.

[52] M. Machacek, L. Hodgson, C. Welch, H. Elliott, O. Pertz, P. Nalbant, A. Abell, G. L. Johnson, K. M. Hahn, and G. Danuser. “Coordination of Rho GTPase activities during cell protrusion”. en. In: *Nature* 461.7260 (2009), pp. 99–103.

[53] C. D. Lawson and K. Burridge. “The on-off relationship of Rho and Rac during integrin-mediated adhesion and cell migration”. In: *Small GTPases* 5.1 (2014), e27958.

[54] A. Sadok and C. J. Marshall. “Rho GTPases: Masters of cell migration”. In: *Small GTPases* 5.4 (2014), e983878.

[55] S. Etienne-Manneville and A. Hall. “Integrin-Mediated Activation of Cdc42 Controls Cell Polarity in Migrating Astrocytes through PKC”. English. In: *Cell* 106.4 (2001), pp. 489–498.

[56] K. Riento and A. J. Ridley. “ROCKs: multifunctional kinases in cell behaviour”. en. In: *Nature Reviews Molecular Cell Biology* 4.6 (2003), pp. 446–456.

[57] C. S. Peskin, G. M. Odell, and G. F. Oster. “Cellular motions and thermal fluctuations: the Brownian ratchet”. en. In: *Biophysical Journal* 65.1 (1993), pp. 316–324.

[58] A. Mogilner and G. Oster. “Cell motility driven by actin polymerization”. en. In: *Biophysical Journal* 71.6 (1996), pp. 3030–3045.

[59] M. Abercrombie, J. E. Heaysman, and S. M. Pegrum. “The locomotion of fibroblasts in culture. IV. Electron microscopy of the leading lamella”. In: *Experimental Cell Research* 67.2 (1971), pp. 359–367.

[60] M. Abercrombie. “The Croonian Lecture, 1978 - The crawling movement of metazoan cells”. In: *Proceedings of the Royal Society of London. Series B. Biological Sciences* 207.1167 (1980), pp. 129–147.

[61] A. T. Dawes and L. Edelstein-Keshet. “Phosphoinositides and Rho Proteins Spatially Regulate Actin Polymerization to Initiate and Maintain Directed Movement in a One-Dimensional Model of a Motile Cell”. In: *Biophys J* 92.3 (2007), pp. 744–768.

[62] R. H. Insall and L. M. Machesky. “Actin Dynamics at the Leading Edge: From Simple Machinery to Complex Networks”. In: *Developmental Cell* 17.3 (2009), pp. 310–322.

[63] A. J. Lomakin, K. C. Lee, S. J. Han, D. A. Bui, M. Davidson, A. Mogilner, and G. Danuser. “Competition for actin between two distinct F-actin networks defines a bistable switch for cell polarization”. In: *Nature Cell Biology* 17.11 (2015), pp. 1435–1445.

[64] J. V. Small and J. E. Celis. “Filament arrangements in negatively stained cultured cells: the organization of actin”. In: *Cytobiology* 16 (1978), pp. 308–325.

[65] J. V. Small, G. Isenberg, and J. E. Celis. “Polarity of actin at the leading edge of cultured cells”. In: *Nature* 272.5654 (1978), pp. 638–639.
[66] T. M. Svitkina, A. B. Verkhovsky, K. M. McQuade, and G. G. Borisy. “Analysis of the Actin-Myosin II System in Fish Epidermal Keratocytes: Mechanism of Cell Body Translocation”. In: *J Cell Biol* 139 (1997), pp. 397–415.
[67] J. V. Small, T. Stradal, E. Vignal, and K. Rottner. “The lamellipodium: where motility begins”. English. In: *Trends in Cell Biology* 12.3 (2002), pp. 112–120.
[68] T. Pollard. “The cytoskeleton, cellular motility and the reductionist agenda”. In: *Nature* 422 (2003), pp. 741–745.
[69] W. Oosterheert, B. U. Klink, A. Belyy, S. Pospich, and S. Raunser. “Structural basis of actin filament assembly and aging”. en. In: *Nature* 611.7935 (2022), pp. 374–379.
[70] M. J. Reynolds, C. Hachicho, A. G. Carl, R. Gong, and G. M. Alushin. “Bending forces and nucleotide state jointly regulate F-actin structure”. en. In: *Nature* 611.7935 (2022), pp. 380–386.
[71] J. P. Bibeau, N. G. Pandit, S. Gray, N. Shatery Nejad, C. V. Sindelar, W. Cao, and E. M. De La Cruz. “Twist response of actin filaments”. In: *Proceedings of the National Academy of Sciences* 120.4 (2023), e2208536120.
[72] P. J. Carman, K. R. Barrie, G. Rebowski, and R. Dominguez. “Structures of the free and capped ends of the actin filament”. In: *Science* 380.6651 (2023), pp. 1287–1292.
[73] F. Buss, G. Spudich, and J. Kendrick-Jones. “MYOSIN VI: Cellular Functions and Motor Properties”. en. In: *Annual Review of Cell and Developmental Biology* 20.1 (2004), pp. 649–676.
[74] A. L. Wells, A. W. Lin, L.-Q. Chen, D. Safer, S. M. Cain, T. Hasson, B. O. Carragher, R. A. Milligan, and H. L. Sweeney. “Myosin VI is an actin-based motor that moves backwards”. en. In: *Nature* 401.6752 (1999), pp. 505–508.
[75] T. Hodge and M. J. T. V. Cope. “A myosin family tree”. In: *Journal of Cell Science* 113.19 (2000), pp. 3353–3354.
[76] V. Betapudi, L. S. Licate, and T. T. Egelhoff. “Distinct roles of nonmuscle myosin II isoforms in the regulation of MDA-MB-231 breast cancer cell spreading and migration”. In: *Cancer Research* 66.9 (2006), pp. 4725–4733.
[77] Y. Minamiya, T. Nakagawa, H. Saito, I. Matsuzaki, K. Taguchi, M. Ito, and J.-i. Ogawa. “Increased Expression of Myosin Light Chain Kinase mRNA Is Related to Metastasis in Non-Small Cell Lung Cancer”. In: *Tumor Biology* 26.3 (2005), pp. 153–157.
[78] M. Kovács, J. Tóth, C. Hetényi, A. Málnási-Csizmadia, and J. R. Seller. “Mechanism of blebbistatin inhibition of myosin II”. In: *Journal of Biological Chemistry* 279.34 (2004), pp. 35557–35563.
[79] A. F. Straight, A. Cheung, J. Limouze, I. Chen, N. J. Westwood, J. R. Sellers, and T. J. Mitchison. “Dissecting temporal and spatial control of cytokinesis with a myosin II inhibitor”. In: *Science* 299.5613 (2003), pp. 1743–1747.
[80] A. Huttenlocher, M. H. Ginsberg, and A. F. Horwitz. “Modulation of cell migration by integrin-mediated cytoskeletal linkages and ligand-binding affinity.” In: *Journal of Cell Biology* 134.6 (1996), pp. 1551–1562.
[81] S. P. Palecek, J. C. Loftus, M. H. Ginsberg, D. A. Lauffenburger, and A. F. Horwitz. “Integrin-ligand binding properties govern cell migration speed through cell-substratum adhesiveness”. In: *Nature* 385.6616 (1997), pp. 537–540.
[82] M. P. Sheetz, D. P. Felsenfeld, and C. G. Galbraith. “Cell migration: regulation of force on extracellular-matrix-integrin complexes”. In: *Trends in Cell Biology* 8.2 (1998), pp. 51–54.
[83] M. Vicente-Manzanares, C. K. Choi, and A. R. Horwitz. “Integrins in cell migration - the actin connection”. In: *Journal of Cell Science* 122.2 (2009), pp. 199–206.
[84] J. T. Parsons, A. R. Horwitz, and M. A. Schwartz. “Cell adhesion: integrating cytoskeletal dynamics and cellular tension”. In: *Nat Rev Mol Cell Biol* 11.9 (2010), pp. 633–643.
[85] T. D. Ross, B. G. Coon, S. Yun, N. Baeyens, K. Tanaka, M. Ouyang, and M. A. Schwartz. “Integrins in mechanotransduction”. en. In: *Current Opinion in Cell Biology*. Cell adhesion and migration 25.5 (2013), pp. 613–618.

[86] K. Burridge and C. Guilluy. “Focal adhesions, stress fibers and mechanical tension”. In: *Experimental Cell Research* 343.1 (2016), pp. 14–20.

[87] X. Li, J. D. Combs, K. Salaita, and X. Shu. “Polarized focal adhesion kinase activity within a focal adhesion during cell migration”. en. In: *Nature Chemical Biology* (2023), pp. 1–11.

[88] T. Lämmermann, B. L. Bader, S. J. Monkley, T. Worbs, R. Wedlich-Söldner, K. Hirsch, M. Keller, R. Förster, D. R. Critchley, R. Fässler, and M. Sixt. “Rapid leukocyte migration by integrin-independent flowing and squeezing”. en. In: *Nature* 453.7191 (2008), pp. 51–55.

[89] G. Giannone, B. J. Dubin-Thaler, O. Rossier, Y. Cai, O. Chaga, G. Jiang, W. Beaver, H. G. Döbereiner, Y. Freund, G. Borisy, and M. P. Sheetz. “Lamellipodial Actin Mechanically Links Myosin Activity with Adhesion-Site Formation”. In: *Cell* 128.3 (2007), pp. 561–575.

[90] T. J. Mitchison and L. P. Cramer. “Actin-Based Cell Motility and Cell Locomotion”. English. In: *Cell* 84.3 (1996), pp. 371–379.

[91] J. Howard. *Mechanics of Motor Proteins and the Cytoskeleton*. Sinauer, 2005.

[92] R. O. Hynes. “Integrins: Bidirectional, Allosteric Signaling Machines”. English. In: *Cell* 110.6 (2002), pp. 673–687.

[93] J. D. Humphries, A. Byron, and M. J. Humphries. “Integrin ligands at a glance”. In: *Journal of Cell Science* 119.19 (2006), pp. 3901–3903.

[94] R. A. Clark, J. M. Lanigan, P. DellaPelle, E. Manseau, H. F. Dvorak, and R. B. Colvin. “Fibronectin and fibrin provide a provisional matrix for epidermal cell migration during wound reepithelialization”. In: *Journal of Investigative Dermatology* 79.5 (1982), pp. 264–269.

[95] M. Leiss, K. Beckmann, A. Girós, M. Costell, and R. Fässler. “The role of integrin binding sites in fibronectin matrix assembly *in vivo*”. In: *Current Opinion in Cell Biology*. Cell-to-cell contact and extracellular matrix 20.5 (2008), pp. 502–507.

[96] M. D. Pierschbacher and E. Ruoslahti. “Variants of the cell recognition site of fibronectin that retain attachment-promoting activity.” In: *Proceedings of the National Academy of Sciences* 81.19 (1984), pp. 5985–5988.

[97] R. Pytela, M. D. Pierschbacher, and E. Ruoslahti. “Identification and isolation of a 140 kd cell surface glycoprotein with properties expected of a fibronectin receptor”. In: *Cell* 40.1 (1985), pp. 191–198.

[98] B. Geiger, J. P. Spatz, and A. D. Bershadsky. “Environmental sensing through focal adhesions”. en. In: *Nature Reviews Molecular Cell Biology* 10.1 (2009), pp. 21–33.

[99] C. K. Choi, M. Vicente-Manzanares, J. Zareno, L. A. Whitmore, A. Mogilner, and A. R. Horwitz. “Actin and α-actinin orchestrate the assembly and maturation of nascent adhesions in a myosin II motor-independent manner”. In: *Nature Cell Biology* 10.9 (2008), pp. 1039–1050.

[100] H. B. Schiller, M.-R. Hermann, J. Polleux, T. Vignaud, S. Zanivan, C. C. Friedel, Z. Sun, A. Raducanu, K.-E. Gottschalk, M. Théry, M. Mann, and R. Fässler. “β1- and αv-class integrins cooperate to regulate myosin II during rigidity sensing of fibronectin-based microenvironments”. en. In: *Nature Cell Biology* 15.6 (2013), pp. 625–636.

[101] T. D. Pollard. “Actin and Actin-Binding Proteins”. en. In: *Cold Spring Harbor Perspectives in Biology* 8.8 (2016), a018226.

[102] S. Wang, A. H. Crevenna, I. Ugur, A. Marion, I. Antes, U. Kazmaier, M. Hoyer, D. C. Lamb, F. Gegenfurtner, Z. Kliesmete, C. Ziegenhain, W. Enard, A. Vollmar, and S. Zahler. “Actin stabilizing compounds show specific biological effects due to their binding mode”. en. In: *Scientific Reports* 9.1 (2019), p. 9731.

[103] M. Coué, S. L. Brenner, I. Spector, and D. Korn. “Inhibition of actin polymerization by latrunculin A”. In: *FEBS Letters* 213.2 (1987), pp. 316–318.

[104] K. Katagiri and S. Matsuura. “Antitumor activity of Cytochalasin D”. en. In: *The Journal of Antibiotics* 24.10 (1971), pp. 722–723.

[105] Y. Kashman, A. Groweiss, and U. Shmueli. “Latrunculin, a new 2-thiazolidinone macrolide from the marine sponge latrunculia magnifica”. In: *Tetrahedron Letters* 21.37 (1980), pp. 3629–3632.

[106] I. Spector, N. R. Shochet, Y. Kashman, and A. Groweiss. “Latrunculins: novel marine toxins that disrupt microfilament organization in cultured cells”. In: *Science* 219.4584 (1983), pp. 493–495.

[107] I. Löw, P. Dancker, and T. Wieland. “Stabilization of F-actin by phalloidin reversal of the destabilizing effect of cytochalasin B”. en. In: *FEBS Letters* 54.2 (1975), pp. 263–265.

[108] M. Uehata, T. Ishizaki, H. Satoh, T. Ono, T. Kawahara, T. Morishita, H. Tamakawa, K. Yamagami, J. Inui, M. Maekawa, and S. Narumiya. “Calcium sensitization of smooth muscle mediated by a Rho-associated protein kinase in hypertension”. en. In: *Nature* 389.6654 (1997), pp. 990–994.

[109] K. Kuwahara, Y. Saito, O. Nakagawa, I. Kishimoto, M. Harada, E. Ogawa, Y. Miyamoto, I. Hamanaka, N. Kajiyama, N. Takahashi, T. Izumi, R. Kawakami, N. Tamura, Y. Ogawa, and K. Nakao. “The effects of the selective ROCK inhibitor, Y27632, on ET-1-induced hypertrophic response in neonatal rat cardiac myocytes – possible involvement of Rho/ROCK pathway in cardiac muscle cell hypertrophy”. en. In: *FEBS Letters* 452.3 (1999), pp. 314–318.

[110] D. J. Campbell, C. H. Kim, and E. C. Butcher. “Chemokines in the systemic organization of immunity”. en. In: *Immunological Reviews* 195.1 (2003), pp. 58–71.

[111] K. M. Yamada and M. Sixt. “Mechanisms of 3D cell migration”. en. In: *Nature Reviews Molecular Cell Biology* 20.12 (2019), pp. 738–752.

[112] E. Vercruysse, D. B. Brückner, M. Gómez-González, A. Remson, M. Luciano, Y. Kalukula, L. Rossetti, X. Trepat, E. Hannezo, and S. Gabriele. “Geometry-driven migration efficiency of autonomous epithelial cell clusters”. en. In: *Nature Physics* (2024), pp. 1–9.

[113] J. Scott Gruver, A. A. Potdar, J. Jeon, J. Sai, B. Anderson, D. Webb, A. Richmond, V. Quaranta, P. T. Cummings, and C. Y. Chung. “Bimodal Analysis Reveals a General Scaling Law Governing Nondirected and Chemotactic Cell Motility”. In: *Biophysical Journal* 99.2 (2010), pp. 367–376.

[114] T. Jin and D. Hereld. *Methods in Molecular Biology: Chemotaxis*. 2009.

[115] A. Shellard and R. Mayor. “Durotaxis: The Hard Path from In Vitro to In Vivo”. In: *Developmental Cell* 56.2 (2021), pp. 227–239.

[116] L. G. Vincent, Y. S. Choi, B. Alonso-Latorre, J. C. del Álamo, and A. J. Engler. “Mesenchymal stem cell durotaxis depends on substrate stiffness gradient strength”. en. In: *Biotechnology Journal* 8.4 (2013), pp. 472–484.

[117] I. Pi-Jaumà, R. Alert, and J. Casademunt. “Collective durotaxis of cohesive cell clusters on a stiffness gradient”. en. In: *The European Physical Journal E* 45.1 (2022), p. 7.

[118] C. M. Ferrer, H. M. Cho, R. Boon, T. Bernasocchi, L. P. Wong, M. Cetinbas, E. R. Haggerty, I. Mitsiades, G. R. Wojtkiewicz, D. E. McLoughlin, R. Aboushousha, H. Abdelhamid, S. Kugel, E. Rheinbay, R. Sadreyev, D. Juric, Y. M. W. Janssen-Heininger, and R. Mostoslavsky. “The glutathione S-transferase Gstt1 drives survival and dissemination in metastases”. en. In: *Nature Cell Biology* 26.6 (2024), pp. 975–990.

[119] K. Wolf, M. te Lindert, M. Krause, S. Alexander, J. te Riet, A. L. Willis, R. M. Hoffman, C. G. Figdor, S. J. Weiss, and P. Friedl. “Physical limits of cell migration: Control by ECM space and nuclear deformation and tuning by proteolysis and traction force”. In: *Journal of Cell Biology* 201.7 (2013), pp. 1069–1084.

[120] S. Even-Ram and K. M. Yamada. “Cell migration in 3D matrix”. In: *Current Opinion in Cell Biology*. Cell-to-cell contact and extracellular matrix 17.5 (2005), pp. 524–532.

[121] G. Giannone, B. J. Dubin-Thaler, Hans-Günther Döbereiner, N. Kieffer, A. R. Bresnick, and M. P. Sheetz. “Periodic Lamellipodial Contractions Correlate with Rearward Actin Waves”. In: *Cell* 116.3 (2004), pp. 431–443.

[122] H.-G. Döbereiner, B. J. Dubin-Thaler, J. M. Hofman, H. S. Xenias, T. N. Sims, Gregory Giannone, M. L. Dustin, C. H. Wiggins, and M. P. Sheetz. “Lateral Membrane Waves Constitute a Universal Dynamic Pattern of Motile Cells”. In: *Phys Rev Lett* 97.3 (2006), p. 038102.

[123] M. Enculescu, A. Gholami, and M. Falcke. “Dynamic regimes and bifurcations in a model of actin-based motility”. In: *Physical Review E* 78.3 (2008), p. 031915.

[124] A. Gholami, M. Falcke, and E. Frey. “Velocity oscillations in actin-based motility”. In: *New Journal of Physics* 10 (2008), p. 033022.

[125] S. A. Koestler, S. Auinger, M. Vinzenz, K. Rottner, and J. V. Small. “Differentially oriented populations of actin filaments generated in lamellipodia collaborate in pushing and pausing at the cell front”. In: *Nature Cell Biology* 10.3 (2008), pp. 306–313.

[126] T. Bretschneider, K. Anderson, M. Ecke, A. Müller-Taubenberger, B. Schroth-Diez, H. C. Ishikawa-Ankerhold, and Günther Gerisch. “The Three-Dimensional Dynamics of Actin Waves, a Model of Cytoskeletal Self-Organization”. In: *Biophys J* 96.7 (2009), pp. 2888–2900.

[127] M. Enculescu, M. Sabouri-Ghomi, G. Danuser, and M. Falcke. “Modeling of Protrusion Phenotypes Driven by the Actin-Membrane Interaction”. In: *Biophys J* 98.8 (2010), pp. 1571–1581.

[128] D. T. Burnette, S. Manley, P. Sengupta, R. Sougrat, M. W. Davidson, B. Kachar, and J. Lippincott-Schwartz. “A role for actin arcs in the leading-edge advance of migrating cells”. In: *Nat Cell Biol* 13.4 (2011), pp. 371–382.

[129] K. Doubrovinski and K. Kruse. “Cell Motility Resulting from Spontaneous Polymerization Waves”. In: *Physical Review Letters* 107.25 (2011), p. 258103.

[130] J. Allard and A. Mogilner. “Traveling waves in actin dynamics and cell motility”. In: *Current Opinion in Cell Biology*. Cell architecture 25.1 (2013), pp. 107–115.

[131] F. Ziebert and I. S. Aranson. “Effects of Adhesion Dynamics and Substrate Compliance on the Shape and Motility of Crawling Cells”. In: *Plos One* 8.5 (2013).

[132] M. Gerhardt, M. Ecke, M. Walz, A. Stengl, C. Beta, and G. Gerisch. “Actin and PIP3 waves in giant cells reveal the inherent length scale of an excited state”. In: *Journal of Cell Science* 127.20 (2014), pp. 4507–4517.

[133] J. Zimmermann and M. Falcke. “Formation of transient lamellipodia”. In: *PLoS ONE* 9.2 (2014), pp. 1–11.

[134] E. L. Barnhart, J. Allard, S. S. Lou, J. A. Theriot, and A. Mogilner. “Adhesion-Dependent Wave Generation in Crawling Cells”. In: *Current Biology* 27.1 (2017), pp. 27–38.

[135] C. Beta and K. Kruse. “Intracellular Oscillations and Waves”. In: *Annual Review of Condensed Matter Physics* 8.1 (2017), pp. 239–264.

[136] J. Park, W. R. Holmes, S. H. Lee, H. N. Kim, D. H. Kim, M. K. Kwak, C. J. Wang, L. Edelstein-Keshet, and A. Levchenko. “Mechanochemical feedback underlies coexistence of qualitatively distinct Cell polarity patterns within diverse cell populations”. In: *Proceedings of the National Academy of Sciences of the United States of America* 114.28 (2017), E5750–E5759.

[137] A. Bolado-Carrancio, O. S. Rukhlenko, E. Nikonova, M. A. Tsyganov, A. Wheeler, A. Garcia-Munoz, W. Kolch, A. von Kriegsheim, and B. N. Kholodenko. “Periodic propagating waves coordinate RhoGTPase network dynamics at the leading and trailing edges during cell migration”. en. In: *eLife* 9 (2020), e58165.

[138] K. Hennig, I. Wang, P. Moreau, L. Valon, S. DeBeco, M. Coppey, Y. A. Miroshnikova, C. Albiges-Rizo, C. Favard, R. Voituriez, and M. Balland. “Stick-slip dynamics of cell adhesion triggers spontaneous symmetry breaking and directional migration of mesenchymal cells on one-dimensional lines”. In: *Science Advances* 6.1 (2020), pp. 1–13.

[139] S. H. Lee, J. C. Hou, A. Hamidzadeh, M. S. Yousafzai, V. Ajeti, H. Chang, D. J. Odde, M. Murrell, and A. Levchenko. “A molecular clock controls periodically driven cell migration in confined spaces”. In: *Cell Systems* 13.7 (2022), 514–529.e10.

[140] F. Lautenschläger and M. Piel. “Microfabricated devices for cell biology: All for one and one for all”. In: *Current Opinion in Cell Biology* 25.1 (2013), pp. 116–124.

[141] M. Abercrombie and J. E. M. Heaysman. “Observations on the social behaviour of cells in tissue culture: II. “Monolayering” of fibroblasts”. In: *Experimental Cell Research* 6.2 (1954), pp. 293–306.

[142] P. Maiuri, J. F. Rupprecht, S. Wieser, V. Ruprecht, O. Bénichou, N. Carpi, M. Coppey, S. De Beco, N. Gov, C. P. Heisenberg, C. Lage Crespo, F. Lautenschlaeger, M. Le Berre, A. M. Lennon-Dumenil, M. Raab, H. R. Thiam, M. Piel, M. Sixt, and R. Voituriez. “Actin flows mediate a universal coupling between cell speed and cell persistence”. In: *Cell* 161.2 (2015), pp. 374–386.

[143] V. Ruprecht, S. Wieser, A. Callan-Jones, M. Smutny, H. Morita, K. Sako, V. Barone, M. Ritsch-Marte, M. Sixt, R. Voituriez, and C. P. Heisenberg. “Cortical Contractility Triggers a Stochastic Switch to Fast Amoeboid Cell Motility”. In: *Cell* 160.4 (2015), pp. 673–685.

[144] C. Schreiber, F. J. Segerer, E. Wagner, A. Roidl, and J. O. Rädler. “Ring-Shaped Microlanes and Chemical Barriers as a Platform for Probing Single-Cell Migration”. In: *Scientific Reports* 6 (2016).

[145] S. L. Schuster, F. J. Segerer, F. A. Gegenfurtner, K. Kick, C. Schreiber, M. Albert, A. M. Vollmar, J. O. Rädler, and S. Zahler. “Contractility as a global regulator of cellular morphology, velocity, and directionality in low-adhesive fibrillary micro-environments”. In: *Biomaterials* 102 (2016), pp. 137–147.

[146] B. Ljepoja, C. Schreiber, F. A. Gegenfurtner, J. García-Roman, B. Köhler, S. Zahler, J. O. Rädler, E. Wagner, and A. Roidl. “Inducible microRNA-200c decreases motility of breast cancer cells and reduces filamin A”. en. In: *PLOS ONE* 14.11 (2019), e0224314.

[147] P. Monzo, M. Crestani, Y. K. Chong, A. Ghisleni, K. Hennig, Q. Li, N. Kakogiannos, M. Giannotta, C. Richichi, T. Dini, E. Dejana, P. Maiuri, M. Balland, M. P. Sheetz, G. Pelicci, B. T. Ang, C. Tang, and N. C. Gauthier. “Adaptive mechanoproperties mediated by the formin FMN1 characterize glioblastoma fitness for invasion”. en. In: *Developmental Cell* 56.20 (2021), 2841–2855.e8.

[148] Y. Kim, L. T. H. Tram, K. A. Kim, and B. C. Kim. “Defining Integrin Tension Required for Chemotaxis of Metastatic Breast Cancer Cells in Confinement”. en. In: *Advanced Healthcare Materials* n/a.n/a (2023), p. 2202747.

[149] C. O’Neill, P. Jordan, P. Riddle, and G. Ireland. “Narrow linear strips of adhesive substratum are powerful inducers of both growth and total focal contact area”. In: *Journal of Cell Science* 95.4 (1990), pp. 577–586.

[150] T. Matsuda and T. Sugawara. “Control of cell adhesion, migration, and orientation on photochemically microprocessed surfaces”. en. In: *Journal of Biomedical Materials Research* 32.2 (1996), pp. 165–173.

[151] E. M. Levina, M. A. Kharitonova, Y. A. Rovensky, and J. M. Vasiliev. “Cytoskeletal control of fibroblast length: experiments with linear strips of substrate”. In: *Journal of Cell Science* 114.23 (2001), pp. 4335–4341.

[152] F. Pouthas, P. Girard, V. Lecaudey, T. B. N. Ly, D. Gilmour, C. Boulin, R. Pepperkok, and E. G. Reynaud. “In migrating cells, the Golgi complex and the position of the centrosome depend on geometrical constraints of the substratum”. In: *Journal of Cell Science* 121.14 (2008), pp. 2406–2414.

[153] D. Mohammed, G. Charras, E. Vercruysse, M. Versaevel, J. Lantoine, L. Alaimo, C. Bruyère, M. Luciano, K. Glinel, G. Delhaye, O. Théodoly, and S. Gabriele. “Substrate area confinement is a key determinant of cell velocity in collective migration”. en. In: *Nature Physics* 15.8 (2019), pp. 858–866.

[154] C. Baltes, D. G. Thalla, U. Kazmaier, and F. Lautenschläger. “Actin stabilization in cell migration”. English. In: *Frontiers in Cell and Developmental Biology* 10 (2022).

[155] M. Piel and M. Théry. *Micropatterning in Cell Biology, Part A*. en. Methods in Cell Biology 119. Elsevier, 2014.

[156] M. Piel and M. Théry. *Micropatterning in Cell Biology, Part C*. en. Methods in Cell Biology 121. Academic Press, 2014.

[157] V. Ruprecht, P. Monzo, A. Ravasio, Z. Yue, E. Makhija, P. O. Strale, N. Gauthier, G. V. Shivashankar, V. Studer, C. Albiges-Rizo, and V. Viasnoff. “How cells respond to environmental cues – insights from bio-functionalized substrates”. In: *Journal of Cell Science* 130.1 (2017). Ed. by A. Ewald, pp. 51–61.

[158] D. Falconnet, G. Csucs, H. Michelle Grandin, and M. Textor. “Surface engineering approaches to micropattern surfaces for cell-based assays”. In: *Biomaterials* 27.16 (2006), pp. 3044–3063.

[159] J. L. Tan, W. Liu, C. M. Nelson, S. Raghavan, and C. S. Chen. “Simple Approach to Micropattern Cells on Common Culture Substrates by Tuning Substrate Wettability”. In: *Tissue Engineering* 10.5-6 (2004), pp. 865–872.

[160] E. D'Arcangelo and A. P. McGuigan. "Micropatterning strategies to engineer controlled cell and tissue architecture in vitro". In: *BioTechniques* 58.1 (2015), pp. 13–23.
[161] J. M. Bélisle, J. P. Correia, P. W. Wiseman, T. E. Kennedy, and S. Costantino. "Patterning protein concentration using laser-assisted adsorption by photobleaching, LAPAP". en. In: *Lab on a Chip* 8.12 (2008), pp. 2164–2167.
[162] J. M. Bélisle, D. Kunik, and S. Costantino. "Rapid multicomponent optical protein patterning". en. In: *Lab on a Chip* 9.24 (2009), pp. 3580–3585.
[163] A. Azioune, M. Storch, M. Bornens, M. Théry, and M. Piel. "Simple and rapid process for single cell micro-patterning". en. In: *Lab on a Chip* 9.11 (2009), pp. 1640–1642.
[164] A. D. Doyle, F. W. Wang, K. Matsumoto, and K. M. Yamada. "One-dimensional topography underlies three-dimensional fibrillar cell migration". In: *Journal of Cell Biology* 184.4 (2009), pp. 481–490.
[165] S. G. Ricoult, T. E. Kennedy, and D. Juncker. "Substrate-Bound Protein Gradients to Study Haptotaxis". In: *Frontiers in Bioengineering and Biotechnology* 3 (2015).
[166] A. Azioune, N. Carpi, Q. Tseng, M. Théry, and M. Piel. "Protein Micropatterns. A Direct Printing Protocol Using Deep UVs." In: *Methods in Cell Biology* 97.C (2010), pp. 133–146.
[167] P.-O. Strale, A. Azioune, G. Bugnicourt, Y. Lecomte, M. Chahid, and V. Studer. "Multiprotein Printing by Light-Induced Molecular Adsorption". In: *Advanced Materials* 28.10 (2016), pp. 2024–2029.
[168] A. D. Doyle, R. J. Petrie, M. L. Kutys, and K. M. Yamada. "Dimensions in cell migration". en. In: *Current Opinion in Cell Biology*. Cell adhesion and migration 25.5 (2013), pp. 642–649.
[169] K. M. Yamada, A. D. Doyle, and J. Lu. "Cell–3D matrix interactions: recent advances and opportunities". English. In: *Trends in Cell Biology* 32.10 (2022), pp. 883–895.
[170] P. Weiss and B. Garber. "Shape and Movement of Mesenchyme Cells as Functions of the Physical Structure of the Medium". In: *Proceedings of the National Academy of Sciences* 38.3 (1952), pp. 264–280.
[171] J. d'Alessandro, A. Barbier–Chebbah, V. Cellerin, O. Benichou, R. M. Mège, R. Voituriez, and B. Ladoux. "Cell migration guided by long-lived spatial memory". en. In: *Nature Communications* 12.1 (2021), p. 4118.
[172] D. Caballero, R. Voituriez, and D. Riveline. "Protrusion Fluctuations Direct Cell Motion". English. In: *Biophysical Journal* 107.1 (2014), pp. 34–42.
[173] P. DiMilla, J. Stone, J. Quinn, S. Albelda, and D. Lauffenburger. "Maximal migration of human smooth muscle cells on fibronectin and type IV collagen occurs at an intermediate attachment strength". In: *Journal of Cell Biology* 122.3 (1993), pp. 729–737.
[174] S. S. Chang, W.-h. Guo, Y. Kim, and Y.-l. Wang. "Guidance of Cell Migration by Substrate Dimension". en. In: *Biophysical Journal* 104.2 (2013), pp. 313–321.
[175] S. L. Gupton and C. M. Waterman-Storer. "Live-Cell Fluorescent Speckle Microscopy of Actin Cytoskeletal Dynamics and Their Perturbation by Drug Perfusion". In: *Cell Biology, Four-Volume Set* 3 (2006), pp. 137–151.
[176] E. L. Barnhart, K. C. Lee, K. Keren, A. Mogilner, and J. A. Theriot. "An adhesion-dependent switch between mechanisms that determine motile cell shape". In: *PLoS Biology* 9.5 (2011).
[177] B. Borm, R. P. Requardt, V. Herzog, and G. Kirfel. "Membrane ruffles in cell migration: indicators of inefficient lamellipodia adhesion and compartments of actin filament reorganization". In: *Experimental Cell Research* 302.1 (2005), pp. 83–95.
[178] M. Prass, K. Jacobson, A. Mogilner, and M. Radmacher. "Direct measurement of the lamellipodial protrusive force in a migrating cell". en. In: *Journal of Cell Biology* 174.6 (2006), pp. 767–772.
[179] F. Heinemann, H. Doschke, and M. Radmacher. "Keratocyte Lamellipodial Protrusion Is Characterized by a Concave Force-Velocity Relation". In: *Biophys J* 100.6 (2011), pp. 1420–1427.
[180] J. Zimmermann, C. Brunner, M. Enculescu, M. Goegler, A. Ehrlicher, J. Käs, and M. Falcke. "Actin Filament Elasticity and Retrograde Flow Shape the Force-Velocity Relation of Motile Cells". In: *Biophysical Journal* 102.2 (2012), pp. 287–295.

[181] W. D. Leineweber and S. I. Fraley. “Adhesion tunes speed and persistence by coordinating protrusions and extracellular matrix remodeling”. In: *Developmental Cell* 58.15 (2023), 1414–1428.e4.
[182] A. B. Verkhovsky, T. M. Svitkina, and G. G. Borisy. “Self-polarization and directional motility of cytoplasm”. In: *Current Biology* 9.1 (1999), pp. 11–20.
[183] J. E. Ron, P. Monzo, N. C. Gauthier, R. Voituriez, and N. S. Gov. “One-dimensional cell motility patterns”. en. In: *Physical Review Research* 2.3 (2020), p. 033237.
[184] P. Sens. “Stick–slip model for actin-driven cell protrusions, cell polarization, and crawling”. en. In: *Proceedings of the National Academy of Sciences* 117.40 (2020), pp. 24670–24678.
[185] G. L. Ryan, N. Watanabe, and D. Vavylonis. “A review of models of fluctuating protrusion and retraction patterns at the leading edge of motile cells”. en. In: *Cytoskeleton* 69.4 (2012), pp. 195–206.
[186] R. Link, K. Weißenbruch, M. Tanaka, M. Bastmeyer, and U. S. Schwarz. “Cell Shape and Forces in Elastic and Structured Environments: From Single Cells to Organoids”. en. In: *Advanced Functional Materials* n/a.n/a (2023), p. 2302145.
[187] P. Romanczuk, M. Bär, W. Ebeling, B. Lindner, and L. Schimansky-Geier. “Active Brownian particles”. en. In: *The European Physical Journal Special Topics* 202.1 (2012), pp. 1–162.
[188] D. Selmeczi, S. Mosler, P. H. Hagedorn, N. B. Larsen, and H. Flyvbjerg. “Cell motility as persistent random motion: Theories from experiments”. In: *Biophysical Journal* 89.2 (2005), pp. 912–931.
[189] B. G. Mitterwallner, C. Schreiber, J. O. Daldrop, J. O. Rädler, and R. R. Netz. “Non-Markovian data-driven modeling of single-cell motility”. In: *Physical Review E* 101.3 (2020).
[190] A. Mogilner and G. Oster. “Force Generation by Actin Polymerization II: The Elastic Ratchet and Tethered Filaments”. English. In: *Biophysical Journal* 84.3 (2003), pp. 1591–1605.
[191] C. E. Chan and D. J. Odde. “Traction Dynamics of Filopodia on Compliant Substrates”. In: *Science* 322.5908 (2008), pp. 1687–1691.
[192] F. Gerbal, P. Chaikin, Y. Rabin, and J. Prost. “An Elastic Analysis of Listeria monocytogenes Propulsion”. In: *Biophys J* 79.5 (2000), pp. 2259–2275.
[193] E. M. Craig, J. Stricker, M. Gardel, and A. Mogilner. “Model for adhesion clutch explains biphasic relationship between actin flow and traction at the cell leading edge”. en. In: *Physical Biology* 12.3 (2015), p. 035002.
[194] G. Upton and I. Cook. *A Dictionary of Statistics*. Oxford Paperback Reference. OUP Oxford, 2008.
[195] I. Fornacon-Wood, H. Mistry, C. Johnson-Hart, C. Faivre-Finn, J. P. B. O’Connor, and G. J. Price. “Understanding the Differences Between Bayesian and Frequentist Statistics”. English. In: *International Journal of Radiation Oncology, Biology, Physics* 112.5 (2022), pp. 1076–1082.
[196] A. Gelman and C. R. Shalizi. “Philosophy and the practice of Bayesian statistics”. en. In: *British Journal of Mathematical and Statistical Psychology* 66.1 (2013), pp. 8–38.
[197] G. Box and G. Tiao. *Bayesian Inference in Statistical Analysis*. Wiley Classics Library. Wiley, 2011.
[198] A. Stuart and K. Ord. *Kendall’s Advanced Theory of Statistics, Distribution Theory*. Wiley, 2010.
[199] K. Cranmer, J. Brehmer, and G. Louppe. “The frontier of simulation-based inference”. In: *Proceedings of the National Academy of Sciences* 117.48 (2020), pp. 30055–30062.
[200] T. A. Le, A. G. Baydin, R. Zinkov, and F. Wood. “Using synthetic data to train neural networks is model-based reasoning”. In: *2017 International Joint Conference on Neural Networks (IJCNN)*. 2017, pp. 3514–3521.
[201] J. Chan, V. Perrone, J. Spence, P. Jenkins, S. Mathieson, and Y. Song. “A Likelihood-Free Inference Framework for Population Genetic Data using Exchangeable Neural Networks”. In: *Advances in Neural Information Processing Systems*. Vol. 31. Curran Associates, Inc., 2018.
[202] G. Papamakarios and I. Murray. “Fast ϵ-free Inference of Simulation Models with Bayesian Conditional Density Estimation”. In: *Advances in Neural Information Processing Systems*. Vol. 29. Curran Associates, Inc., 2016.

[203] J.-M. Lueckmann, P. J. Goncalves, G. Bassetto, K. Öcal, M. Nonnenmacher, and J. H. Macke. "Flexible statistical inference for mechanistic models of neural dynamics". In: *Advances in Neural Information Processing Systems*. Vol. 30. Curran Associates, Inc., 2017.

[204] D. S. Greenberg, M. Nonnenmacher, and J. H. Macke. "Automatic Posterior Transformation for Likelihood-free Inference". en. In: *Proceedings of the 36 th International Conference on Machine Learning*. 2019.

[205] C. M. Bishop. "Mixture density networks". en-GB. In: Birmingham: Aston University, 1994.

[206] G. Papamakarios, T. Pavlakou, and I. Murray. "Masked Autoregressive Flow for Density Estimation". In: *Advances in Neural Information Processing Systems*. Ed. by I. Guyon, U. V. Luxburg, S. Bengio, H. Wallach, R. Fergus, S. Vishwanathan, and R. Garnett. Vol. 30. Curran Associates, Inc., 2017.

[207] G. Papamakarios, E. Nalisnick, D. J. Rezende, S. Mohamed, and B. Lakshminarayanan. "Normalizing Flows for Probabilistic Modeling and Inference". In: *Journal of Machine Learning Research* 22.57 (2021), pp. 1–64.

[208] C. Durkan, A. Bekasov, I. Murray, and G. Papamakarios. "Neural Spline Flows". In: *Advances in Neural Information Processing Systems*. Vol. 32. Curran Associates, Inc., 2019.

[209] P. J. Gonçalves, J.-M. Lueckmann, M. Deistler, M. Nonnenmacher, K. Öcal, G. Bassetto, C. Chintaluri, W. F. Podlaski, S. A. Haddad, T. P. Vogels, D. S. Greenberg, and J. H. Macke. "Training deep neural density estimators to identify mechanistic models of neural dynamics". In: *eLife* 9 (2020). Ed. by J. R. Huguenard, T. O'Leary, and M. S. Goldman, e56261.

[210] A. Tejero-Cantero, J. Boelts, M. Deistler, J.-M. Lueckmann, C. Durkan, P. J. Gonçalves, D. S. Greenberg, and J. H. Macke. *SBI – A toolkit for simulation-based inference*. 2020.

[211] J. Hermans, A. Delaunoy, F. Rozet, A. Wehenkel, V. Begy, and G. Louppe. *A Trust Crisis In Simulation-Based Inference? Your Posterior Approximations Can Be Unfaithful*. 2022.

[212] D. P. Kingma, T. Salimans, and M. Welling. "Variational Dropout and the Local Reparameterization Trick". In: *Advances in Neural Information Processing Systems*. Ed. by C. Cortes, N. Lawrence, D. Lee, M. Sugiyama, and R. Garnett. Vol. 28. Curran Associates, Inc., 2015.

[213] J. Oesterle, C. Behrens, C. Schröder, T. Hermann, T. Euler, K. Franke, R. G. Smith, G. Zeck, and P. Berens. "Bayesian inference for biophysical neuron models enables stimulus optimization for retinal neuroprosthetics". In: *eLife* 9 (2020). Ed. by A. Borst, J. R. Huguenard, A. Borst, and A. L. Fairhall, e54997.

[214] D. B. Brückner, A. Fink, J. O. Rädler, and C. P. Broedersz. "Disentangling the behavioural variability of confined cell migration". In: *Journal of The Royal Society Interface* 17.163 (2020), p. 20190689.

[215] R. M. Lee, H. Yue, W.-J. Rappel, and W. Losert. "Inferring single-cell behaviour from large-scale epithelial sheet migration patterns". In: *Journal of The Royal Society Interface* 14.130 (2017), p. 20170147.

[216] D. B. Brückner and C. P. Broedersz. "Learning dynamical models of single and collective cell migration: a review". en. In: *Reports on Progress in Physics* 87.5 (2024), p. 056601.

[217] J. Icha, M. Weber, J. C. Waters, and C. Norden. "Phototoxicity in live fluorescence microscopy, and how to avoid it". en. In: *BioEssays* 39.8 (2017), p. 1700003.

[218] M. Atienza Juanatey. "Automated High-Throughput 1D Single Cell Migration Assay". en. MA thesis. Munich: Ludwigs-Maximilian-Universität München, 2023.

[219] V. Studer. "PRINTING AN ADHESIVE PATTERN ON AN ANTI-FOULING SUPPORT". English. US-20170218230-A1. 2017.

[220] C. R. Burch and J. P. P. Stock. "Phase-Contrast Microscopy". en. In: *Journal of Scientific Instruments* 19.5 (1942), p. 71.

[221] K. Thorn. "A quick guide to light microscopy in cell biology". In: *Molecular Biology of the Cell* 27.2 (2016), pp. 219–222.

[222] D. J. Stephens and V. J. Allan. "Light Microscopy Techniques for Live Cell Imaging". In: *Science* 300.5616 (2003), pp. 82–86.

[223] D. J. Webb and C. M. Brown. “Epi-Fluorescence Microscopy”. en. In: *Cell Imaging Techniques: Methods and Protocols*. Ed. by D. J. Taatjes and J. Roth. Totowa, NJ: Humana Press, 2013, pp. 29–59.

[224] J. W. Lichtman and J.-A. Conchello. “Fluorescence microscopy”. en. In: *Nature Methods* 2.12 (2005), pp. 910–919.

[225] M. J. Sanderson, I. Smith, I. Parker, and M. D. Bootman. “Fluorescence Microscopy”. en. In: *Cold Spring Harbor Protocols* 2014.10 (2014), pdb.top071795.

[226] C. Stringer, T. Wang, M. Michaelos, and M. Pachitariu. “Cellpose: a generalist algorithm for cellular segmentation”. en. In: *Nature Methods* 18.1 (2021), pp. 100–106.

[227] M. Pachitariu and C. Stringer. “Cellpose 2.0: how to train your own model”. en. In: *Nature Methods* 19.12 (2022), pp. 1634–1641.

[228] A. N. Gonzalez-Beltran, P. Masuzzo, C. Ampe, G.-J. Bakker, S. Besson, R. H. Eibl, P. Friedl, M. Gunzer, M. Kittisopikul, S. E. L. Dévédec, S. Leo, J. Moore, Y. Paran, J. Prilusky, P. Rocca-Serra, P. Roudot, M. Schuster, G. Sergeant, S. Strömblad, J. R. Swedlow, M. van Erp, M. Van Troys, A. Zaritsky, S.-A. Sansone, and L. Martens. “Community standards for open cell migration data”. In: *GigaScience* 9.5 (2020), giaa041.

[229] M. D. Wilkinson, M. Dumontier, I. J. Aalbersberg, G. Appleton, M. Axton, A. Baak, N. Blomberg, J.-W. Boiten, L. B. da Silva Santos, P. E. Bourne, J. Bouwman, A. J. Brookes, T. Clark, M. Crosas, I. Dillo, O. Dumon, S. Edmunds, C. T. Evelo, R. Finkers, A. Gonzalez-Beltran, A. J. G. Gray, P. Groth, C. Goble, J. S. Grethe, J. Heringa, P. A. C. ’t Hoen, R. Hooft, T. Kuhn, R. Kok, J. Kok, S. J. Lusher, M. E. Martone, A. Mons, A. L. Packer, B. Persson, P. Rocca-Serra, M. Roos, R. van Schaik, S.-A. Sansone, E. Schultes, T. Sengstag, T. Slater, G. Strawn, M. A. Swertz, M. Thompson, J. van der Lei, E. van Mulligen, J. Velterop, A. Waagmeester, P. Wittenburg, K. Wolstencroft, J. Zhao, and B. Mons. “The FAIR Guiding Principles for scientific data management and stewardship”. en. In: *Scientific Data* 3.1 (2016), p. 160018.

[230] P. Masuzzo and L. Martens. “An open data ecosystem for cell migration research”. English. In: *Trends in Cell Biology* 25.2 (2015), pp. 55–58.

[231] P. Masuzzo, M. Van Troys, C. Ampe, and L. Martens. “Taking Aim at Moving Targets in Computational Cell Migration”. In: *Trends in Cell Biology* 26.2 (2016), pp. 88–110.

[232] P. Masuzzo, L. Huyck, A. Simiczyjew, C. Ampe, L. Martens, and M. Van Troys. “An end-to-end software solution for the analysis of high-throughput single-cell migration data”. en. In: *Scientific Reports* 7.1 (2017), p. 42383.

[233] A. Klimek, D. Mondal, S. Block, P. Sharma, and R. R. Netz. “Data-driven classification of individual cells by their non-Markovian motion”. English. In: *Biophysical Journal* 123.10 (2024), pp. 1173–1183.

[234] R. R. Netz. *Multi-point distribution for Gaussian non-equilibrium non-Markovian observables*. 2023.

[235] R. R. Netz. “Derivation of the nonequilibrium generalized Langevin equation from a time-dependent many-body Hamiltonian”. In: *Physical Review E* 110.1 (2024), p. 014123.

[236] P. Dieterich, R. Klages, R. Preuss, and A. Schwab. “Anomalous dynamics of cell migration”. In: *Proceedings of the National Academy of Sciences of the United States of America* 105.2 (2008), pp. 459–463.

[237] D. Selmeczi, L. Li, L. I. Pedersen, S. F. Nrrelykke, P. H. Hagedorn, S. Mosler, N. B. Larsen, E. C. Cox, and H. Flyvbjerg. “Cell motility as random motion: A review”. en. In: *The European Physical Journal Special Topics* 157.1 (2008), pp. 1–15.

[238] D. Campos, V. Méndez, and I. Llopis. “Persistent random motion: Uncovering cell migration dynamics”. In: *Journal of Theoretical Biology* 267.4 (2010), pp. 526–534.

[239] I. P. M. Tomlinson, M. R. Novelli, and W. F. Bodmer. “The mutation rate and cancer”. In: *Proceedings of the National Academy of Sciences* 93.25 (1996), pp. 14800–14803.

[240] A. L. Jackson and L. A. Loeb. “The Mutation Rate and Cancer”. In: *Genetics* 148.4 (1998), pp. 1483–1490.

[241] A. Sanchez, H. G. Garcia, D. Jones, R. Phillips, and J. Kondev. “Effect of Promoter Architecture on the Cell-to-Cell Variability in Gene Expression”. en. In: *PLOS Computational Biology* 7.3 (2011), e1001100.

[242] U. M. Litzenburger, J. D. Buenrostro, B. Wu, Y. Shen, N. C. Sheffield, A. Kathiria, W. J. Greenleaf, and H. Y. Chang. “Single-cell epigenomic variability reveals functional cancer heterogeneity”. en. In: *Genome Biology* 18.1 (2017), p. 15.

[243] K. Wosikowski, D. Schuurhuis, G. J. Kops, M. Saceda, and S. E. Bates. “Altered gene expression in drug-resistant human breast cancer cells”. eng. In: *Clinical Cancer Research: An Official Journal of the American Association for Cancer Research* 3.12 Pt 1 (1997), pp. 2405–2414.

[244] M. Strauch, A. Lüdke, D. Münch, T. Laudes, C. G. Galizia, E. Martinelli, L. Lavra, R. Paolesse, A. Ulivieri, A. Catini, R. Capuano, and C. Di Natale. “More than apples and oranges–detecting cancer with a fruit fly’s antenna”. eng. In: *Scientific Reports* 4 (2014), p. 3576.

[245] F. Buettner, K. N. Natarajan, F. P. Casale, V. Proserpio, A. Scialdone, F. J. Theis, S. A. Teichmann, J. C. Marioni, and O. Stegle. “Computational analysis of cell-to-cell heterogeneity in single-cell RNA-sequencing data reveals hidden subpopulations of cells”. en. In: *Nature Biotechnology* 33.2 (2015), pp. 155–160.

[246] A. Y. Alexandrova, K. Arnold, S. Schaub, J. M. Vasiliev, J.-J. Meister, A. D. Bershadsky, and A. B. Verkhovsky. “Comparative Dynamics of Retrograde Actin Flow and Focal Adhesions: Formation of Nascent Adhesions Triggers Transition from Fast to Slow Flow”. en. In: *PLoS ONE* 3.9 (2008). Ed. by C.-P. Heisenberg, e3234.

[247] J. Zimmermann, M. Enculescu, and M. Falcke. “Leading edge - gel coupling in lamellipodium motion”. In: *Phys Rev E* 82.5 (2010), p. 051925.

[248] M. J. Footer, J. W. J. Kerssemakers, J. A. Theriot, and M. Dogterom. “Direct measurement of force generation by actin filament polymerization using an optical trap”. In: *Proceedings of the National Academy of Sciences* 104.7 (2007), pp. 2181–2186.

[249] K. Wilson, A. Lewalle, M. Fritzsche, R. Thorogate, T. Duke, and G. Charras. “Mechanisms of leading edge protrusion in interstitial migration”. In: *Nature Communications* 4.1 (2013), p. 2896.

[250] M. Guo, A. F. Pegoraro, A. Mao, E. H. Zhou, P. R. Arany, Y. Han, D. T. Burnette, M. H. Jensen, K. E. Kasza, J. R. Moore, F. C. Mackintosh, J. J. Fredberg, D. J. Mooney, J. Lippincott-Schwartz, and D. A. Weitz. “Cell volume change through water efflux impacts cell stiffness and stem cell fate”. In: *Proceedings of the National Academy of Sciences* 114.41 (2017), E8618–E8627.

[251] T. Mitchison and M. Kirschner. “Cytoskeletal dynamics and nerve growth”. In: *Neuron* 1.9 (1988), pp. 761–772.

[252] C. Jurado, J. R. Haserick, and J. Lee. “Slipping or Gripping? Fluorescent Speckle Microscopy in Fish Keratocytes Reveals Two Different Mechanisms for Generating a Retrograde Flow of Actin”. In: *Molecular Biology of the Cell* 16.2 (2005), pp. 507–518.

[253] K. Hu, L. Ji, K. T. Applegate, G. Danuser, and C. M. Waterman-Storer. “Differential Transmission of Actin Motion Within Focal Adhesions”. In: *Science* 315.5808 (2007), pp. 111–115.

[254] M. L. Gardel, B. Sabass, L. Ji, G. Danuser, U. S. Schwarz, and C. M. Waterman. “Traction stress in focal adhesions correlates biphasically with actin retrograde flow speed”. In: *Journal of Cell Biology* 183.6 (2008), pp. 999–1005.

[255] Y. Li, P. Bhimalapuram, and A. R. Dinner. “Model for how retrograde actin flow regulates adhesion traction stresses”. en. In: *Journal of Physics: Condensed Matter* 22.19 (2010), p. 194113.

[256] P. Vallotton, G. Danuser, S. Bohnet, J.-J. Meister, and A. B. Verkhovsky. “Tracking Retrograde Flow in Keratocytes: News from the Front”. In: *Molecular Biology of the Cell* 16.3 (2005), pp. 1223–1231.

[257] J. Renkawitz, K. Schumann, M. Weber, T. Lämmermann, H. Pflicke, M. Piel, J. Polleux, J. P. Spatz, and M. Sixt. “Adaptive force transmission in amoeboid cell migration”. en. In: *Nature Cell Biology* 11.12 (2009), pp. 1438–1443.

[258] E. Evans. “Probing the Relation Between Force—Lifetime—and Chemistry in Single Molecular Bonds”. en. In: *Annual Review of Biophysics* 30.Volume 30, 2001 (2001), pp. 105–128.

[259] P. Bieling, T.-D. Li, J. Weichsel, R. McGorty, P. Jreij, B. Huang, D. A. Fletcher, and R. D. Mullins. “Force Feedback Controls Motor Activity and Mechanical Properties of Self-Assembling Branched Actin Networks”. English. In: *Cell* 164.1 (2016), pp. 115–127.

[260] B. Amiri. “Biophysical modeling of mesenchymal cell motility and its constitutive relations”. en. In: (2023).

[261] E. Barnhart, K.-C. Lee, G. M. Allen, J. A. Theriot, and A. Mogilner. “Balance between cell-substrate adhesion and myosin contraction determines the frequency of motility initiation in fish keratocytes”. In: *Proceedings of the National Academy of Sciences* 112.16 (2015), pp. 5045–5050.

[262] U. S. Bhalla. “Signaling in Small Subcellular Volumes. I. Stochastic and Diffusion Effects on Individual Pathways”. English. In: *Biophysical Journal* 87.2 (2004), pp. 733–744.

[263] W. Bialek and S. Setayeshgar. “Physical limits to biochemical signaling”. In: *Proceedings of the National Academy of Sciences* 102.29 (2005), pp. 10040–10045.

[264] P. Vallotton, S. L. Gupton, C. M. Waterman-Storert, and G. Danuser. “Simultaneous mapping of filamentous actin flow and turnover in migrating cells by quantitative fluorescent speckle microscopy”. In: *Proceedings of the National Academy of Sciences of the United States of America* 101.26 (2004), pp. 9660–9665.

[265] S. L. Gupton and C. M. Waterman-Storer. “Spatiotemporal Feedback between Actomyosin and Focal-Adhesion Systems Optimizes Rapid Cell Migration”. In: *Cell* 125.7 (2006), pp. 1361–1374.

[266] S. Yamashiro, H. Mizuno, M. B. Smith, G. L. Ryan, T. Kiuchi, D. Vavylonis, and N. Watanabe. “New single-molecule speckle microscopy reveals modification of the retrograde actin flow by focal adhesions at nanometer scales”. In: *Molecular Biology of the Cell* 25.7 (2014), pp. 1010–1024.

[267] T. Y. Tsai, S. R. Collins, C. K. Chan, A. Hadjitheodorou, P. Y. Lam, S. S. Lou, H. W. Yang, J. Jorgensen, F. Ellett, D. Irimia, M. W. Davidson, R. S. Fischer, A. Huttenlocher, T. Meyer, J. E. Ferrell, and J. A. Theriot. “Efficient Front-Rear Coupling in Neutrophil Chemotaxis by Dynamic Myosin II Localization”. In: *Developmental Cell* 49.2 (2019), 189–205.e6.

[268] O. M. Drozdowski, F. Ziebert, and U. S. Schwarz. “Optogenetic control of migration of contractile cells predicted by an active gel model”. en. In: *Communications Physics* 6.1 (2023), pp. 1–12.

[269] S. R. Bittner, A. Palmigiano, A. T. Piet, C. A. Duan, C. D. Brody, K. D. Miller, and J. Cunningham. “Interrogating theoretical models of neural computation with emergent property inference”. In: *eLife* 10 (2021). Ed. by J. R. Huguenard, T. O’Leary, and M. S. Goldman, e56265.

[270] N. Tolley, P. L. C. Rodrigues, A. Gramfort, and S. R. Jones. “Methods and considerations for estimating parameters in biophysically detailed neural models with simulation based inference”. en. In: *PLOS Computational Biology* 20.2 (2024), e1011108.

[271] C. M. Bishop. *Pattern Recognition and Machine Learning*. en. 1st ed. Springer New York, NY, 2006.

[272] T. Hastie, J. Friedman, and R. Tibshirani. *The Elements of Statistical Learning*. Springer Series in Statistics. New York, NY: Springer, 2001.

[273] S. Srinivasan, S. Das, V. Surve, A. Srivastava, S. Kumar, N. Jain, A. Sawant, C. Nayak, and R. Purwar. “Blockade of ROCK inhibits migration of human primary keratinocytes and malignant epithelial skin cells by regulating actomyosin contractility”. en. In: *Scientific Reports* 9.1 (2019), p. 19930.

[274] K. Champion, B. Lusch, J. N. Kutz, and S. L. Brunton. “Data-driven discovery of coordinates and governing equations”. In: *Proceedings of the National Academy of Sciences* 116.45 (2019), pp. 22445–22451.

[275] G. E. Hinton, A. Krizhevsky, and S. D. Wang. “Transforming Auto-Encoders”. en. In: *Artificial Neural Networks and Machine Learning – ICANN 2011*. Ed. by T. Honkela, W. Duch, M. Girolami, and S. Kaski. Vol. 6791. Berlin, Heidelberg: Springer Berlin Heidelberg, 2011, pp. 44–51.

[276] M. Kalia and S. L. Brunton. “Deep learning of normal form autoencoders for universal, parameter-dependent dynamics”. en. In: 2020.

[277] M. Raissi, P. Perdikaris, and G. E. Karniadakis. “Physics-informed neural networks: A deep learning framework for solving forward and inverse problems involving nonlinear partial differential equations”. In: *Journal of Computational Physics* 378 (2019), pp. 686–707.

[278] S. Cuomo, V. S. Di Cola, F. Giampaolo, G. Rozza, M. Raissi, and F. Piccialli. “Scientific Machine Learning Through Physics–Informed Neural Networks: Where we are and What’s Next”. en. In: *Journal of Scientific Computing* 92.3 (2022), p. 88.

[279] G. E. Karniadakis, I. G. Kevrekidis, L. Lu, P. Perdikaris, S. Wang, and L. Yang. “Physics-informed machine learning”. en. In: *Nature Reviews Physics* 3.6 (2021), pp. 422–440.

[280] H. Wang, T. Fu, Y. Du, W. Gao, K. Huang, Z. Liu, P. Chandak, S. Liu, P. Van Katwyk, A. Deac, A. Anandkumar, K. Bergen, C. P. Gomes, S. Ho, P. Kohli, J. Lasenby, J. Leskovec, T.-Y. Liu, A. Manrai, D. Marks, B. Ramsundar, L. Song, J. Sun, J. Tang, P. Veličković, M. Welling, L. Zhang, C. W. Coley, Y. Bengio, and M. Zitnik. “Scientific discovery in the age of artificial intelligence”. en. In: *Nature* 620.7972 (2023), pp. 47–60.

[281] N. Baker, F. Alexander, T. Bremer, A. Hagberg, Y. Kevrekidis, H. Najm, M. Parashar, A. Patra, J. Sethian, S. Wild, K. Willcox, and S. Lee. *Workshop Report on Basic Research Needs for Scientific Machine Learning: Core Technologies for Artificial Intelligence*. English. Tech. rep. USDOE Office of Science (SC), Washington, D.C. (United States), 2019.

[282] J. Renkawitz, A. Kopf, J. Stopp, I. de Vries, M. K. Driscoll, J. Merrin, R. Hauschild, E. S. Welf, G. Danuser, R. Fiolka, and M. Sixt. “Nuclear positioning facilitates amoeboid migration along the path of least resistance”. en. In: *Nature* 568.7753 (2019), pp. 546–550.

[283] S. Dolati, F. Kage, J. Mueller, M. Müsken, M. Kirchner, G. Dittmar, M. Sixt, K. Rottner, and M. Falcke. “On the relation between filament density, force generation, and protrusion rate in mesenchymal cell motility”. In: *Molecular Biology of the Cell* 29.22 (2018), pp. 2674–2686.

[284] C. F. Guimarães, L. Gasperini, A. P. Marques, and R. L. Reis. “The stiffness of living tissues and its implications for tissue engineering”. en. In: *Nature Reviews Materials* 5.5 (2020), pp. 351–370.

[285] D. E. Discher, P. Janmey, and Y.-l. Wang. “Tissue Cells Feel and Respond to the Stiffness of Their Substrate”. In: *Science* 310.5751 (2005), pp. 1139–1143.

[286] S. Stöberl. “Quantitative Cell Migration in 3D Compliant Hydrogel Microenvironments”. en. PhD thesis. Munich: Ludwig-Maximilians-Universität, 2024.

[287] S. W. Hell and J. Wichmann. “Breaking the diffraction resolution limit by stimulated emission: stimulated-emission-depletion fluorescence microscopy”. EN. In: *Optics Letters* 19.11 (1994), pp. 780–782.

[288] E. Betzig and J. K. Trautman. “Near-Field Optics: Microscopy, Spectroscopy, and Surface Modification Beyond the Diffraction Limit”. In: *Science* 257.5067 (1992), pp. 189–195.

[289] J. Schnitzbauer, M. T. Strauss, T. Schlichthaerle, F. Schueder, and R. Jungmann. “Super-resolution microscopy with DNA-PAINT”. en. In: *Nature Protocols* 12.6 (2017), pp. 1198–1228.

[290] R. Jungmann, M. S. Avendaño, J. B. Woehrstein, M. Dai, W. M. Shih, and P. Yin. “Multiplexed 3D cellular super-resolution imaging with DNA-PAINT and Exchange-PAINT”. en. In: *Nature Methods* 11.3 (2014), pp. 313–318.

[291] H. Deschout, T. Lukes, A. Sharipov, D. Szlag, L. Feletti, W. Vandenberg, P. Dedecker, J. Hofkens, M. Leutenegger, T. Lasser, and A. Radenovic. “Complementarity of PALM and SOFI for super-resolution live-cell imaging of focal adhesions”. en. In: *Nature Communications* 7.1 (2016), p. 13693.

[292] M. Pittman, E. Iu, K. Li, M. Wang, J. Chen, N. Taneja, M. H. Jo, S. Park, W.-H. Jung, L. Liang, I. Barman, T. Ha, S. Gaitanaros, J. Liu, D. Burnette, S. Plotnikov, and Y. Chen. “Membrane ruffling is a mechanosensor of extracellular fluid viscosity”. en. In: *Nature Physics* 18.9 (2022), pp. 1112–1121.

[293] G. A. Dunn and G. E. Jones. “Cell motility under the microscope: Vorsprung durch Technik”. en. In: *Nature Reviews Molecular Cell Biology* 5.8 (2004), pp. 667–672.

[294] T. A. Dunn, S. Chen, D. A. Faith, J. L. Hicks, E. A. Platz, Y. Chen, C. M. Ewing, J. Sauvageot, W. B. Isaacs, A. M. De Marzo, and J. Luo. “A Novel Role of Myosin VI in Human Prostate Cancer”. en. In: *The American Journal of Pathology* 169.5 (2006), pp. 1843–1854.

[295] H.-P. Wollscheid, M. Biancospino, F. He, E. Magistrati, E. Molteni, M. Lupia, P. Soffientini, K. Rottner, U. Cavallaro, U. Pozzoli, M. Mapelli, K. J. Walters, and S. Polo. “Diverse functions of myosin VI elucidated by an isoform-specific α-helix domain”. en. In: *Nature Structural & Molecular Biology* 23.4 (2016), pp. 300–308.

[296] H. Yoshida, W. Cheng, J. Hung, D. Montell, E. Geisbrecht, D. Rosen, J. Liu, and H. Naora. “Lessons from border cell migration in the *Drosophila* ovary: A role for myosin VI in dissemination of human ovarian cancer”. en. In: *Proceedings of the National Academy of Sciences* 101.21 (2004), pp. 8144–8149.

[297] D. B. Allan, T. Caswell, N. C. Keim, C. M. van der Wel, and R. W. Verweij. *soft-matter/trackpy: v0.6.4*. 2024.

[298] P. S. Foundation. *The Python Language Reference*. en. 2024.

[299] J. Bezanson, A. Edelman, S. Karpinski, and V. B. Shah. “Julia: A Fresh Approach to Numerical Computing”. In: *SIAM Review* 59.1 (2017), pp. 65–98.

[300] S. Talts, M. Betancourt, D. Simpson, A. Vehtari, and A. Gelman. *Validating Bayesian Inference Algorithms with Simulation-Based Calibration*. 2020.

Danksagung

Schlussendlich möchte ich hier meine Dankbarkeit gegenüber alldenjenigen äußern, die zur Entstehung dieser Doktorarbeit beigetragen haben.

Joachim Rädler gilt sicherlich der größte Dank. Ohne Dein Vertrauen in mich und die stete Bereitschaft, mich zu fördern und zu unterstützen, wäre diese Arbeit nie entstanden. Danke, für die Möglichkeit, an Deinem Lehrstuhl und unter Deiner Betreuung promovieren zu dürfen.
Christoph Schreiber als meinem direkten Vorgänger und Mentor gebührt der Dank dafür, von seiner Expertise immens profitiert zu haben. Die Betreuung meiner Masterarbeit und die Förderung meines Promotionsvorhabens waren für die Doktorarbeit Grundstein legend.
Miguel Atienza Junatey bin ich dankbar für die wertvolle Teamarbeit, die sich schnell aus einem engen Betreuungsverhältnis entwickelte. Dazu gehörten nicht nur angeregte wissenschaftliche Diskussionen, sondern auch das kompetitive Cappuccino machen.
Martin Falcke und Behnam Amiri, sowie im späteren Verlauf auch Anton Klimek, haben durch ihre Expertise der theoretischen Physik maßgeblich zum Erfolg dieser Arbeit und meinem Verständnis der Biophysik beigetragen.
Ohne Gerlinde Schwake und Charlott Leu wäre jegliche Laborarbeit undenkbar. Eure Unterstützung, die sich keinesfalls nur auf technische Fragen beschränkte, machte diese Arbeit erst möglich.
Emily Brieger und Stefan Ströbli waren die besten Kollegen, Leidensgenossen und Konferenzbuddies, die man sich nur vorstellen konnte. Unsere legendäre Zeit in Israel wird unvergessen bleiben.
Nathalie Schäffler, Judith Müller und Agathe JOUNEAU, Simon Kempe und dem gesamten Lehrstuhl Rädler gebührt ein großer Dank für die intensive gemeinsame Zeit, die weit mehr als nur die Arbeit umfasste.
Chris bin ich nicht nur für unsere langjährige Freundschaft, sondern auch konkret für die anregenden Diskussionen dankbar, die den Bezug zur Klinik herstellten, sowie für das Korrekturlesen. Gleiches gilt auch für Christian, der mich mit seiner Nachhilfe zum Thema Machine Learning, sowie durch den sportlichen Ausgleich supportet hat.

Zu guter Letzt gilt natürlich ein besonderer Dank Luisa und meiner Familie. Danke!